FERMILAB-THESIS-2016-42

Abstract

First Detection of Low Energy Electron Neutrinos in Liquid Argon Time Projection Chambers

Corey Adams

2017

Electron neutrino appearance is the signature channel to address the most pressing questions in neutrino oscillations physics, at both long and short baselines. This includes the search for CP violation in the neutrino sector, which the U.S. flagship neutrino experiment DUNE will address. In addition, the Short Baseline Neutrino Program at Fermilab (MicroBooNE, SBND, ICARUS-T600) searches for new physics, such as sterile neutrinos, through electron neutrino appearance. Liquid argon time projection chambers are the forefront of neutrino detection technology, and the detector of choice for both short and long baseline neutrino oscillation experiments.

This work presents the first experimental observation and study of electron neutrinos in the 1-10 GeV range, the essential oscillation energy regime for the above experiments. The systematic uncertainties for an electron neutrino appearance search for the Fermilab Short Baseline Neutrino Program are carefully quantified, and the characterization of separation between electrons and high energy photons is examined.

FERMILAB-THESIS-2016-42

First Detection of Low Energy Electron Neutrinos in Liquid Argon Time Projection Chambers

A Dissertation
Presented to the Faculty of the Graduate School
of
Yale University
in Candidacy for the Degree of
Doctor of Philosophy

by
Corey Adams

Dissertation Director: Professor Bonnie Fleming

May, 2017

For Shannon,

and my parents

Contents

List of Figures

List of Tables

Acknowledgements

I've encountered a lot of people over the past few years that have helped me, either directly or indirectly, and I want to thank you all. I hope I don't forget anyone...but if I do, know that it's not on purpose.

Thanks, most of all, to my wife Shannon. You were here when I started this, and you're still here at the end of it. That's dedication! I see every day the things you do to support me.

I also wouldn't have succeeded in finishing this marathon without the help and support of my family, especially my parents. You've been there to help and advise me since day one, and are still there helping. I couldn't have asked for more.

By the time thesis writing comes around, the first and second year of graduate school pain seems like a distant memory. But that was shared suffering (Jackson E&M comes to mind...) and I'm grateful for your help, friendship, and fun that we had, Dave, Anya, Evan, Anthony, Alexey, Hannah, Ryan. It would have been impossible to stay sane and survive that without you.

I've had the pleasure of working with and knowing a lot of people over the years, and one way or another you've been really helpful as I worked towards this thesis. Thanks to Kyungeun, Sue and Lil, David K. and David C., Kazu, Mike M., Joseph, Kirby, Tingjun, Zarko, Georgia, Dave S., ... and everyone else that I've missed.

Josh and Mitch, your advice, feedback, and conversations really steered me in the right direction over the past year and turned this into an analysis I'm proud of. Thanks.

Ariana, Elena, Brooke, Xiao, and Serhan, you've made this group a lot of fun over the past years, and I am really going to miss it. You've been great colleagues and even better friends.

A big part of learning to do research and becoming a scientist is working with those who've come before you and learning everything they can teach you. Andrzej, Roxanne, Jonathan, and Eric, I'm really grateful for everything you've taught me. Andrzej, you've given me the best career advice I think I've ever gotten with "Go learn physics." Challenging to do, but you've steered me well.

Flavio and Ornella, you've taught me more about neutrino physics and performing research than I can recount. I look forward to many more years of you teaching me, and I hope you realize just how big an impact you've had on me and everyone around you. Over the last year, Ornella, no one has guided me more in completing my work than you.

When I was looking for a research group during my first year of graduate school, a recently graduated student told me that working with Bonnie was "the best decision I made during graduate school." Now, at the end, I can echo that statement. Bonnie, you've treated me as a colleague from day one, always giving me respect and kindness while teaching me how to do physics. You've taught me how to be a better physicist, and how to succeed in science, and you set the example of how to treat everyone around you so well.

I know I thanked you first, Shannon, but it's worth doing again. Thanks for helping me through every single day of graduate school. I should amend my earlier statement: marrying you was the best decision I made in graduate school, or ever. Thanks for everything.

Summary

This thesis presents a detailed characterization of electron neutrinos in a state of the art neutrino detector, the liquid argon time projection chamber. The signature of electron neutrinos in LArTPCs is critical to the US accelerator based neutrino physics program, at both short and long baselines. Chapters 1, 2, and 3 present an overview of current neutrino physics, including how the field of neutrino physics reached its current state, as well as a description of both the neutrino beams and detector technologies needed to advance the field further. Chapter 4 presents the current short baseline anomalies that hint towards non standard neutrino oscillations and the experimental outlook of the Fermilab Short Baseline Neutrino Program, while Chapter 5 highlights the importance of carefully studying and accounting for the uncertainties in Fermilab's program. Finally, 6 presents the first experimental observation of electron neutrinos in the 1 to 10 GeV range in a liquid argon time projection chamber, laying the groundwork for a decade's worth of precision neutrino measurements.

Chapter 1

Neutrino Physics

Since its original inception in the 1930s, neutrino physics has developed into a robust subfield of high energy physics. The neutrino was theorized in the 1930s by Wolfgang Pauli, rigorously incorporated into the theory of beta decay by Enrico Fermi [1], and first detected in 1956 by Clyde Cowan and Frederick Reines [2].

Originally, the neutrino was postulated to preserve conservation of momentum in the theory of beta decay, where a nucleon such as a neutron is converted to a proton by emitting an electron and a neutrino:

$$n \rightarrow p^+ + e^- + \bar{\nu}_e \tag{1.1}$$

The reaction above is actually an example of a weak interaction happening at the quark level, where one of the neutron's down quarks converts to an up quark through the emission of a W^-. Unfortunately, the neutrino is a very weakly interacting particle, so the direct observation of both the electron and the neutrino from a β decay reaction was, and still is, impossible.

For the detection of the neutrino, Cowan and Reines used a very similar reaction to beta decay, but instead of producing a neutrino this reaction absorbs a neutrino and emits a neutron and a positron:

$$p^+ + \bar{\nu}_e \rightarrow e^- + n \tag{1.2}$$

Unlike neutrinos, neutrons and positrons are relatively easy to observe, so Cowan and Reines simply exposed a large sample of protons to a very large blast of neutrinos. Practically, this meant building a detector near a high intensity source of neutrinos, which they did: they exposed large tanks of water to the neutrino flux of a nuclear reactor at the Savannah River plant, in Georgia. The neutrinos coming to their detector (actually, *anti*-neutrinos) interacted with the protons and produced a neutron and a positron. The positron was observed after it interacted by annihilating with an electron in the water tank, producing a pair of gamma particles. The neutron was detected by it's capture on Cadmium, which was doped in the tank. The neutron capture also produces a gamma, but it is delayed from the positron's gamma pair. Cowan and Reines ultimately observed about three neutrinos per hour in their detector. Conclusively, when the reactor was shut off, they no longer observed neutrinos.

Since the first discovery of the neutrino, neutrinos and their interactions have played a central role in the development of the standard model of particle physics. Pauli originally proposed only one neutrino, but not long after his prediction (and before the experimental evidence that confirmed it) other types of neutrinos were postulated. Since then, 2 other types of neutrinos have been discovered, namely the muon and tau neutrinos [3], [4].

Conventionally, neutrinos are symbolized as ν_e, ν_μ, and ν_τ corresponding to the 3 flavors of charged leptons. The charged current interactions of these neutrinos, by exchanging a $W^\pm$ boson, produces an outgoing charged lepton of the same flavor as the incoming neutrino: ν_e produces electrons, $\bar{\nu}_e$ produces anti-electrons, ν_μ produces muons, etc, such as in Equations 1.1 and 1.2. However, neutrinos can also interact via neutral currents, where the outgoing lepton is *not* charged. Instead, the neutrino exchanges a neutral Z^0 boson with the target material. The first observed neutral current interaction is shown in Figure 1.1 [5].

Neutrino physics was dramatically altered with the discovery of neutrino oscillations, described below, which opens the door to many new questions, including measurements of CP Violation and possible sterile states of neutrinos. Since the 1960s until the early 2000s,

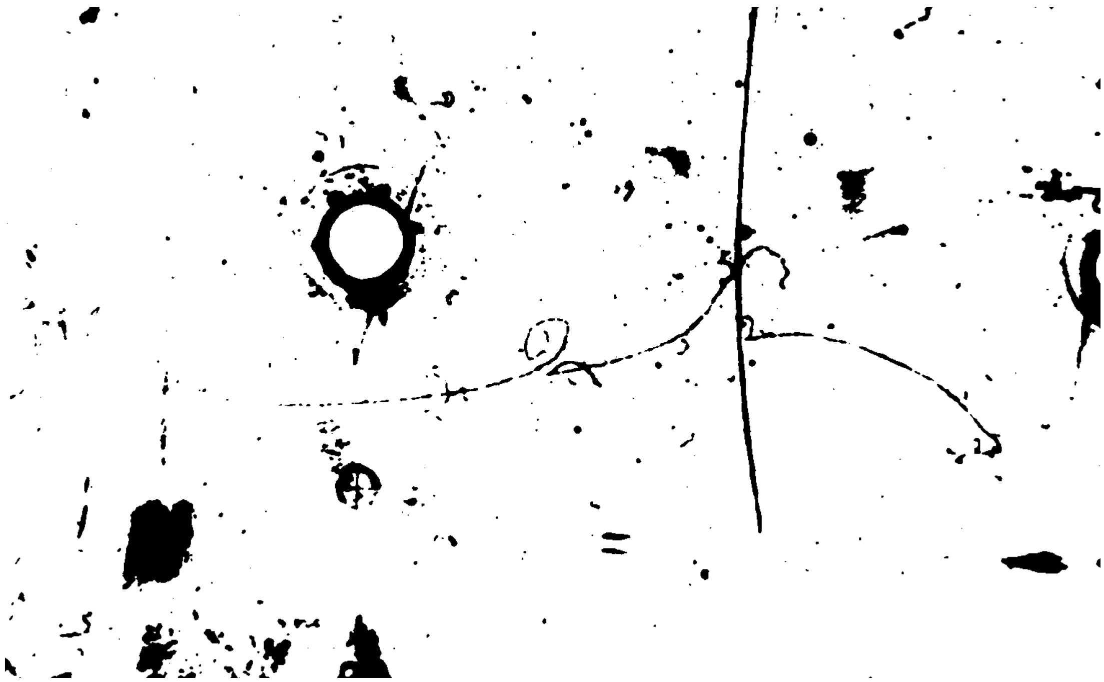

Figure 1.1: The first observed neutral current neutrino interaction, seen by Gargamelle in 1973.

the field of neutrino physics had an unresolved anomaly known as the Solar Neutrino Problem. Models of the interactions in the interior of the sun made a definite prediction for the number of electron-flavor neutrinos arriving at Earth [6], based on well grounded theories of stellar fuel burning. On the other hand, experiments sensitive to neutrinos observed a significant deficit as compared to predictions [7].

In 1998, the Super-Kamiokande experiment published definitive evidence of neutrino oscillations from their observation of atmospheric neutrinos [8] - one of the definitve. This evidence was also supported with observations from the Sudbury Neutrino Observatory (SNO) [9], and GALLEX/SAGE [10, 11]. With the confirmation of neutrino oscillations, a solution to the Solar Neutrino Anomaly had been found: the sun did in fact produce the predicted rate of electron neutrinos, but experiments that were only sensitive to electron neutrinos were unable to detect the muon and tau neutrinos that were produced through the oscillation mechanism.

The conclusive evidence for neutrino oscillations also implies that neutrinos are not, as

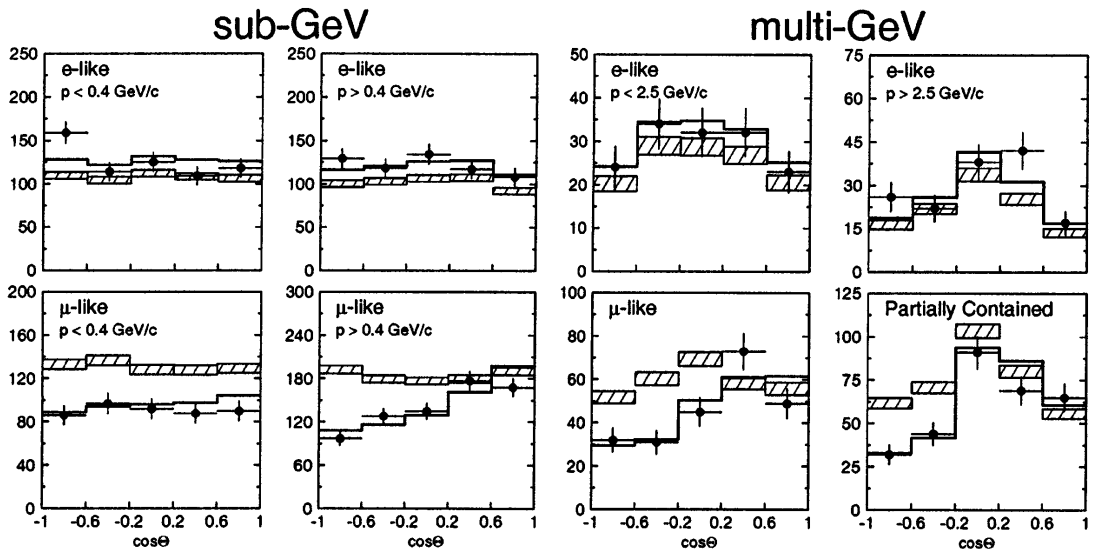

Figure 1.2: The distribution of zenith angle events from Super-Kamiokande, published in [8]. The deficit of upward going muon type neutrinos above 1 GeV is the definitive evidence for neutrino oscillations.

was initially believed, massless particles. However, neutrinos are known to be incredibly light weight, and cosmological constraints imply neutrinos have a summed mass (all three active flavors) of less than 0.23 eV [12, 13]. The exact mass of each type of neutrino is unknown still, though experiments are setting lower and lower bounds to directly constrain it [14, 15].

One of the exciting questions that can be probed by studying neutrinos is CP violation. Some theories predict that the current matter/anti-matter imbalance in the observable universe could be explained by CP violation by leptons, such as neutrinos [16]. This parameter is directly probable with neutrinos by measuring the difference in neutrino oscillations between neutrinos and anti-neutrinos. In particular, the neutrino matter effect [17, 18] leads to a large observable effect of CP violation in electron neutrinos.

Another intriguing avenue of discovery in neutrino physics is the resolution of short baseline anomalies, which may hint towards the existence of sterile neutrinos. Experiments have been proposed to probe these anomalies [19, 20], and other existing experiments have found ways to investigate short baseline anomalies already [21–24].

Both for the case of CP violation and the resolution of short baseline anomalies, the detection and measurement of electron neutrinos is critical. The most promising experiment to measure neutrino CP violation, DUNE [25], will look for the appearance of electron neutrinos in a primarily muon neutrino beam. The Fermilab Short Baseline Neutrino Program (SBN Program) [19] will similarly be searching for electron neutrinos in a primarily muon neutrino neutrino beam. The first stage of the SBN Program, MicroBooNE, is already running in Fermilab's Booster Neutrino Beam searching for low energy electron neutrinos.

Both DUNE and the SBN Program rely on high granularity detectors for their neutrino searches, the liquid argon time projection chamber (LArTPC, see Chapter 3). However, at the time of the publication of this thesis, only one LAr-TPC in the world had ever observed electron neutrinos. The ICARUS experiment includes an observation of two electron neutrinos at approximately 20 GeV [26]. On the other hand, the energy of interest to both DUNE and SBN is significantly lower, in the range of 1 GeV. Therefore, the work presented in this thesis is the first observation of low energy electron neutrinos in a liquid argon time projection chamber.

As will be shown in Chapter 4, the reduction and constraint of backgrounds related to the electron neutrino appearance searches is critical to their success. In past experiments, based largely on Cherenkov detectors, the observation of electron neutrinos at low energies is hindered by the presence of neutral current backgrounds from high energy photons. The suppression of these backgrounds is vital to the success of DUNE, MicroBooNE and other LAr-TPC experiments. Chapter 6 presents the first data driven measurements of separation power in LAr-TPCs to reject high energy photons from electrons, and as such is an essential measurement for the LAr-TPC neutrino program.

1.1 Neutrino Sources

Neutrinos, despite their weak interaction cross section and difficulty to observe, are actually incredibly common on Earth - more than a trillion neutrinos pass through an average sized human hand every second. By far the most powerful nearby source of neutrinos is from the Sun, produced predominantly in proton-proton fusion. But, more powerful (and more exotic) sources of neutrinos are known to exist, such as supernova [27, 28]. Terrestrially, neutrinos are produced in the geothermal reactions of the Earth's core, and there is large flux of "atmospheric" neutrinos produced by the interactions of cosmic particles in the upper atmosphere. As radioactive elements decay through weak interactions, radioactive material emits neutrinos as well - in fact this can be a quite useful source for calibration of neutrino experiments.

There are also artificial sources of neutrinos, most commonly nuclear reactors. Though they are less powerful than the Sun, neutrino experiments can get significantly closer to a nuclear reactor than to the Sun, and the local neutrino flux can be quite high. The most sophisticated artificial source of neutrinos comes from the neutrinos beams produced at accelerator complexes such as Fermilab, CERN, and J-PARC. Artificial neutrino beams can provide a high intensity source of neutrinos over a large range of energies, and offer many other benefits as well.

A detailed understanding of the source of neutrinos is vital to the success of every neutrino experiment, and Chapter 2 explores neutrino beams in more detail.

1.2 Neutrino Oscillations

Neutrino oscillations [29–31] are the foundation and the starting point for modern neutrino experiments exploring CP violation and short baseline anomalies, and can be used to probe the mass hierarchy of the neutrinos. As such, they are fundamentally important to neutrino experiments, so a description of the theory of neutrino oscillations and the experimental evidence is presented here.

1.2.1 Neutrino Oscillations - Theory

Neutrinos, when produced through electro-weak interactions, are produced in flavor eigenstates. To date, there are known to be three flavors of neutrinos: ν_e, ν_μ, and ν_τ. Each of these neutrinos, as suggested by their name, corresponds to a charged lepton. The conservation of lepton flavor, in electro-weak interactions, dictates that the number of leptons of a particular flavor is conserved during an interaction. As an example, the decay of a muon to an electron would violate lepton flavor conservation if not for the presence of neutrinos:

$$\mu^- \rightarrow e^- + \bar{\nu}_e + \nu_\mu \tag{1.3}$$

Lepton flavor violation is not, however, a law of nature. The most striking evidence for the violation of lepton flavor conservation is neutrino oscillations, though there are hints and proposals that lepton flavor could be violated by charged leptons as well [32]. For neutrino oscillations, the violation of lepton flavor is a direct result of the fact that neutrinos in the lepton eigenstates are a superposition of the mass eigenstates of neutrinos:

$$\nu_e = \alpha\nu_1 + \beta\nu_2 + \gamma\nu_3 \tag{1.4}$$

where the numerical neutrino states represent the neutrinos with a well defined mass. It should be noted, from a historical perspective, that in fact neutrinos were originally considered to be zero-mass in the Standard Model. The discovery of neutrino oscillations instead provided definitive evidence that neutrinos **do** have mass. From a modern perspective, however, the evidence for neutrino masses is overwhelming. The interesting phenomenon, then, arise from the fact that neutrinos produce in lepton flavor states do not stay stably in those states.

The most common way to mathematically describe neutrino oscillations is through the

Pontecorvo-Maki-Nakagawa-Sakata matrix [29, 30], or PMNS matrix:

$$\begin{pmatrix} \nu_e \\ \nu_\mu \\ \nu_\tau \end{pmatrix} = \begin{pmatrix} U_{e1} & U_{e2} & U_{e3} \\ U_{\mu1} & U_{\mu2} & U_{\mu3} \\ U_{\tau1} & U_{\tau2} & U_{\tau3} \end{pmatrix} \begin{pmatrix} \nu_1 \\ \nu_2 \\ \nu_3 \end{pmatrix} \tag{1.5}$$

In this matrix, under the standard assumptions of neutrino oscillations, the rows and columns are normalize such that the matrix is unitary: $\sum_{i=1}^{3} |U_{\alpha i}|^2 = 1$, and similarly for the columns. It's very common for the PMNS matrix to be parameterize in terms of mixing angles:

$$\begin{pmatrix} U_{e1} & U_{e2} & U_{e3} \\ U_{\mu1} & U_{\mu2} & U_{\mu3} \\ U_{\tau1} & U_{\tau2} & U_{\tau3} \end{pmatrix} = \begin{pmatrix} 1 & 0 & 0 \\ 0 & \cos\theta_{23} & \sin\theta_{23} \\ 0 & -\sin\theta_{23} & \cos\theta_{23} \end{pmatrix} \times \tag{1.6}$$

$$\begin{pmatrix} \cos\theta_{13} & 0 & \sin\theta_{13} e^{-i\delta_{CP}} \\ 0 & 1 & 0 \\ -\sin\theta_{13} e^{i\delta_{CP}} & 0 & \cos\theta_{13} \end{pmatrix} \times \tag{1.7}$$

$$\begin{pmatrix} \cos\theta_{12} & \sin\theta_{23} & 0 \\ -\sin\theta_{23} & \cos\theta_{12} & 0 \\ 0 & 0 & 1 \end{pmatrix} \tag{1.8}$$

The value of this expansion is that the individual mixing angles are observable with different experimental setups. The additional phase, δ_{CP}, is needed if neutrinos violate Charge-Parity symmetry. Some theories suggest that neutrino violation of CP symmetry is responsible for the matter/anti-matter asymmetry in the Universe (see Section 1.3).

In general, an experiment probing neutrino oscillations will start with an ensemble of neutrinos prepared in a particular flavor state ν_α:

$$\nu_\alpha = U_{\alpha 1}\nu_1 + U_{\alpha 2}\nu_2 + U_{\alpha 3}\nu_3$$

The state of the neutrino ν_α evolves according to the standard time evolution operator, and so at a later time the neutrino state is

$$\nu_\alpha(t) = U_{\alpha 1}\nu_1(t) + U_{\alpha 2}\nu_2(t) + U_{\alpha 3}\nu_3(t)$$

where $\nu_j(t) = e^{-i(E_j t - \vec{p}\dot{x})}\nu_j(t)$, using the plane wave solution for the neutrinos. Since each neutrino has a different mass, the three components of a neutrino flavor state become out of phase as time passes. Since the neutrino masses are known to be very small, and the neutrinos detected in experiments are typically energies of MeV or higher, all observed neutrinos are ultra-relativistic. So, the energy expression in the time evolution of the neutrino flavor state can be simplified with $E_j \approx E + \frac{m_j^2}{2E}$. Therefore, the probability that a neutrino that started in state α will be observed in state β at a later time t is:

$$P_{\alpha\to\beta} = \left|\langle \nu_\alpha(t)|\nu_\beta\rangle\right|^2 = \left|\sum_i U_{i\alpha}U_{i\beta}e^{-it\frac{m_j^2}{2E}}\right|^2$$

Of course, since neutrinos are ultra-relativistic it is not possible to observe them at a later time in the same location. Instead, neutrino oscillations searches observe the neutrinos at a distance away from the source. Assuming the neutrinos travel at the speed of light, so that $L = ct$ (and typically setting c = 1), the useful oscillation probability expression for neutrino experiments is

$$P_{\alpha\to\beta} = \left|\sum_i U_{i\alpha}U_{i\beta}e^{-im_j^2\frac{L}{2E}}\right|^2$$

For the case of oscillation between two types of neutrinos, the oscillation probability is often expressed as

$$P_{\alpha\to\beta} = \sin^2(2\theta)\sin^2\left(\frac{\Delta m^2 L}{4E}\right) \tag{1.9}$$

As seen in the next section, the sinusoidal characteristic of oscillations is apparent when the neutrinos are presented as a function of L/E.

1.2.2 Neutrino Oscillations - Experimental Evidence

Neutrino oscillations have a compelling record of experimental evidence in their favor. This section provides a brief overview of some of the notable oscillation experiments to date. A much more complete summary of neutrino oscillations, both theory and experimental evidence, is available from the Particle Data Group [33].

Solar Neutrino Problem

The first experimental hint of neutrino oscillations came, retrospectively, with the "Solar Neutrino Problem." The standard Solar model makes a definite prediction for the number of neutrinos produced by the sun [6], while the observation of Ray Davis and John Bahcall at the Homestake experiment observed only approximately one third of the neutrinos they expected from the Sun. This observation was subsequently reproduced and confirmed by a number of experiments [9, 34–40].

The many neutrino detectors observing the solar neutrinos produced different measurements of their observed flux, compared to predictions from standard solar models - see Figure 1.3. Each experiment, however, observes a different deficit of neutrinos. However, the experiments searching for solar neutrinos had different minimum thresholds for detection, and the solar neutrino flux is not constant with energy (Figure 1.4). This strongly implied that the resolution of the Solar Neutrino Problem needed to account for a dependence on neutrino energy, consistent with neutrino oscillations. Further, the evidence was very strong that the neutrino oscillations in the Sun were affected by the interactions of neutrinos with matter, know as the Mikheev-Smirnov-Wolfenstien (MSW) effect [17, 18].

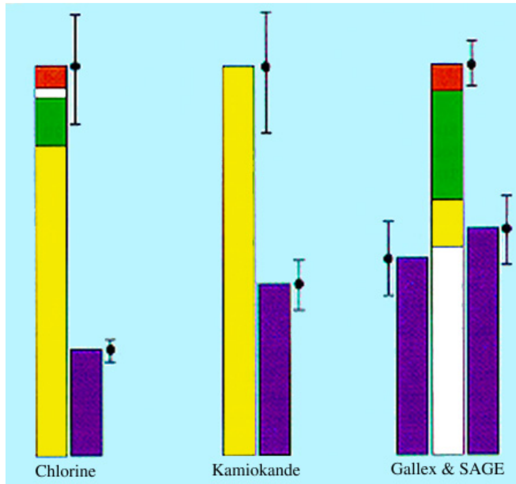

Figure 1.3: Solar neutrino deficit for the different detectors/materials. Figure from [41].

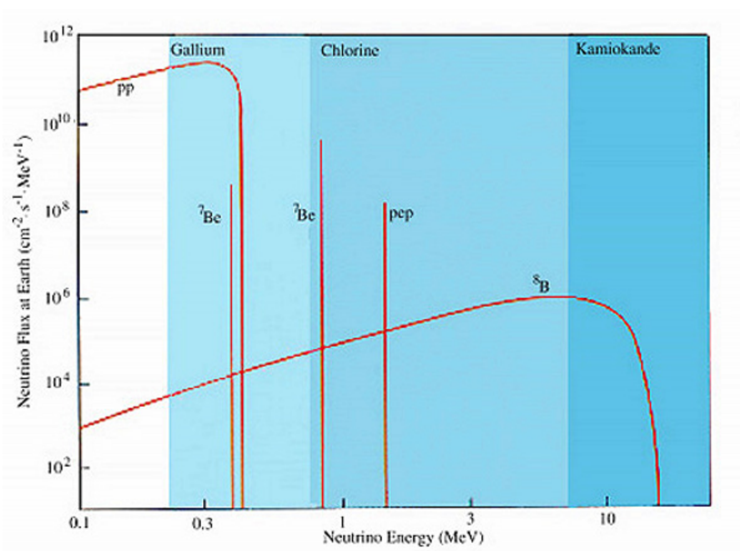

Figure 1.4: Solar neutrino flux, and the relevant region for the different detectors/materials. Figure from [41].

Eventually, with the results of experiments such as Super Kamiokande and and SNO, the squared mass separation required to explain the solar neutrino deficit in terms of oscillations was measured as $m_{solar} = 7.5 \times 10^{-5} eV^2$. This measurement was later confirmed by the KamLAND experiment [42, 43], who also were able to demonstrate experimentally the sinusoidal dependence of neutrino oscillations, in Figure 1.5. Combined with solar neutrino data, the KamLAND results [44, 45] indicated that the solar neutrino mass splitting, now understood to be Δm^2_{12}, is $\Delta m^2 12 = 7.5^{+0.19}_{-0.20} \times 10^{-5} eV^2$, and the oscillation mixing angle is given as $\tan^2(\theta_{12}) = 0.452^{+0.035}_{-0.033}$.

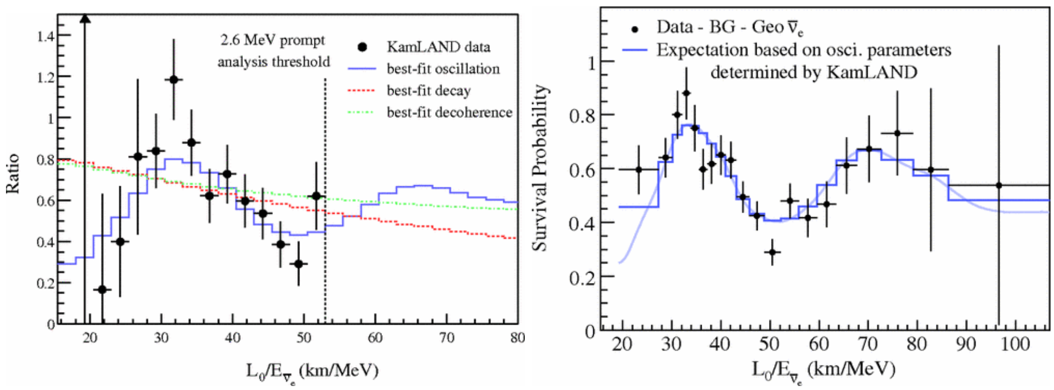

Figure 1.5: (Left) Initial oscillation spectrum from KamLAND. (Right) Higher statistics results from KamLAND. The data are plotted with L=180km, and the data agree well with the best fit oscillation hypothesis. Figures from [43, 44].

.

The resolution of the solar neutrino anomaly set off a cascade of neutrino oscillation searches, including the search for oscillations outside of the solar neutrino regime. The observation of atmospheric oscillations, in fact, was historically the first direct evidence of neutrino oscillations.

Atmospheric Neutrinos

Earth is continuously bombarded with particles in the upper atmosphere, producing (among other things) a flux of neutrinos primarily from the decay of pions and kaons [46–48]. The atmospheric flux is often predicted as a function of zenith angle, and this allows neutrino oscillation experiments to study neutrinos over a very large range of distances: the shortest distances of travel from production are 10s of kilometers, directly above a detector, to 1.2×10^4 kilometers, from the opposite side of the Earth. The atmospheric neutrino flux is composed of primarily of ν_μ, $\bar{\nu}_\mu$, ν_e, and $\bar{\nu}_e$ neutrinos in approximately a 2:1 ratio for (ν_μ + $\bar{\nu}_\mu$) : (ν_e + $\bar{\nu}_e$) [33].

Compelling evidence for the oscillation of atmospheric muon neutrinos was presented by the Super-Kamiokande collaboration in 1998 [8], shown in Figure 1.6. Because the Super-Kamiokande detector is unable to distinguish muons from anti-muons, there is no ability to sign select and the oscillation result is presented as a combined oscillation of muon neutrinos and anti-neutrinos. Because of the distances involved and the energy range of the neutrinos, the solar neutrino mixing is not plausible as an explanation for the oscillation of atmospheric neutrinos. In addition, the electron neutrino component of the flux is in general agreement with the observed data, assuming no oscillations. Therefore, the explanation is that atmospheric muon neutrinos oscillate predominantly into tau neutrinos. A subsequent study confirmed the statistical observation of tau neutrinos from atmospheric oscillations, though the tau neutrinos can not be identified on an event-by-event basis [49]. The atmospheric neutrino oscillation suggests a mass splitting that is in the range of $10^{-3} eV^2$, significantly higher than the observed solar neutrino mass splitting.

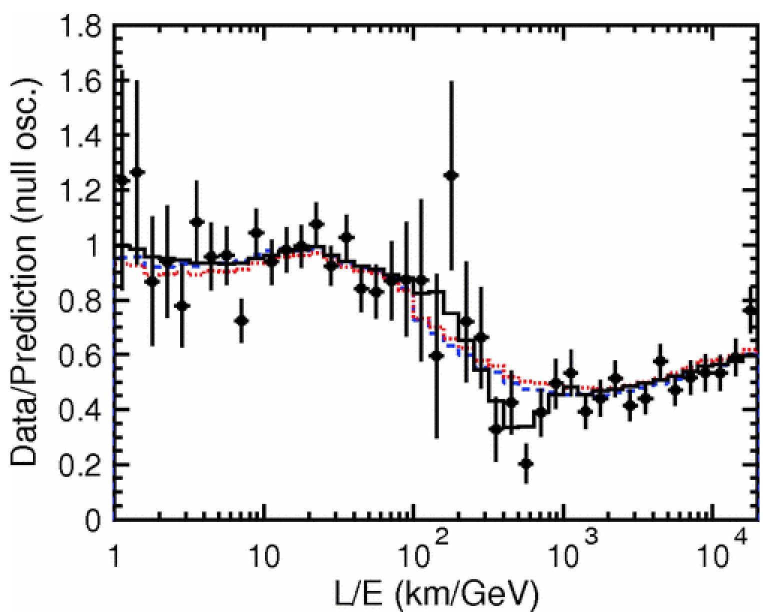

Figure 1.6: Super-Kamiokande atmospheric neutrino oscillations, as a function of L/E. L is calculated from the zenith angle of the detected neutrino. Figure from [50].

On-axis Neutrino Beams: K2K and MINOS

The precision measurement of the atmospheric neutrino mixing and mass splitting was determined using long baseline neutrino oscillation experiments with neutrino beams. The first such experiment, K2K (KEK to Kamiokande), observed oscillations through the disappearance of accelerator produced muon neutrinos [51]. MINOS was the second long baseline neutrino oscillation experiment, with a beam of neutrinos from Fermilab traveling to Soudan in Minnesota. MINOS reported oscillation [52] of muon neutrinos as well as muon anti-neutrinos due to the ability of the NuMI beam to run in an anti-neutrino enhanced configuration. MINOS is a magnetized detector, allowing sign selection of the muons it observes.

The advantage of MINOS and K2K over the results of Super-Kamiokande is that the source of neutrinos is controlled, the energy spectrum is relatively narrow banded ($< E_\nu >= 1.3 GeV$ for K2K), and the length for oscillations is fixed (250 km for K2K, 735 km for MINOS). Because the parameters of the experiments are more tightly controlled, MINOS and K2K are both able to measure the parameters of atmospheric oscillation with precision. MINOS's full data set [53] measures the atmospheric oscillation parameters as $\Delta m^2_A = 2.41^{+0.09}_{-0.10} eV^2$, with $\sin^2(2\theta_A) = 0.950^{+0.035}_{-0.036}$. In addition, MINOS is able to measure neutrino and anti-neutrino oscillations independently, though the parameters are found to agree for neutrinos and anti-neutrinos within experimental uncertainties.

Off-axis Neutrino Beams: T2K, NOνA

As one moves off of the axis of a neutrino beam, the flux from the beam decreases and narrows in energy. For an oscillation experiment, a mono-energetic and point-like neutrino source is ideal, and an off-axis neutrino beam is closer to this ideal situation. Both the T2K [54] and NOνA [55] experiments utilize this to study neutrino oscillations. In particular, since NOνA is fine grained detector, they are able to observe the appearance of electron neutrinos arising from $\nu_\mu \to \nu_e$ oscillations [56].

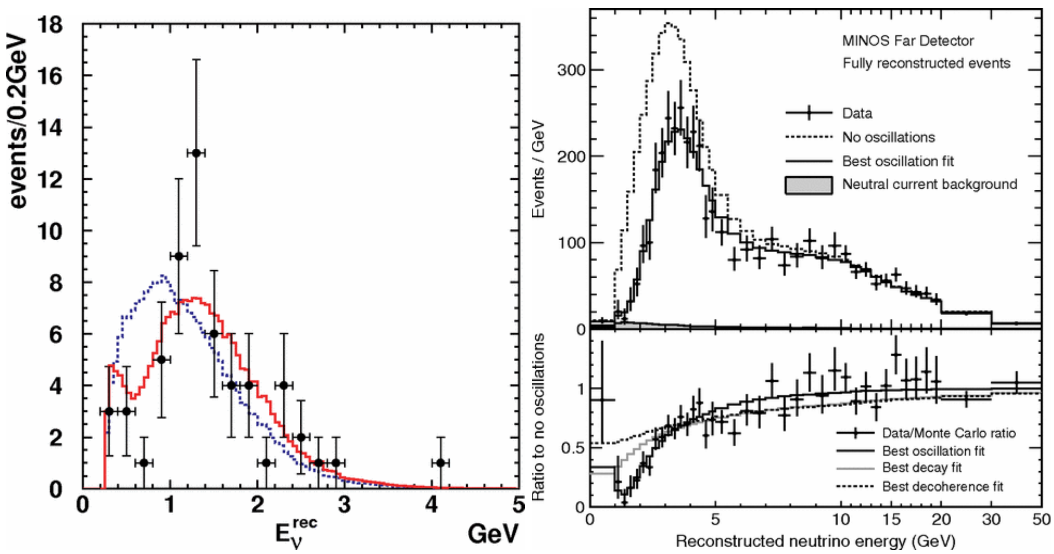

Figure 1.7: (Left) K2K Event spectrum. (Right) MINOS event spectrum. Both data sets clearly favor the oscillation hypothesis.

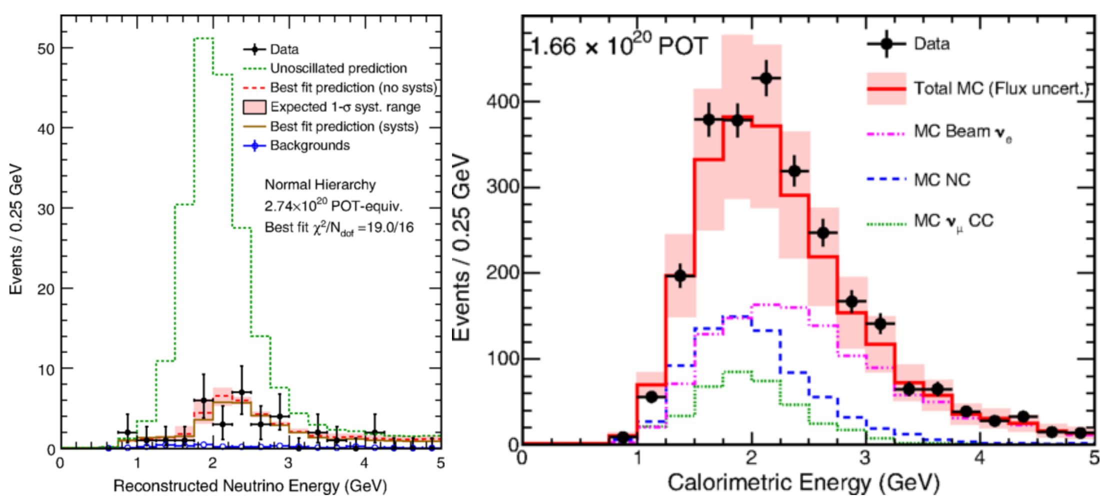

Figure 1.8: (Left) ν_μ Oscillation results. (Right) ν_e appearance oscillation results. Figures from [55] and [56].

Reactor Neutrinos and θ_{13}

The three neutrino oscillation paradigm requires three mass splittings (between the three neutrinos) and three mixing angles, however since it's observed that $\Delta m_{solar} = 7.6 \times 10^{-5}$, two of the mass splittings are effectively degenerate. Measuring the mixing angles is slightly more complicated, however, in the regime where solar neutrino oscillations are not yet relevant the parameter θ_{13} can be measured effectively. θ_{13} can be measured as non-zero from beam experiments such as MINOS, T2K and NOνA [57–59], but it is directly measurable by searching for electron neutrino disappearance. Nuclear reactors provide a high intensity flux of electron anti-neutrinos in the $\sim$ MeV range, so an experiment at around 1 km can probe $\bar{\nu}_e$ disappearance due to mass splittings in the range of $10^{-3} eV^2$.

The first experiment to actively search for $\bar{\nu}_e$ disappearance due to a nonzero θ_{13} mixing angle was CHOOZ [60] in France. CHOOZ found no evidence for non-zero θ_{13}, but set an upper limit on the mixing angle and proposed a follow up experiment to improve sensitivity to lower mixing angles [60].

In 2012, a suite of experiments measured a non-zero θ_{13}. Double-CHOOZ [61], Daya Bay [62], and Reno [63] all report significant observation of $\bar{\nu}_e$ disappearance from reactor neutrinos, and Daya Bay and Reno results were at the 5σ level. The latest results from Daya Bay [64] show that the measurement of θ_{13} is at precision levels. Though it is the last mixing angle measured, it is now the most well known.

1.3 Future Directions in Neutrino Physics

Neutrino oscillations are a well established phenomenon. Despite that, many properties of neutrinos remain elusive. Some of intriguing puzzles that may be resolved experimentally soon are, for example, the direct measurements of neutrino mass [14, 15] by precision measurements of tritium decay. Other experiments are probing whether or not neutrinos are their own anti-particle by searching for neutrino-less double beta decay [65–67]. Future

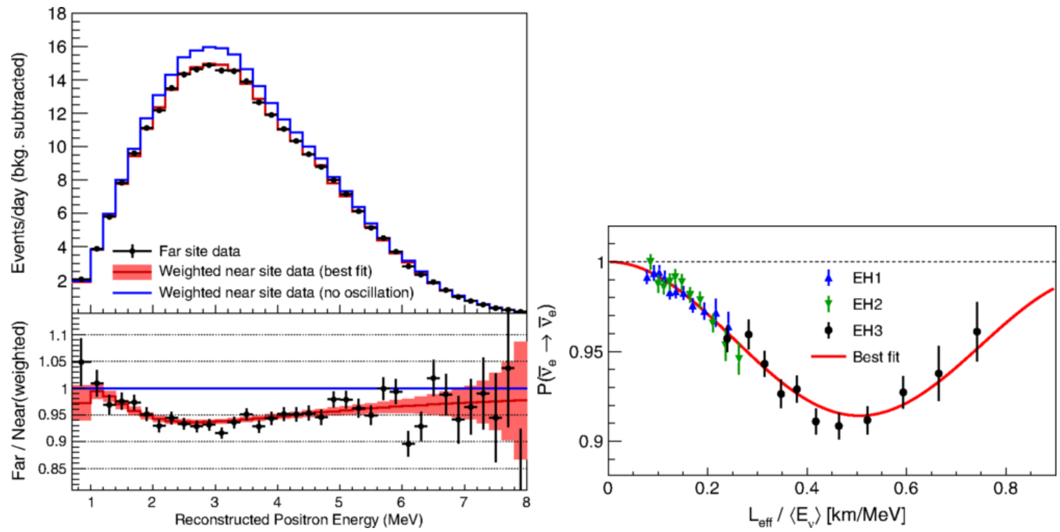

Figure 1.9: (Left) Daya Bay prompt energy spectrum, showing a clear deficit. (Right) Daya Bay survival probability, showing the characteristic oscillation pattern of neutrino oscillations.

experiments will be able to probe the mass heirarchy of neutrinos [25, 68] as well as search for CP violation in the neutrino sector [25, 69]. Undoubtedly, the next decade will produce very exciting results in neutrino physics.

Chapter 2

Neutrino Beams

Direct measurements of neutrinos have two parts: a source of neutrinos, and a detector to observe them. The most precise experiments required detailed knowledge of the workings of both the source *and* the detector. This chapter describes the important components of the Fermilab accelerator based neutrino beams. The Booster Neutrino Beam (BNB) is relevant to the Fermilab Short Baseline Neutrino Program, in Chapters 4 and 5. The Neutrinos from the Main Injector (NuMI) beam is relevant for the ArgoNeuT experiment in Chapter 6.

2.1 Accelerator Based Neutrinos

A popular source of neutrinos in modern experiments are the neutrinos from accelerator complexes. As of the writing of this thesis, there are three active neutrino beams: two at Fermilab [70, 71], and one in Japan [72]. Compared to other sources of neutrinos, accelerator based neutrinos offer some advantages.

First, neutrino beams made at accelerator complexes are designed, and not a by-product of other circumstances. This means that the design of the beam is often optimized for physics goals, in particular by tuning the energy spectrum and energy range of the neutrino beams. Combined with intelligent positioning of detectors, accelerator neutrino beams can be optimized to probe a vast range of oscillation signals.

The NuMI beam, described below, was designed to have three modes of running to cover an entire energy range from 1 to 20 GeV neutrinos. In general, accelerator based neutrino sources are crafted to build neutrino beams that will allow the neutrino experiments in the beam to maximize their physics output.

Another advantage to neutrino beams at accelerators is the pulse structure of the beam. Since accelerators, like Fermilab, make neutrino beams by colliding bunches of protons with a target material, the timing of the proton bunches provides a natural time structure to the neutrino beams. Downstream detectors can, using sufficiently time-sensitive detection material, "time-in" to the neutrino beam pulses to reject non beam backgrounds. For experiments on or near the surface, this is exceptionally important for rejecting cosmic backgrounds.

2.2 Fermilab's Accelerator Complex

At Fermilab, where two of the three active neutrino beams originate, much of the physics program is derived from the use of the proton beam that Fermilab produces. All of the proton beams, regardless of destination, start in the same location. A bottle of hydrogen provides a source of protons for the entire accelerator complex. In batches, some of the hydrogen atoms are given a negative charge by the addition of an electron, and these electrons are pushed into the Linear Accelerator (LINAC) at Fermilab with 750 KeV of energy (via a Cockroft-Walton generator). The LINAC accelerates the protons to 400 MeV, and at the end of the LINAC the protons enter the Booster, a synchrotron. Before entering the Booster, the electrons are knocked off of the H^- ion to ensure that only protons enter the downstream accelerator system. Over the course of thousands of rotations around the Booster, the protons are accelerated to 8 MeV of kinetic energy.

The Booster can nominally operate at 15 Hz, though is generally run at lower frequencies. Future upgrades to Fermilab's accelerator complex involve running the Booster at it's maximum rate to produce as many protons as possible. From the Booster, protons can be extracted to the Booster Neutrino Beam target, described below (Section 2.3). The majority of protons, however, enter the Main Injector to be accelerated to higher energies. The Main Injector can accelerate protons to 120 GeV.

At the time of writing, the majority of the protons from the main injector are used in the NuMI beam (Section 2.4), while some are used for fixed target experiments and test beams (beams made of pions or other particles, generally secondary or tertiary beams from the proton beam). At the time of the data collected for this analysis, however, some of the protons from the Main Injector were used to produce anti-protons for the Tevatron, and some were injected into the Tevatron directly. In the future, it's excepted that a large fraction of protons will be used for the muon campus (for mu2e and g-2 [32] [73]), and further protons will be used for the LBNF Neutrino Beam [74].

2.3 Booster Neutrino Beam

The Booster Neutrino Beam (BNB) is Fermilab's lower energy neutrino beam, and the primary beam of MiniBooNE, MicroBooNE, and the Short Baseline Neutrino Program (see Chapter 4). The BNB is one of the most well understood, extensively studied neutrino beams in existence, and has been running since the MiniBooNE experiment and is expected to run until past 2020.

2.3.1 Booster Neutrino Beam History

The BNB was designed for, and by, the MiniBooNE collaboration. MiniBooNE was a Cherenkov style detector, searching for electron neutrino appearance. Because the primary background for MiniBooNE was photons from neutral pion production in the detector, which come from higher energy neutrinos, the BNB flux was designed to suppress neutrinos with energy above ≈ 1 GeV.

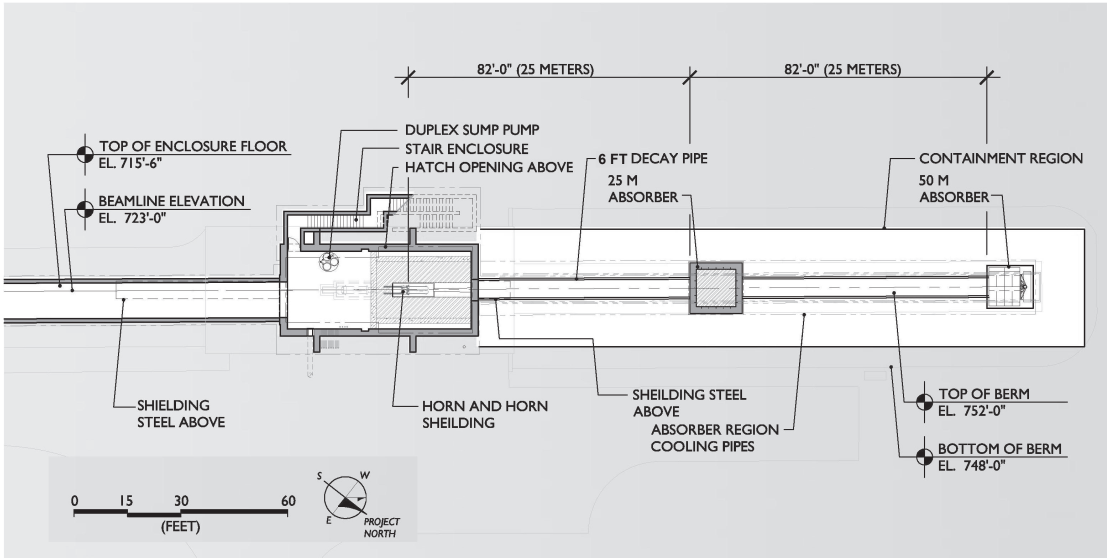

Figure 2.1: The Booster Beam target hall and decay pipe. Protons enter from the left, and hadrons decay in the decay pipe for up to 50m before the beam stop. MiniBooNE, MicroBooNE, and the other SBN experiments are to the right. Figure from [71]

The origin of the BNB is 8 GeV protons (8.89 GeV/c momentum) from Fermilab's Booster complex. These protons are transported to a Beryllium target, encased in a magnetic focusing horn. The protons collide with the Be and produce hadrons within the target, which are focused into the forward direction by the focusing horn. The hadrons enter a decay pipe of 50 meters, where they decay in flight into lighter particles including neutrinos. At the end of the decay pipe is a beam stop to prevent all particles (except neutrinos) from proceeding. A schematic of the proton entry, horn location, decay pipe and beam stop are shown in Figure 2.1.

The batches of protons delivered to the Booster target are pulsed, typically at a rate not more than 5 Hz, and each bunch is approximately 1.6μs in duration. For downstream experiments, such as MiniBooNE and the SBN Program, the ability to resolve interactions in the detector on the time scale of 1.6 μs is extremely useful for rejecting out-of-beam-time cosmics.

Each bunch of protons from the Booster typically contains approximately 4e12 protons. These protons collide with the Beryllium target, which is 71 centimeters long and made from seven segments of Beryllium. This length corresponds to 1.7 interaction lengths for the protons, meaning that just over 80% of the protons interact in the target material. The number of protons on target is measured upstream of the target by two magnetic toroids, and the uncertainty on the number of protons delivered is on the order of 1-3% typically.

Upon interacting, the protons produce lighter hadrons such as pions and kaons. The spectra of produced hadrons is the source of the largest uncertainty in the Booster Neutrino Beam, and is discussed in more detail in Section 5.3. The hadrons produced by the protons at the target are focused with the magnetic horn which produces an azimuthal, pulsed magnetic field in time with the proton delivery. The primary source of the neutrinos in the BNB is from decay in flight pions, though there is significant contamination from kaon decay and muon decay (where the muons are also the product of pion decay). The kaons and muons also produce a contamination of electron neutrinos in the primarily muon neutrino beam, and this flux of electron neutrinos is the primary background in the Short Baseline Neutrino Program's ν_e appearance analysis (see Section 4.4.2.

The estimation of the flux, by neutrino type and by originating particle, at the MiniBooNE location can be seen in Figure 2.3. This estimate of the flux is produced with a sophisticated Monte Carlo simulation, discussed in detail in [71]. However, the general procedure is:

1. Define the beamline geometry, including the shape, location, and composition of the components of the BNB. This includes the target, magnetic horn, decay pipe and beam stop as well as the other minor parts. The simulation attempts to capture the reality of the beam construction as closely as possible. A graphical representation of the magnetic focusing horn can be seen in Figure 2.2.

2. Generate protons in the simulation that match the expected protons from the beam, accounting for the optical effects of the beam upstream of the target.

3. Simulate the interaction of protons in the target and surrounding material. Substan-

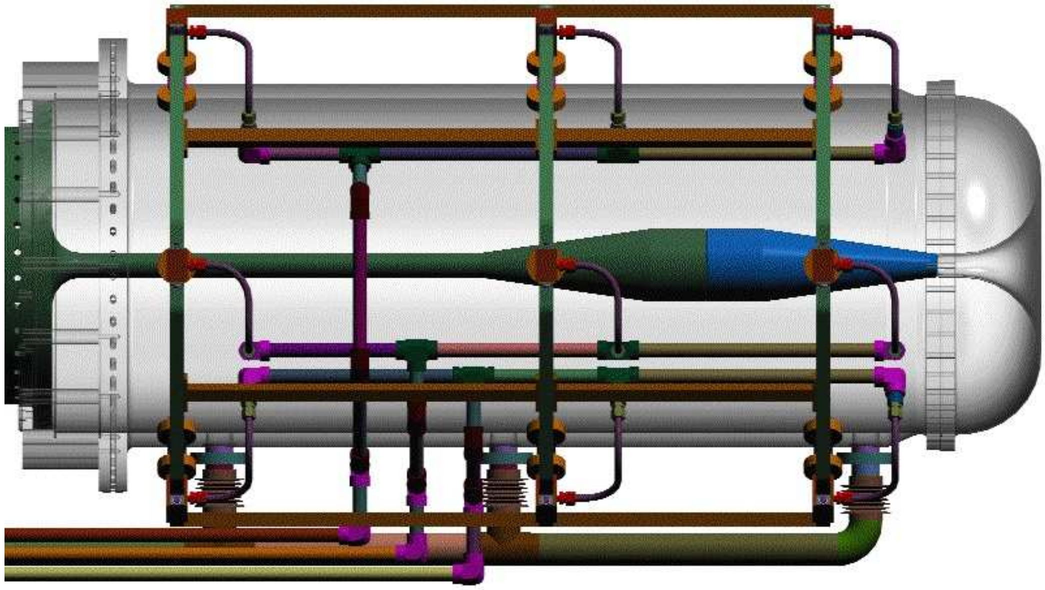

Figure 2.2: The Booster Beam horn and focusing magnet. Figure from [71]

tial effort was made by the MiniBooNE collaboration to constrain this step of the simulation, as it is the primary source of systematic uncertainties in the beam model. Dedicated experiments, such as HARP [75] and BNL E910 [76], are used to constrain pion production and improve the flux prediction, as the uncertainties in pion production dominate the flux uncertainties.

4. Propagate particles from the primary interactions using GEANT [77] to account for energy loss and interactions that change the kinematics of the particles above. This also includes accounting for the focusing effects of the magnetic horn.

5. Identify particles that result in neutrinos at the detector, accounting for branching ratios and kinematic distributions properly. Statistical boosting techniques are also used, since the solid angle subtended by the neutrino detector is small in the lab frame of the decaying particles.

The work covered in this document does not use the MiniBooNE detector at all, however it does leverage the MiniBooNE flux calculation machinery to simulate the flux at mul-

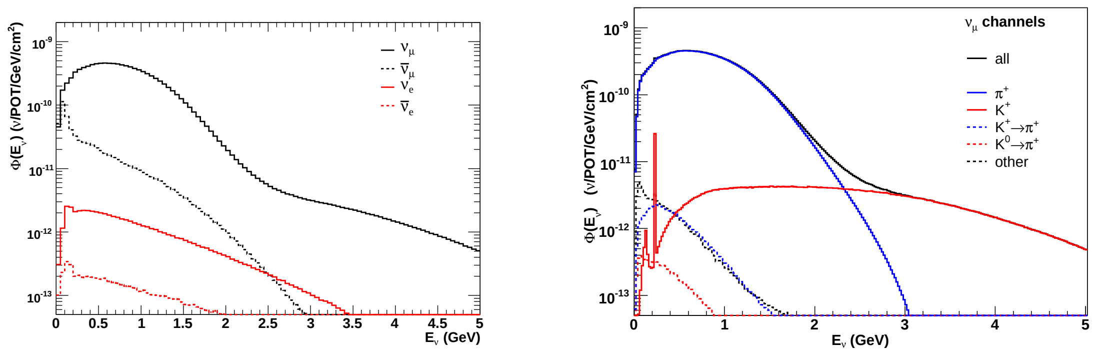

Figure 2.3: (Left) Total predicted flux at the MiniBooNE detector by neutrino species with horn in neutrino mode. (Right) Muon neutrino flux by type of original particle. Figure from [71]

Table 2.1: Fractional flux uncertainties, by species of neutrino, from the MiniBooNE flux calculation.

Source Of Uncertainty	ν_μ	$\bar{\nu}_\mu$	ν_e	$\bar{\nu}_e$
Proton Delivery	2.0%	2.0%	2.0%	2.0%
Proton Optics	1.0%	1.0%	1.0%	1.0%
π^+ Production	14.7%	1.0%	9.3%	0.9%
π^- Production	0.0%	16.5%	0.0%	3.5%
K^+ Production	0.9%	0.2%	11.5%	0.3%
K^- Production	0.0%	0.2%	2.1%	17.6%
Horn Field	2.2%	3.3%	0.6%	0.8%
Nucleon Cross Sections	2.8%	5.7%	3.3%	5.6%
Pion Cross Sections	1.2%	1.2%	0.8%	0.7%

tiple locations for the Short Baseline Neutrino Program, shown in Figure 2.4. In this light, the discussion of the systematic uncertainties of the flux prediction are left to Section 5.3. However, Table 2.1 is included here to showcase the precision at which MiniBooNE constrained the BNB, an accomplishment that future experiments are building upon.

2.4 Neutrinos from the Main Injector (NuMI Beam)

The Neutrinos from the Main Injector (NuMI) beam was conceived of with the MINOS (Main Injector Neutrino Oscillation Search) experiment at a time when neutrino oscillation parameters were not well constrained. In particular, there were hints that the atmospheric

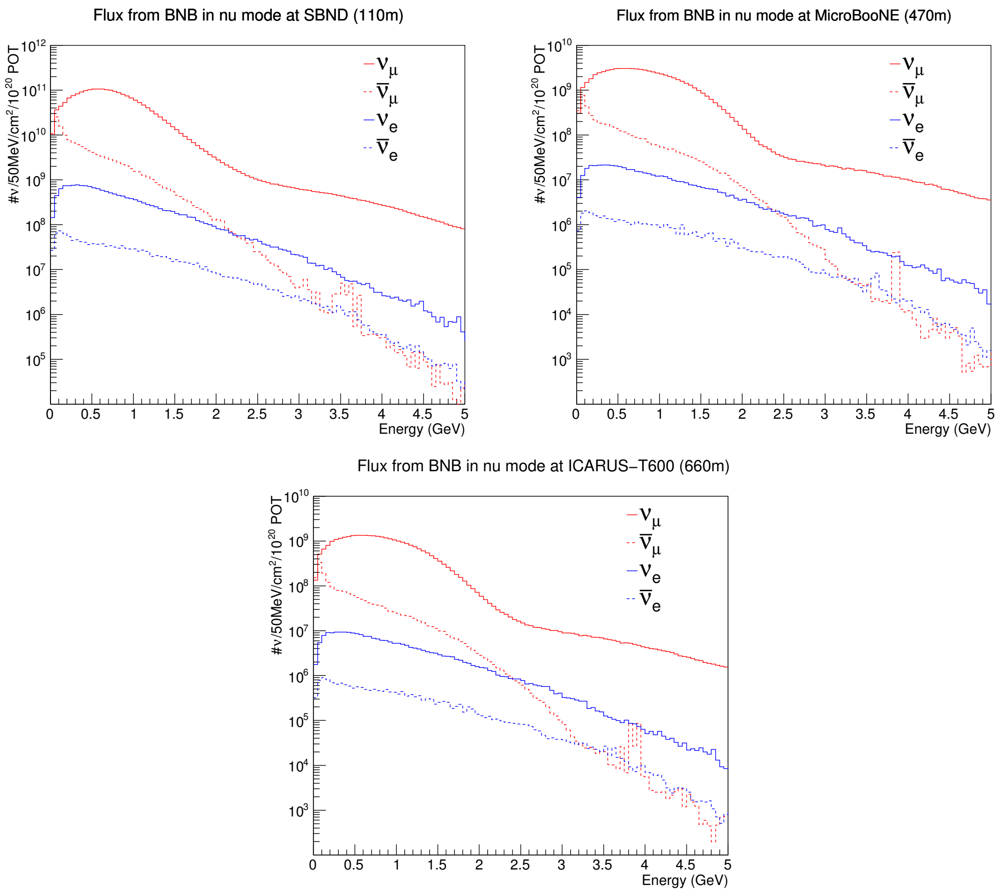

Figure 2.4: The neutrino flux from the Booster Beam at the three locations of the SBN Program. The flux falls at approximately $1/r^2$, however, the near detector flux is slightly distorted due to its proximity to the decay pipe.

mass splitting was of the order of magnitude of $10^{-3}eV^2$, but more than that was unknown. Therefore, the NuMI beam was designed to be configurable and to run in multiple modes of running: Low Energy, Medium Energy, and High Energy. The various energy spectra are shown in Figure 2.5. A comprehensive discussion of the design and operation of the NuMI beam is available in Ref. [70]. This section will be a very brief summary of some important facts about the NuMI beam.

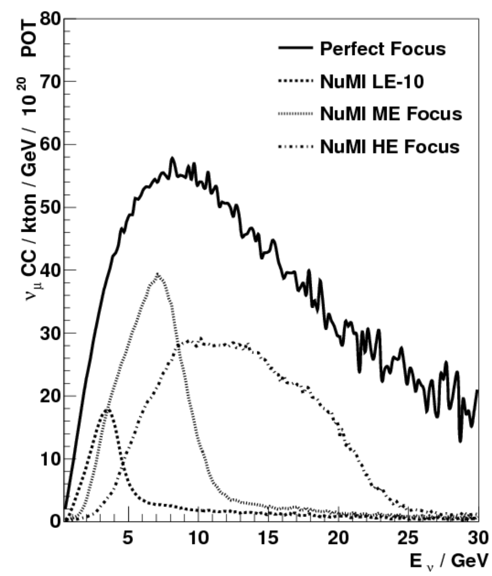

Figure 2.5: The various energy tunings for NuMI. The analysis performed for this work is based off of the Low-Energy mode, mainly in anti-neutrino mode.

The NuMI target is similiar to the BNB target, above, though it is more complex for several reasons. First, the distance between the target itself and the focusing horns is adjustable to allow the different running configurations. Additionally, there are two focusing horns instead of just one. The first horn, located close to the target, and the second horn, downstream, effectively act as a charged hadron focusing system. With a higher energy source of protons compared to the BNB, the two horns are necessary to focus the higher energy secondary particles from the target. Downstream of the target and horn area is the NuMI decay pipe, which is 675m in length. After the decay pipe there is 240m of rock, followed by the near detector for MINOS. ArgoNeuT, the detector that collected the data of this thesis, is located in the MINOS near detector hall in between MINOS and Minerνa. The schematic of the target, horn, and decay pipe are shown in Figures 2.6.

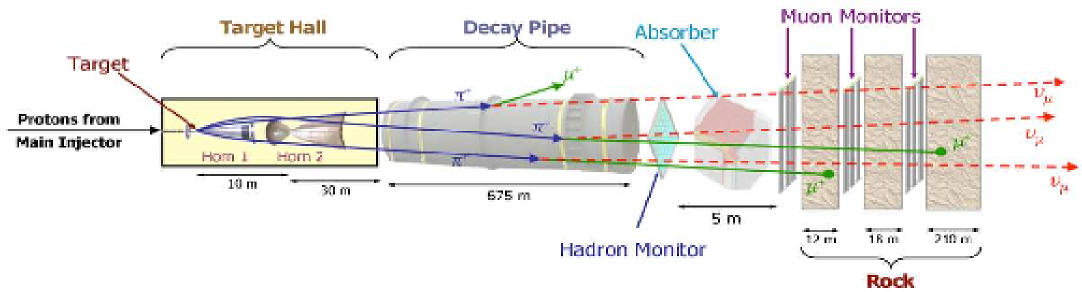

Figure 2.6: The beam target, horns, and decay pipe are shown for NuMI.

The NuMI flux is simulated with a FLUKA simulation in a way very similar to the BNB. It also benefits from the constraints from dedicated hadron production experiments [78,79], and in situ measurements from the detectors along the beam line [80]. The flux models in the simulation of the beam are generally accurate to with 10 or 20%, however experimental constraints and flux tunings can decrease the uncertainty to less than 10% [80]. The flux shown in Figure 2.7 is the computed ArgoNeuT flux without the addition of the constraints, in the NuMI Low Energy mode. Since the result presented in this thesis is not a cross section measurement but a detection of electron neutrinos, the tuned flux is unnecessary precision for this result.

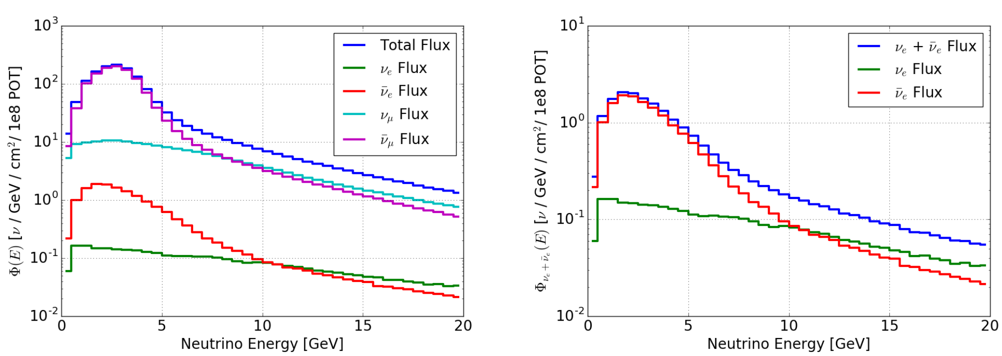

Figure 2.7: The predicted flux at ArgoNeuT. (Left) All flavors of neutrino species. (Right) Only the electron neutrino and anti-neutrino flux.

Chapter 3

Liquid Argon Time Projection Chambers

3.1 Time Projection Chambers

The Time Projection Chamber, abbreviated TPC, is a revolutionary particle detector concept first proposed in 1974 by David Nygren at Lawrence Berkeley National Lab. Since then, the TPC has found applications in a broad array of particle physics experiments such as collider experiments at the LHC [81, 82], precision measurements of muon properties [83], dark matter experiments [84, 85] and more. The abundance of uses for the TPC technology stems from the versatile and robust ability of a TPC to track charged particles.

In general, a Time Projection Chamber is a volume filled with some neutral and inert material. Commonly, noble gases and liquids are used though this is not required. An electric field is applied to the entire medium, and in some cases a magnetic field is applied as well. The electric field is generally applied by using a high voltage cathode as one surface of the detector. The opposing surface, the anode, is typically instrumented with readout equipment.

Time Projection Chambers are designed to observe electrically charged particles. In particular, a high energy charged particle (such as an electron, muon, pion, proton, etc.) can travel through the detector medium and will ionize the substance as it passes through, leaving a trail of electrons and ions. The applied electric field, emanating from the cathode, serves to separate the ionization electrons from the ions and move the electrons towards the anode of the detector. The drifted electrons form the basis of the measurement of the particle. In particular, they appear as a projection of the original track onto the anode of the detector, and the distance from the anode is determined by the time it took for the electrons to drift. Hence the name, Time Projection Chamber.

3.2 History and Liquid Argon Time Projection Chamber Concepts

The Liquid Argon Time Projection Chamber (LArTPC) was invented in 1974 by Bill Willis and Veljko Radika [86], and initially proposed for neutrino physics in 1977 by Carlo Rubbia [87]. At the time of its conception, neutrino physics was dominated by bubble chamber detectors like Gargamelle [88], renowned for it's remarkable resolution of particle topologies. Initially, the LArTPC was proposed as a way to combine high spatial resolution detectors with calorimetry measuring detectors in a way that is scalable to massive detectors. As the field of neutrino physics approaches the largest LArTPC to date with DUNE [74], it's worthwhile to recall the original advantages of the LArTPC technology as laid out in 1977 [87]:

- **"It is dense"**: The relatively high density of liquid argon, at 1.4 g/cm^3, provides a sufficiently high neutrino interaction rate such that high statistics measurements are feasible.

- **"It does not attach electrons and permits long drift times"**: As a long drift time is essential to large scale detectors to both maximize the mass of the detector and minimize the number of readout channels, the fact that argon itself does not attach free electrons is an essential ingredient to LArTPCs.

- **"It has a high electron mobility"**: The high mobility makes drifting electrons from particle ionization in a short time a feasible task.
- **"It is cheap"**: A detector can not be scaled to massive sizes unless the fundamental building block of the detector is affordable.
- **"It is easy to obtain and purify"**: Purification challenges have largely been overcome for LArTPCs. In particular, the MicroBooNE experiment has demonstrated a viable way to achieve high purity argon without purging the detector of impurities first.
- **"It is inert and can be liquified with liquid nitrogen"**: This makes the cryogenic systems for LArTPCs reasonable to purchase and implement.

40 years after the original proposal, it is remarkable how relevant the initial advantages remain in the face of an experiment such as DUNE.

Since the original proposal, some additional advantages of LArTPCs have been noted and are worth mentioning. For example, the scintillation of Liquid Argon has been successfully characterized [89] and is measurable in coincidence with the drift ionization. For large detectors, especially surface detectors, this allows the ability to match scintillation light to ionization tracks to reject out of time events such as cosmic particles. It also allows the implementation of a hardware based trigger to filter neutrino interactions online. For even modest sized LArTPCs, this can be an essential aspect to control data rates and ease computing requirements.

3.3 Design of LArTPCs

As mentioned above, the Liquid Argon TPC has a long history of development. This section presents the details of a modern LArTPC in it's design, given in the context of the ArgoNeuT detector. A comprehensive and detailed description of the ArgoNeuT detector is given in [90].

3.3.1 ArgoNeuT Time Projection Chamber

The ArgoNeuT experiment was the first LAr-TPC in a neutrino beam in the U.S., the first LAr-TPC in a low energy neutrino beam ever, and the start of the Fermilab and U.S. LAr-TPC program. It was initially proposed as a test experiment to study the performance of a LAr-TPC in a neutrino beam, but has since produced a number of critical physics papers that were firsts of their kind. ArgoNeuT made the first measurements of muon neutrino cross sections on argon [91, 92], it characterized the response of the detector to several types of particles [93, 94], and has made high impact measurements of short-range correlated pairs and back to back protons [95], and coherent pion production [96].

The ArgoNeuT TPC is a rectangular volume of liquid argon that measures 40 cm high (Y direction), 47 cm wide (X direction), and 90 cm long (Z direction). In total, this corresponds to about 170 liters of Liquid Argon. In its running configuration, neutrinos from Fermilab's NuMI beam (See Section 2.4) enter nearly parallel to the Z direction, with a slight downward direction. On the left side of the detector in the beam direction is the high voltage cathode, providing a uniform electric field of 500 V/cm throughout the TPC (corresponding to approximately -23 kV of voltage at the cathode). Opposite the cathode is the anode, composed of three wire planes, of which only two are instrumented for readout.

In the detector, as a neutrino interacts it produces outgoing particles, most commonly: muons, protons, neutrons, pions (charged and neutral), photons and electrons. Naturally, the possible particles produced in a neutrino interaction is much broader than this short

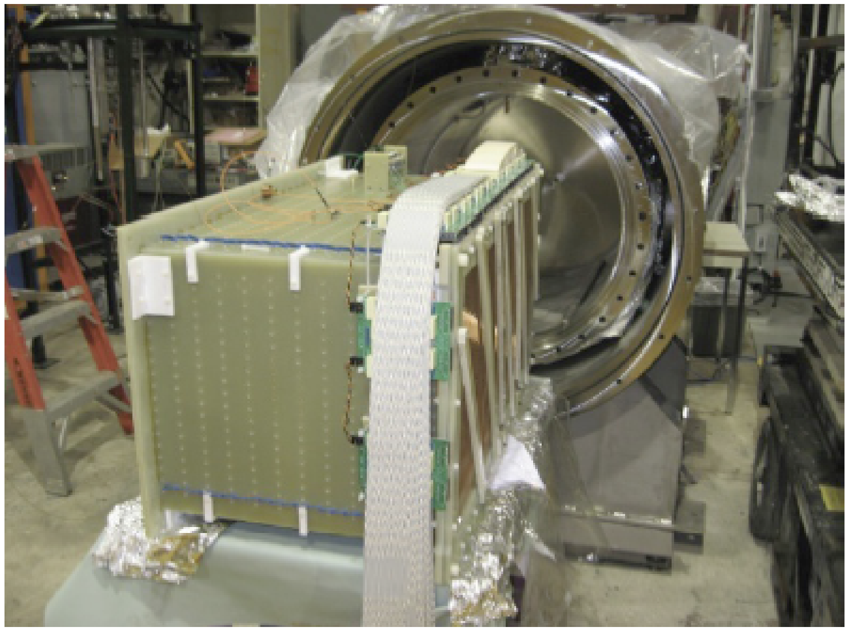

Figure 3.1: The ArgoNeuT TPC positioned just outside of its cryostat. The wire planes and the readout electronics are visible on the right side of the TPC.

list, but this comprises some of the most frequent particles. In the case of the electrically charged particles, the particle will ionize the argon atoms as it moves through the detector. The ionization produced is a statistical quantity, but the average expected ionization depends strongly on the momentum and mass of the particle in question. In general, particles with higher mass and lower momentum produce larger ionization per unit distance traveled [97]. The ionization per unit distance, measured most frequently in the units MeV/cm, is a very powerful tool for calorimetric identification of particles (as demonstrated in Chapter 6).

Neutral particles, such as neutrons and photons, do not ionize the argon atoms as they traverse the detector. However, these particles can still interact with the argon and produce charged particles visible to the TPC instrumentation. Neutrons frequently will scatter off of an argon nucleus and produce a recoiling proton, which can be observed in the detector. Photons can produce electromagnetic showers through Compton scattering and pair production, described more fully in Chapter 6.

After the particles from the neutrino interaction have produced ionization in the detector, the electric field separates the ions and electrons from each other. The separation is imperfect and depends on the strength of the electric field, the amount of ionization, as well as the angle of ionization with respect to the field. This effect, known as recombination of electrons and ions, has been studied in detail in the ArgoNeuT detector [94]. In general, this effect causes a quenching of the observed electrons compared to the true ionizing power of the high energy particles as seen in Figure 3.2.

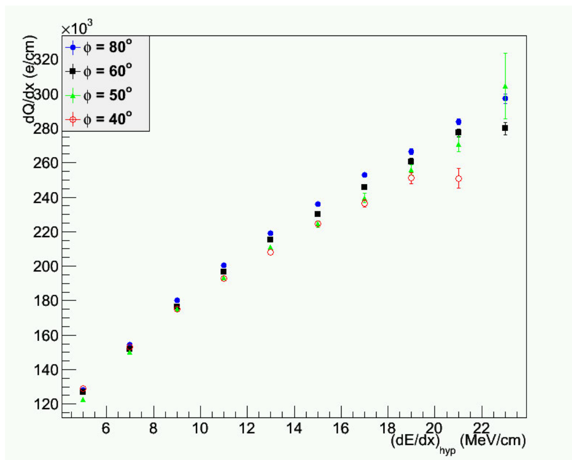

Figure 3.2: Measurement of the recombination effect in ArgoNeuT using stopping protons, at 500 V/cm. [94]

The uniformity of the electric field in the ArgoNeuT detector is maintained with a system of field shaping electrodes. The electrodes are plated on to the interior surface of the volume between the cathode and anode, and are held at a voltage linearly decreasing from cathode to anode. In ArgoNeuT, the field shaping strips are 1cm wide and separated by 1cm, and there are 23 strips total. This technique, however, is utilized in a variety of TPC experiments.

Once the electrons have been separated from the ions, they drift towards the readout wires of the TPC. Though argon itself does not attach electrons, impurities in the argon can do so. The amount of drifting electrons declines as a function of the distance they have to drift. This decline is well modeled with an exponential decline, and the decay constant is referred to as the electron "lifetime." Proper calorimetry must take the lifetime of the electrons into account on hit by hit basis to correctly account for the effect of the impurities in the liquid argon. In ArgoNeuT, the electron lifetime is measured in data by comparing the amplitude of hits from crossing muons at different drift distances as seen in Figure 3.3.

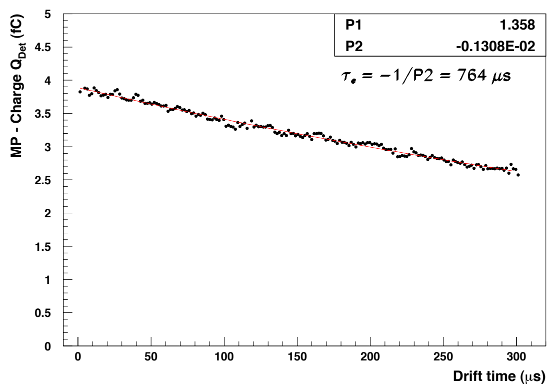

Figure 3.3: The electron lifetime in ArgoNeuT is computed run by run empirically, using a sample of depositions in the TPC from minimally ionizing particles. Shown here is the fit, using an exponential, for run 648 giving an electron lifetime of 742 $\pm\mu$s (statistical error only).

The ArgoNeuT detector has three planes of wires at the anode, two of which are instrumented. The first plane, composed of 225 wires oriented vertically, serves as a shielding plane for the other wires and to provide shaping to the electric field through the TPC. The three planes are spaced with 4 mm between each other. The second plane, referred to as the "induction plane," contains wires that are set at +60^{o} to the beam axis. As electrons cross the shield plane, they approach the induction plane wires. The wires are electrically biased, however, such that the electrons drift around the individual wires. The approaching and subsequent passing of electrons induces a current on these wires (hence the name "induction plane") and the bipolar pulse shape is recorded by the readout electronics for wires that observe electrons. See figure 3.4 for examples of this pulse.

The final set of wires, dubbed the "collection plane," is biased such that it collects the drifting electrons onto it and they are observed as a pulse of charge by the electronics system. The collection plane is set at an angle of -60^{o} to the beam direction. The two instrumented planes each have wire spacings of 4mm, and sample at 5.05 MHz. In total, the instrumented planes have 240 wires in each plane. Since the wires are at an angle with respect to the TPC axes, not all wires are of the same length. Most wires, 144 of 240 in each plane, are 46.2 cm long. The shortest wires are 3.7 cm long.

The sense wires are readout with a system of electronics sampled every 198 ns, and the readout system has a sensitivty of 7.49 ADC/fC of charge recorded. This gives a signal to noise ratio of 15 or higher for minimally ionizing particles in the TPC. An in depth description of the ArgoNeuT readout electronics is available in [90]

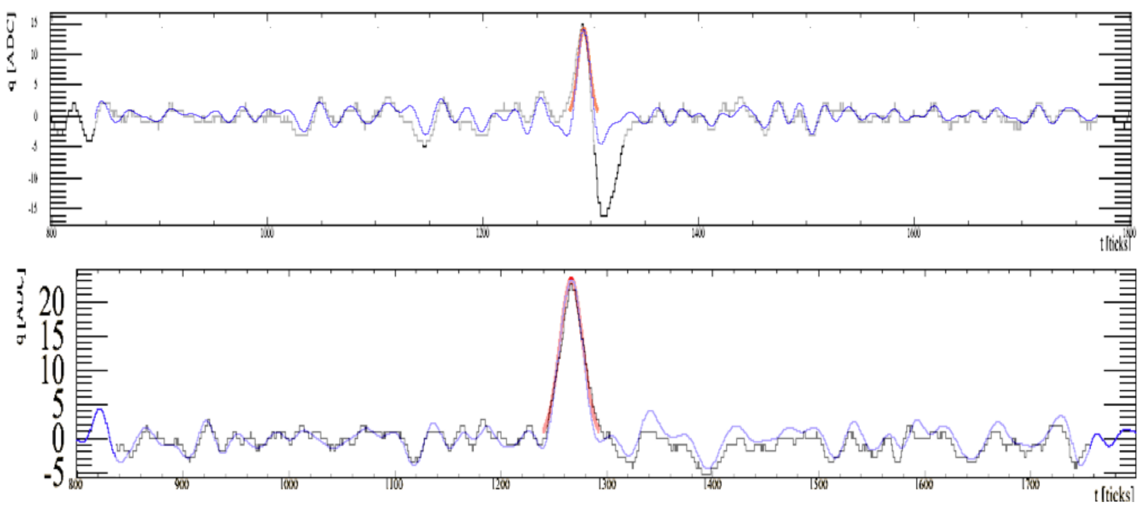

Figure 3.4: Raw and deconvoluted signal shapes from the ArgoNeuT detector. On the top is shown the induction pulse. The bipolar shape of the pulse in the induction plane is corrected during the deconvolution stage. On both planes, a Gaussian hit fitting technique is used to determine the amount of charge recorded. Figure from [90].

3.4 Event Imaging and Reconstruction

One of the prime advantages of a LAr-TPC to other neutrino detection technologies is the ability to do precision imaging *and* calorimetry. In this section, the standard chain of reconstruction algorithms is described to show how the high resolution images are transformed into high level, particle physics data.

Each wire in the detector measures a signal of electrons as they drift, as a function of time. When the wires are arrayed in an image in sequential order, such that the x axis is wire number and the y axis is time tick, 2D images are formed such as in figure 3.5. As seen in figure 3.6, the wire planes represent projections of the 3D data onto a plane that is orthogonal to the wires themselves.

3.4.1 Deconvolution

The reconstruction of these images into a 3D event starts at the lowest level, filtering and deconvolution of the wire signals. In general, the number of electrons recorded by a given wire as a function of time is not perfectly matched by the ADC signals read out by the detector, due to the response of the detector electronics and noise effects.

To correct for this, a deconvolution process is applied to each wire. As seen in figure 3.7, the response of the detector to a delta function introduces a spread of signal which is removed using a scheme with the Fast Fourier Transform. The response of each channel is measured with external pulse generators. The convolution theorem then allows the removal of the detector response by taking the inverse Fourier transform of $\frac{v[t]}{r[t]}$, where $v[t]$ is the Fourier transform of the recorded waveform and $r[t]$ is the Fourier transform of the channel's response. Figure 3.4 shows the result of applying deconvolution to ArgoNeuT data in the collection and induction planes. In addition, the deconvolution for the induction plane removes the bipolar behavior to make hit finding easier.

3.4.2 Hit Finding

For each wire in the detector, a hit finding algorithm is used to locate the regions of the readout with electron deposition signals. While there are several different hit finding algorithms available in LArSoft [98], the official LArTPC reconstruction software, they all follow a generalized procedure.

First, a deconvolved (and noise filtered) wire signal is scanned for regions of signal above a specified threshold. The baseline threshold of hit finding depends on whether the

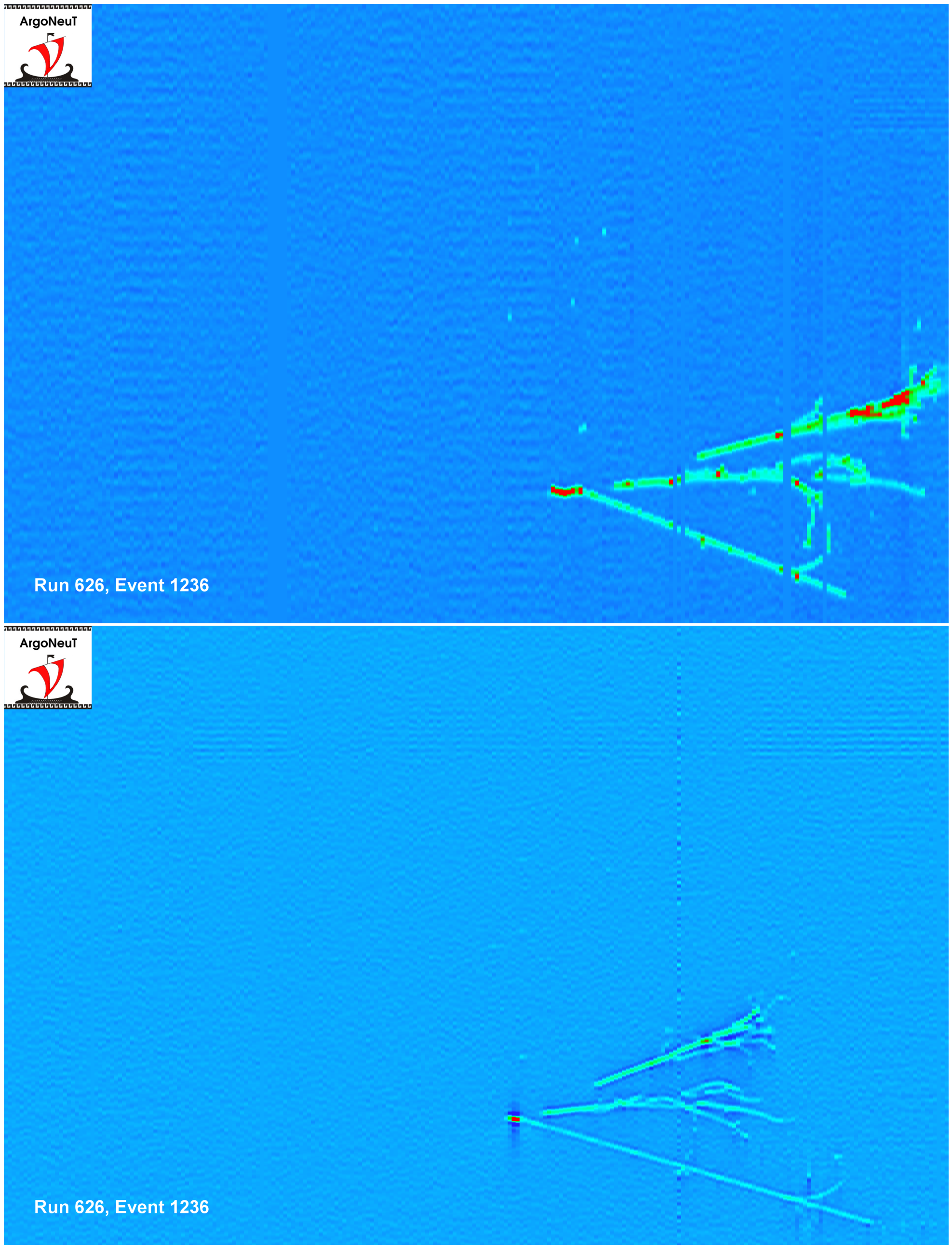

Figure 3.5: Full Resolution ArgoNeuT data. The horizontal direction, from left to right, represents increasing wire number. The vertical direction is the drift distance, with the wires at the bottom of the picture. An artificial color scale is applied to highlight depositions of charge above noise levels. The top image is the collection plane, and the bottom image is the induction plane. The wire signals here are deconvolved, which removes the bipolar shape of the induction pulse.

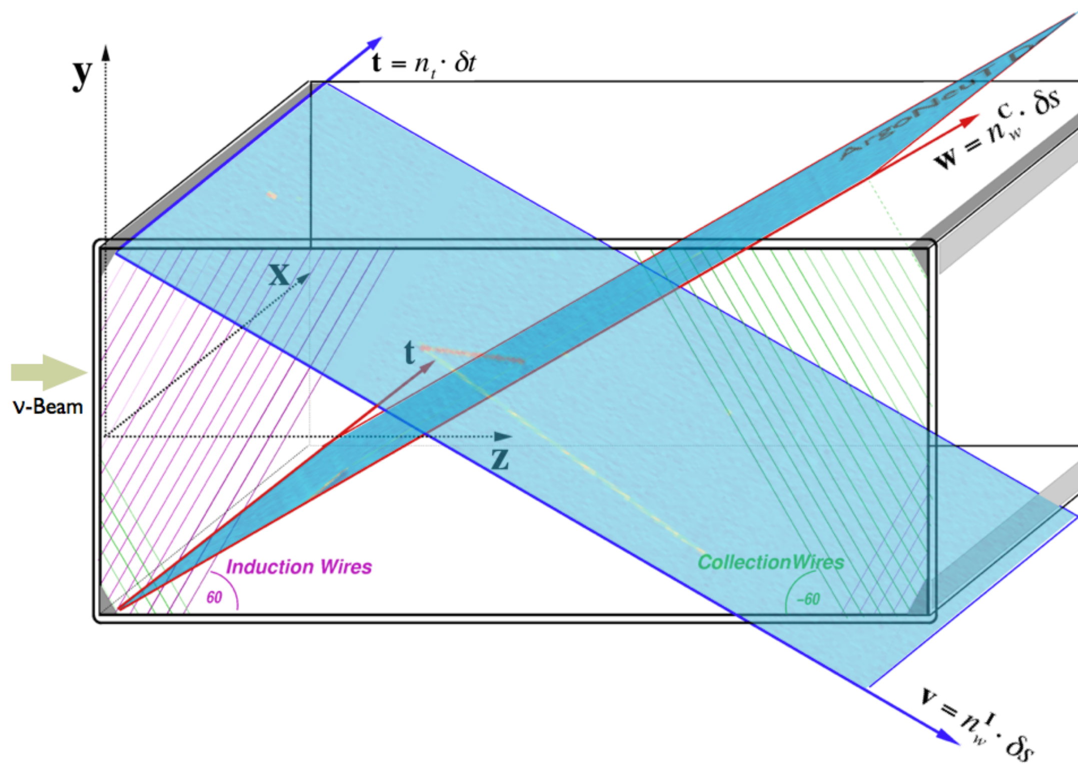

Figure 3.6: Representation of the projection of the LArTPC in ArgoNeuT. The wire and time axes give a 2D image that represents a projection of the 3D charge depositions on to the 2D surfaces shown in blue. Figure from [90].

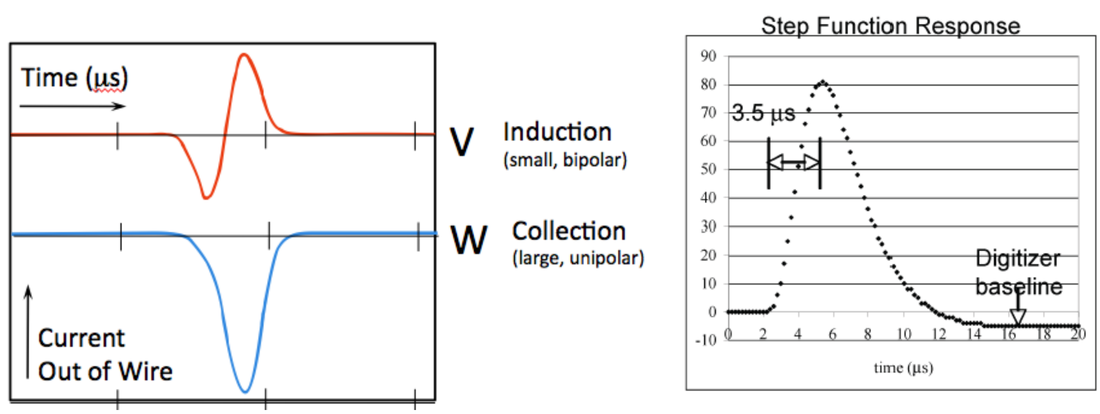

Figure 3.7: On the left, an image of the idealized detector response to drift electrons in the induction and collection plane. On the right, the response of the electrons filter and digitization to a delta function pulse. Figure from [90].

signal is from collection or induction planes, as the two planes have different Signal to Noise ratios.

Next, the regions of interest are fitted with an analytic function to allow a precise determination of the time tick, peak, and integral of the charge deposited. The most common function used is a Gaussian. In some cases, and commonly in neutrino interactions, hits that are close to each other from different particles will have overlapping regions. In this case, the multiplicity of the region above threshold can be determined to help tracking algorithms accurately distribute hits between different particles. An example of this is seen in Figure 3.8. In general, complicated regions with multiple hits are fit with several Gaussian functions summed together.

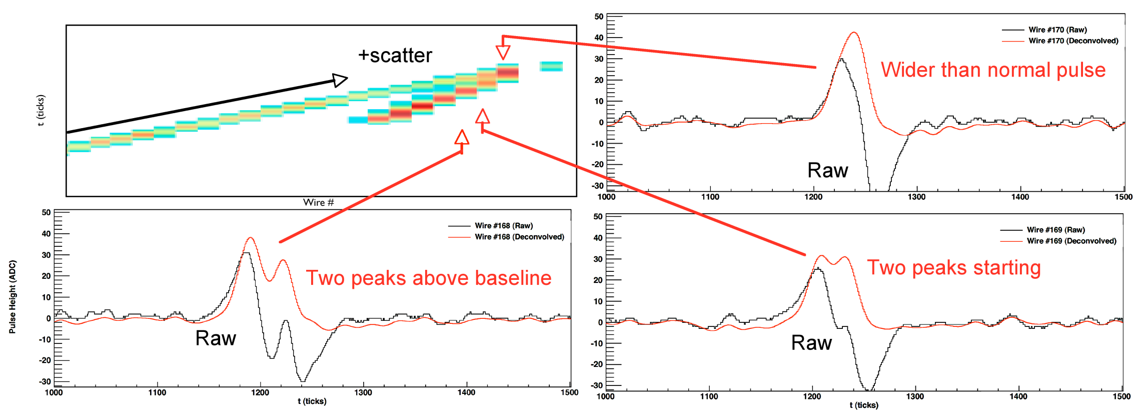

Figure 3.8: A neutrino vertex as seen in the induction view in ArgoNeuT. The top left shows the reconstructed signals above threshold. The other figures show the wire signal moving away from the vertex: the initial signal is wider than normal, and as the tracks diverge in the detector the two peaks are resolved. Figure from [90].

3.4.3 Cluster, Tracking and 3D Reconstruction

Once the wire signals have been deconvolved, and the signal depositions have been reconstructed as hits, a number of higher level steps remain between hits and physics data. First, hits must be grouped together based on which particle they originated from. In general, this is an *extremely* difficult problem with no simple answer. For particles like muons and protons, which produce simple, linear tracks of hits in the detector, it is not impossible and a lot of progress has been made. For more complicated events, such as electromagnetic showers and deep inelastic scatter events, clustering remains the weakest point of the reconstruction chain.

For a track like particle, in general, the groups of hits are associated together into clusters by finding sets of hits that are well aligned linearly. These clusters are then matched across the planes of the detector (two planes in ArgoNeuT, but many state of the art detectors have 3). Though the planes offer different projections of the 3D events into 2D, the drift direction (vertical direction in 3.5) is a common axis in every projection. Therefore, the most useful metric to determine if two clusters are from the same track in the argon is the time it took those clusters to drift to the wires.

Once clusters from multiple planes have been matched together, the wire information between the two clusters can be used to determine where in the Y-Z plane the clusters overlap. This is because each wire intersects the other plane's wires at most once, so if a charge deposition from one plane is matched to one on another plane, it uniquely determines the location of the 3D charge (The X coordinate comes from the drift time).

Almost all of the details of 3D tracking and reconstruction have been abbreviated here, as they are not crucial to the work presented in this thesis. However, a great detail of knowledge and techniques is reported in many references [99, 100].

3.4.4 Calibration

For a LAr-TPC to perform physics studies with calorimetric information, it is essential to accurately calibrate the detector response to charge depositions on the wires. For ArgoNeuT, this was performed with large sample of crossing muons as reported in [93]. That analysis demonstrated that muons induced from upstream interactions (known as "through-going muons" in ArgoNeuT) can be used as a known source of ionization in the detector, as shown in Figure 3.9. For ArgoNeuT, the mean momentum of the through-going muons

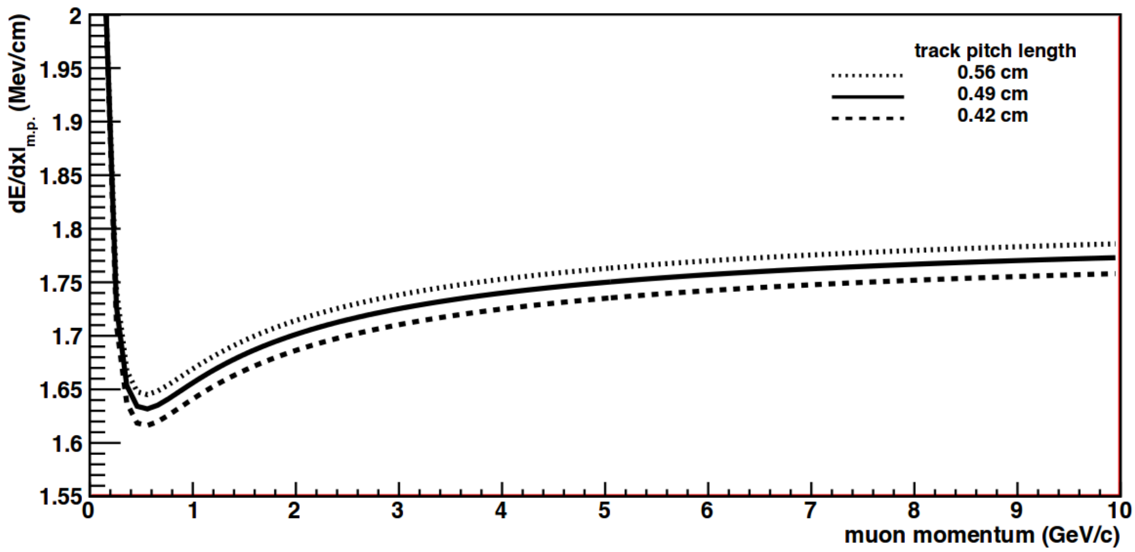

Figure 3.9: Most probable ionization amounts for muons traversing liquid Argon, as a function of momentum.

was estimated at 7 GeV/c.

To calibrate the detector from a sample of muons, the dE/dx of each deposition measured by the wires of the TPC can be collected into a histogram and the shape is fit with a Gaussian-convolved Landau distribution, as demonstrated in Figure 3.10. If the most probable value of the distribution, which is a parameter of the fit, is observed to be different from the target value (1.73 MeV/cm), the calibration constants are adjusted. This process repeats until the calibration constant produces a distribution of hits that agrees with theoretical values of ionization per centimeter.

Unlike [93], there are two differences in the calibration used in the analyses described in Chapter 6. First, the calibration constants are calculated on a wire-by-wire basis, instead of for the entire detector. Second, the calibration constants are calculated for both the collection and the induction plane, instead of just the collection plane. Due to advancements in deconvolution and hit finding since the original publication of the ArgoNeuT calibrations, the induction plane can now be shown to be a usable plane for calorimetry, as seen in Figure 3.11. The two planes show agreement in the calorimetric values calculated

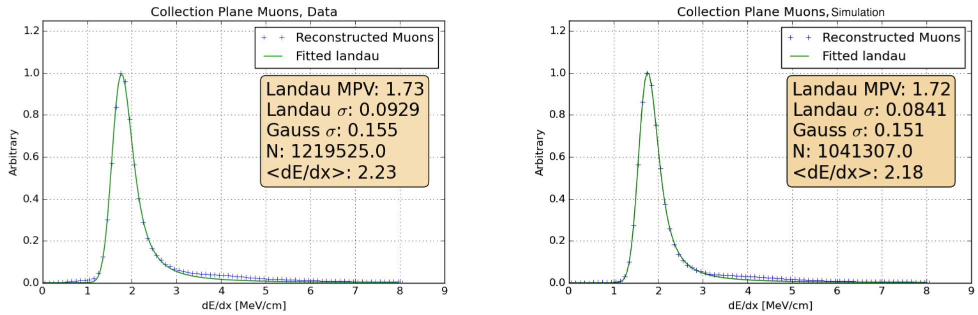

Figure 3.10: Most probable ionization amounts for muons traversing liquid Argon, as a function of momentum. Data are shown on the left, with simulation results on the right.

for the crossing muons. In the end, the average calibration constants for each plane are determined to be 36.4 $\pm$ 2.48 [fC/(ADC*tick)] for the collection plane, and 143 $\pm$ 10.3 [fC/(ADC*tick)].

3.4.5 Particle Identification and Calorimetry

In a LArTPC, the calorimetric identification of particles is based upon the behavior of charged particles moving through the argon. The energy deposited per centimeter is dictated by the Bethe-Bloch equations, and the properties in argon of common particles are seen in Figure 3.12.

As a particle loses energy, it's amount of ionization decreases until it reaches a minimum before the ionization spikes to very high values. Due to the limited resolution of the detector, however, the observed dE/dx values for a given particle will increase as the particle comes to a rest. As seen in Figure 3.13, this measure of dE/dx versus residual range allows calorimetric separation of particles. In particular, protons are easily separated from muons and pions with this measure.

Since LArTPCs also offer bubble chamber quality images, the topology of an event can give excellent ways to distinguish particles. As seen in Figure 3.14, particles like muons and pions that are difficult to distinguish with calorimetry can often be separated based on subsequent interactions within the TPC.

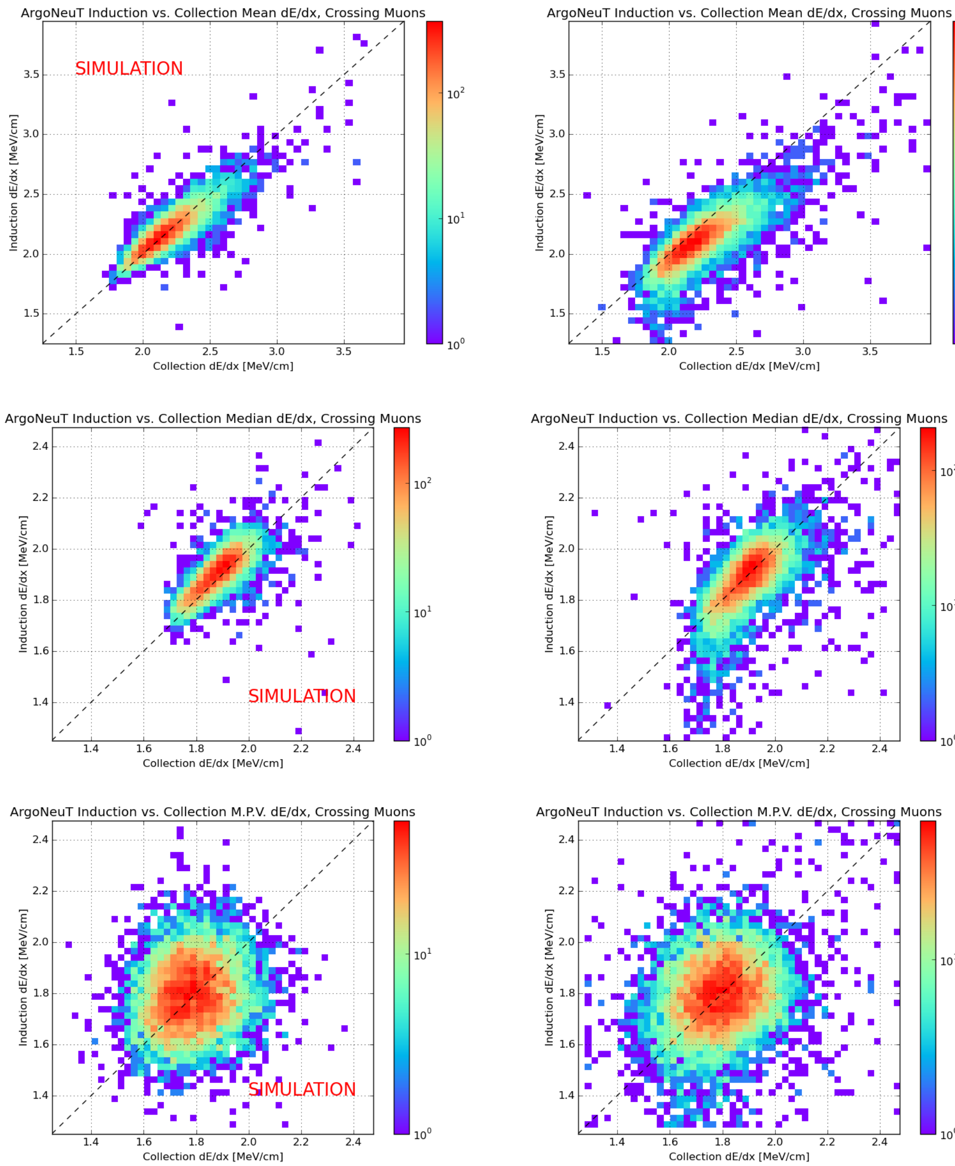

Figure 3.11: A comparison of the mean, median, and most probable value for crossing muons between the collection (x axis) and induction (y axis) planes. Simulation is shown on the left, data on the right. There is good agreement between collection and induction planes, as well as between simulation and data.

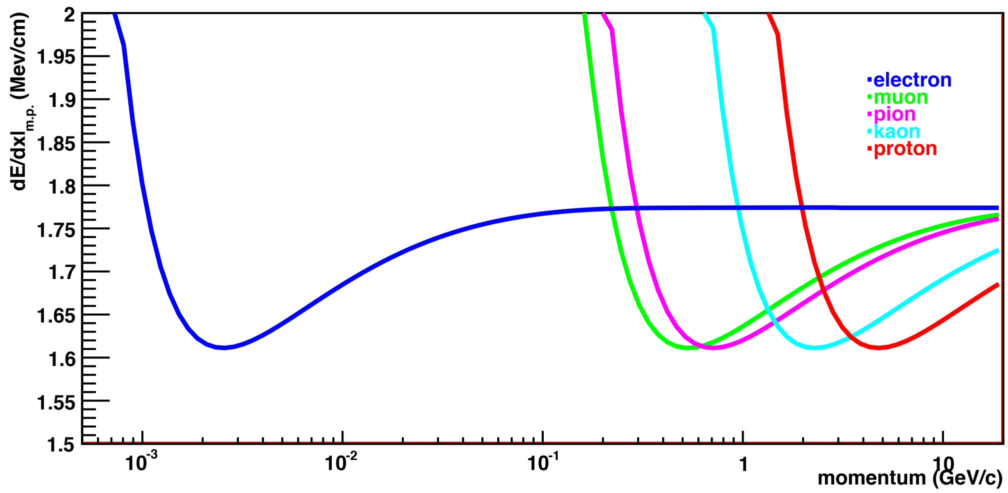

Figure 3.12: Most probable ionization per centimeter in argon for a variety of common particles.

3.4.6 MINOS

ArgoNeuT is fortunate in that it was located directly upstream of the MINOS near detector, which is a magnetized tracking detector [101]. This gives ArgoNeuT a distinct trait that no other LArTPC has had: muon sign selection for muons produced in ArgoNeuT that enter the MINOS near detector.

ArgoNeuT is only 90cm long at it's longest dimension, and since the NuMI beam has neutrino energies of 10+ GeV, it is extremely rare for muons produced in ArgoNeuT to stop within the detector. This enabled several precision measurements of muon neutrino cross sections on argon by looking for neutrinos that interact in ArgoNeuT, and tracking them through the MINOS near detector [91, 92].

For the analyses presented in this thesis, MINOS is not used as a muon spectrometer directly. Instead, since the target interaction is electron neutrinos, MINOS is able to provide rejection of muon neutrino events.

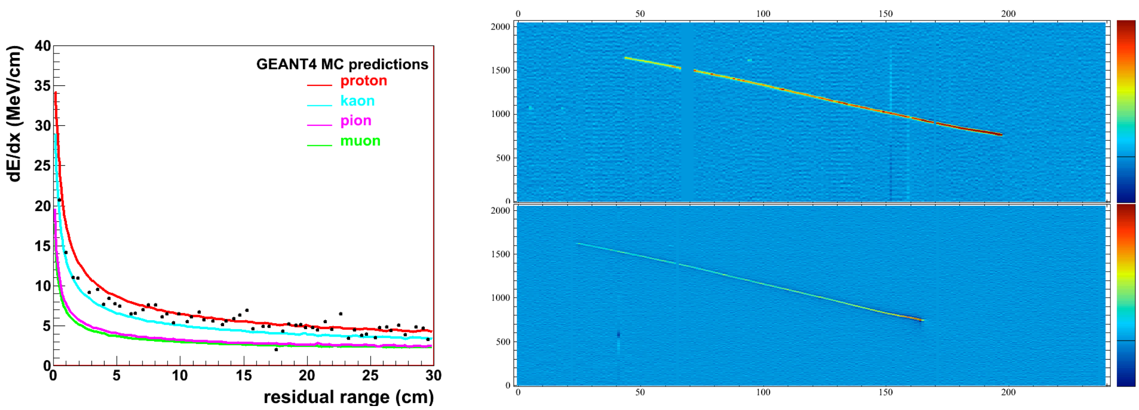

Figure 3.13: (Left) dE/dx versus residual range of various particles in liquid Argon. The values of dE/dx vs. Residual range for a particle observed in the detector can be used to identify the particle's type. (Right) A stopping particle in the ArgoNeuT detector. The values of this particle's dE/dx versus residual range (black points on left) identify it as a proton.

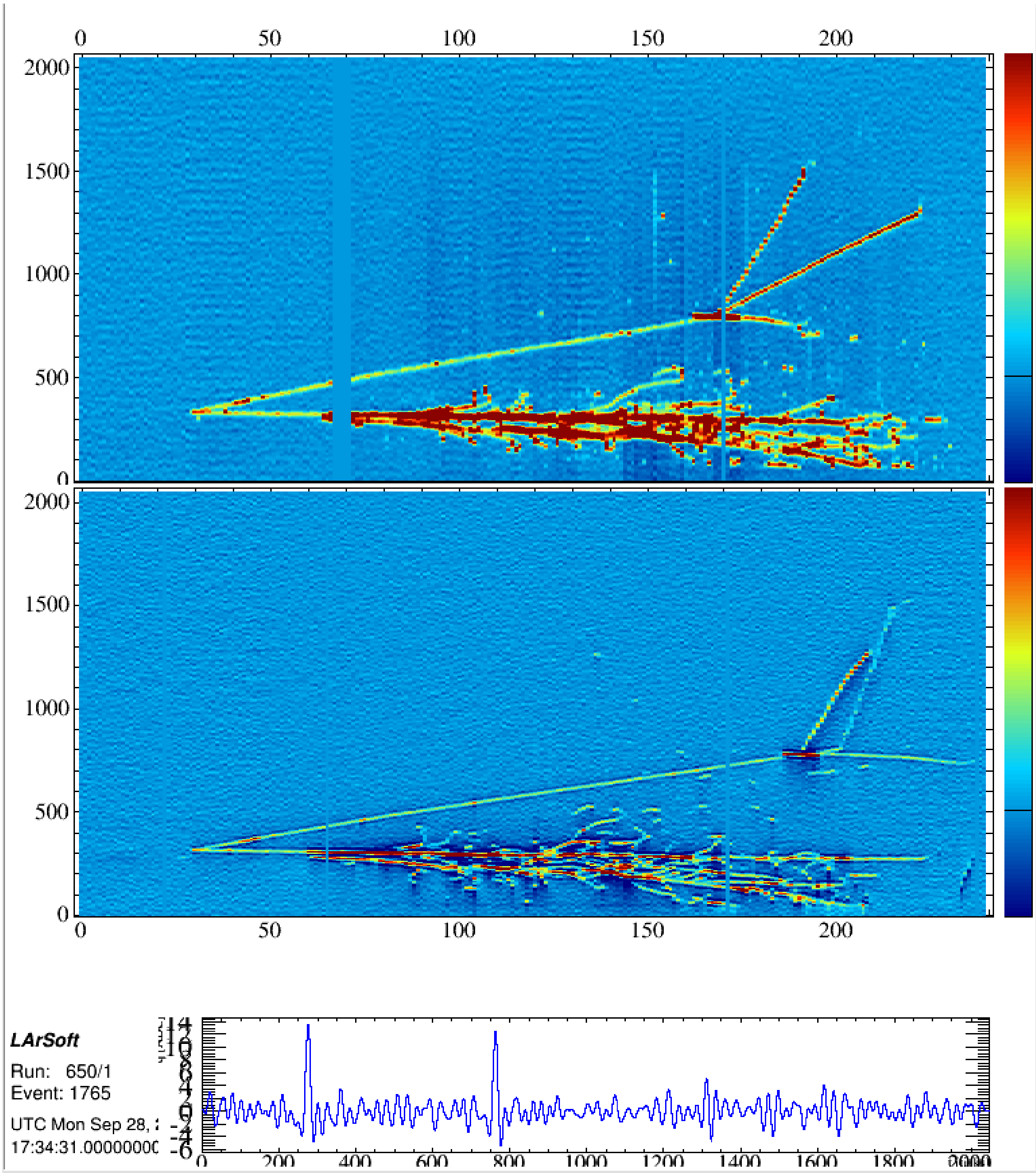

Figure 3.14: An ArgoNeuT event with a strong pion reinteraction. The pion track, starting from the bottom left and moving towards the top right, reinteracts with an argon nucleus through a hadronic interaction. The resulting topology of many particles from the secondary interaction easily distinguishes this track as a pion and not a muon.

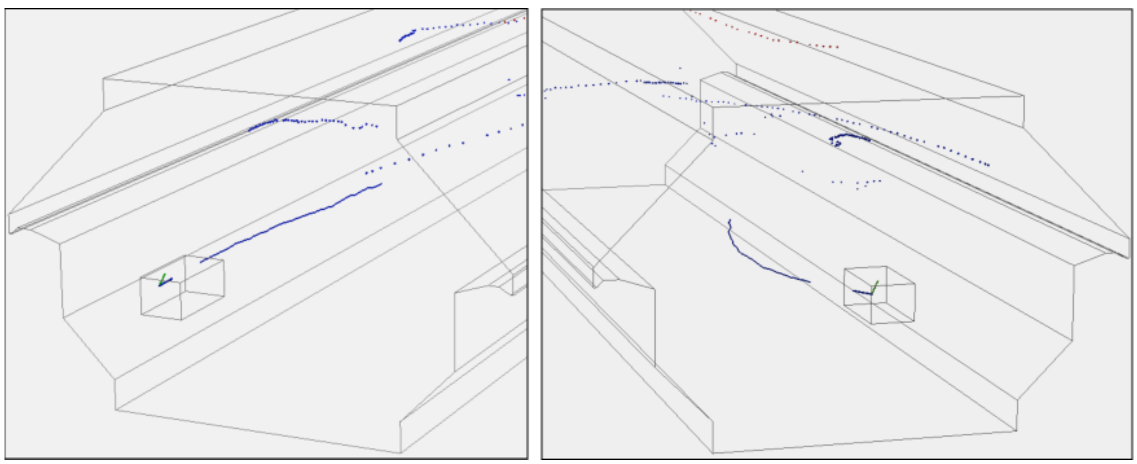

Figure 3.15: An event display depicting the ArgoNeuT experiment and the MINOS near detector. ArgoNeuT is the small box in the foreground. The tracks represent TPC data of ν_μ CC interactions that were successfully tracked and matched into the MINOS near detector. Figure from [90].

3.5 Current and Future LAr-TPCs

ArgoNeuT, the main subject of this chapter, was the first LArTPC in a neutrino beam in the U.S. and the start of the U.S. LAr-TPC neutrino program. Before ArgoNeuT even collected data, however, another LAr-TPC was already proposed: MicroBooNE. Since then, LAr-TPCs have become the detector of choice for neutrino physics in the GeV energy range. This section describes some of the important future TPCs in the US neutrino program.

3.5.1 MicroBooNE

MicroBooNE [102] is the successor to MiniBooNE [103] (See Section 4.1.3), and is designed to confirm or rule out the MiniBooNE "Low Energy Excess," described further in Chapter 4. MicroBooNE is large TPC, 235 $(w)\times$ 250 $(h)\times$ 10.95 (l) m^3, or about 87 tons of Liquid Argon - see Figure 3.16. The most notable differences, other than size, between ArgoNeuT and MicroBooNE are the third instrumented wire plane and the PMT system for light collection. Additionally, the wire spacing in MicroBooNE is 3 mm, decreased from 4 mm in ArgoNeuT.

MicroBooNE's main physics goal, the resolution of the Low Energy Excess, is in addition to a host of other physics and R&D tasks. On the physics side, MicroBooNE will provide exceptional data for studying neutrino interactions, particularly in understanding nuclear physic effects in neutrino interactions. MicroBooNE has the finest 3D resolution of any calorimetric neutrino detector to date, allowing it to measure the outgoing hadrons (protons, pions, neutrons, kaons, etc.) from a neutrino interaction. An image of the MicroBooNE collection plane, Figure 3.17, showing a ν_μ candidate event with a proton and π^0, showcases MicroBooNE's precision imaging. MicroBooNE expects high statistics in many interesting neutrino cross section channels, as shown in Table 3.1. The cross section measurements of MicroBooNE (and SBND and ICARUS) will be a major

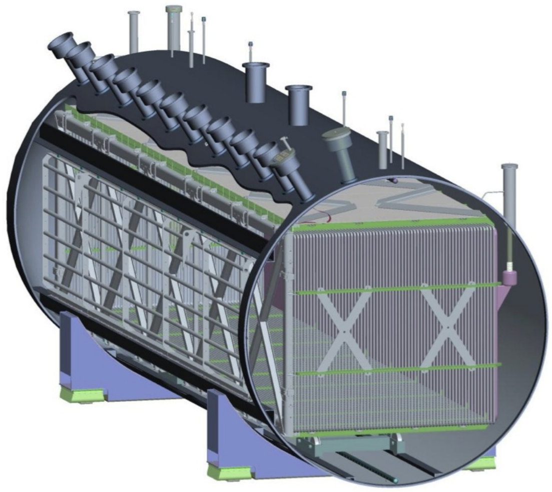

Figure 3.16: A schematic image of the MicroBooNE detector as it was designed. The beam enters from the bottom right side of the detector, along the longest axis. The high voltage cathode is on the right, back of the detector while the sense wires are on the exposed left side where the cryostat has been cut away.

legacy of the Fermilab LAr-TPCs especially in the DUNE [74] era.

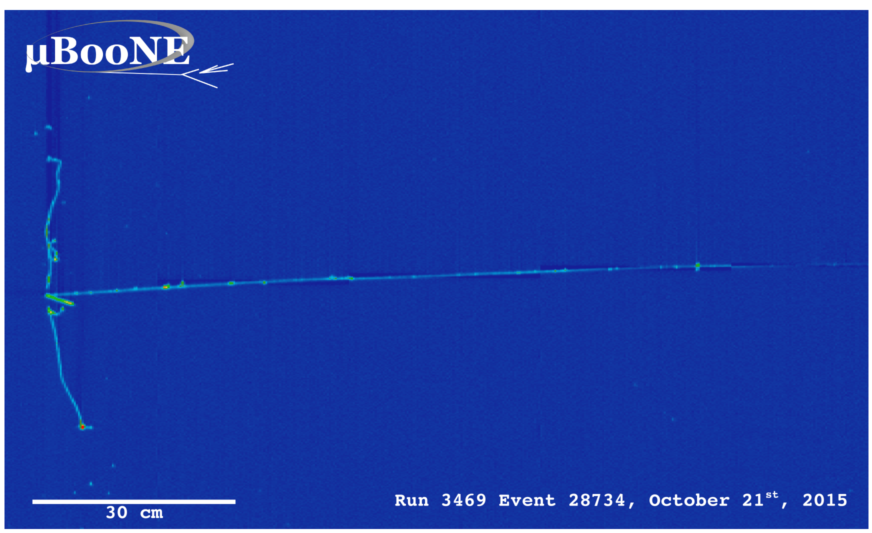

Figure 3.17

MicroBooNE also introduces a number of important R&D acheivements to the field of LAr-TPCs. It is the first large scale LAr-TPC to acheive high purity without evacuating the cryostat. Instead, the TPC used a purge of high purity argon gas to push impurities out of the cryostat before colling the cryostat and filling with liquid argon. In this way, critical

Process		**No. Events**
	ν_μ Events by Topology	
CC Inclusive		122,100
CC 0 π	ν_μ N $\rightarrow \mu$ + Np	78,500
	$\cdot\ \nu_\mu$ N $\rightarrow \mu$ + 0p	16,500
	$\cdot\ \nu_\mu$ N $\rightarrow \mu$ + 1p	44,200
	$\cdot\ \nu_\mu$ N $\rightarrow \mu$ + 2p	8,300
	$\cdot\ \nu_\mu$ N $\rightarrow \mu + \geq$ 3p	9,500
CC 1 $\pi^\pm$	ν_μ N $\rightarrow \mu$ + nucleons + $1\pi^\pm$	30,300
CC $\geq 2\ \pi^\pm$	ν_μ N $\rightarrow \mu$ + nucleons + $\geq 2\ \pi^\pm$	2,700
CC $\geq 1\ \pi^0$	ν_μ N $\rightarrow \mu$ + nucleons + $\geq 1\ \pi^0$	13,400
NC Inclusive		45,900
NC 0 π	ν_μ N $\rightarrow \mu$ + nucleons	29,900
NC 1 $\pi^\pm$	ν_μ N $\rightarrow \mu$ + nucleons + $1\pi^\pm$	6,900
NC $\geq 2\ \pi^\pm$	ν_μ N $\rightarrow \mu$ + nucleons + $\geq 2\ \pi^\pm$	900
NC $\geq 1\ \pi^0$	ν_μ N $\rightarrow \mu$ + nucleons + $\geq 1\ \pi^0$	9,200
	ν_e Events	
CC Inclusive		820
NC Inclusive		290

Table 3.1: Estimated event rates using GENIE (v2.8) in a 6.6e20 POT exposure of MicroBooNE, located 470m from the neutrino source, the Booster Neutrino Beam. In enumerating proton multiplicity, there is a kinetic energy threshold on protons of 20 MeV. The 0π topologies include any number of neutrons in the event. This study uses a 17cm fiducial volume cut in MicroBooNE, which gives a fiducial volume of 61t.

impurities were removed from the detector - see Figure 3.18. Additionally, MicroBooNE employs cold readout electronics immersed in the liquid argon. As seen in Figure 3.19, the average noise level of the readout wires decreased dramatically during the cooldown of the MicroBooNE cryostat.

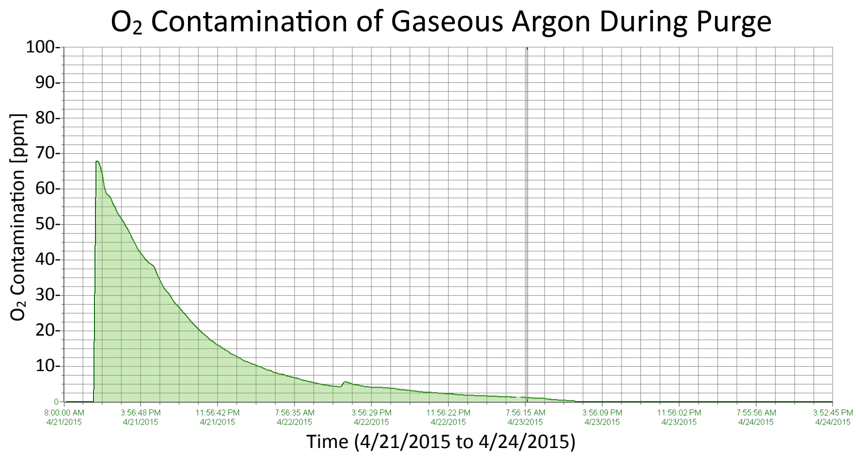

Figure 3.18: The oxygen contamination of the gaseous argon while purging air. The sensor for this oxygen concentration was turned on after 10:00 AM April 21, 2015, and it reached its sensitivity limit during the evening of April 23, 2015. [104]

Another significant improvement that MicroBooNE brings that ArgoNeuT did not have is the addition of a light collection system. A light collection system is essential for detectors like MicroBooNE running on the surface and not deep underground. The MicroBooNE light collection is composed of 8 inch Photo-Multiplier Tubes (PMTs) arrayed behind the wire planes. Argon scintillates at a vacuum ultraviolet wavelength (to which liquid argon is transparent), but the PMTs detect visible light. So, each PMT has a wavelength shifting plate to convert the vacuum ultra violet to visible light detectable by the PMTs.

On the surface, MicroBooNE is exposed to a high flux of cosmic rays, as many as 10 cosmic ray interactions in the detector each readout window of 4.8 ms. On the other hand, the detector is exposed to the neutrino beam for just several μs. Though the wire

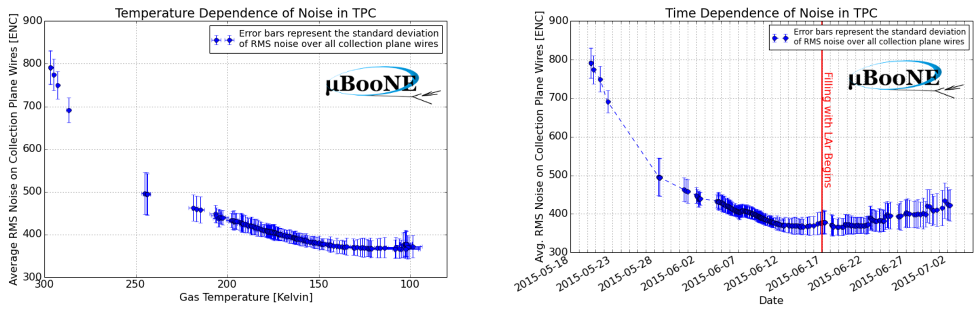

Figure 3.19: Noise measured on collection plane wires as a function of temperature (left) and time (right). Data points represent the average RMS, and error-bars show the standard deviation of these distributions. Error bars are meant to show how the change in temperature affects noise levels compared to the intrinsic variability of noise in the detector due to channel-to-channel gain variations. [105]

information can not be used to identify precisely when an interaction occurred in the TPC, the PMT information detects flashes of light with each particle interaction and can localize interactions in a much tighter region of time. This provides two advantages: first, if the time of an interaction is known (particularly cosmic interactions), the corrections that must be applied as a function of drift distance (such as lifetime corrections) can be accurately applied. Second, and more important for a successful operation of the detector, the PMT system provides a triggering system for the beam interactions, as shown in Figure 3.20. A clear excess of PMT flashes coincident with the expect neutrino beam, for both BNB and NuMI beams, can be seen. By only saving events to disk when there is a PMT flash in this region of time, MicroBooNE is able to dramatically reduce it's consumption of network bandwidth and disk storage.

MicroBooNE began taking neutrino data in the fall of 2015, and collected approximately 3.5E20 POT (about half of its data set) by the fall of 2016. In the near future, MicroBooNE will determine the origin of MiniBooNE's low energy excess. MicroBooNE will lead the Fermilab Short Baseline Program forward as the first running LAr-TPC on the Booster Neutrino Beam, which is an exciting step forward in the U.S. LAr-TPC program.

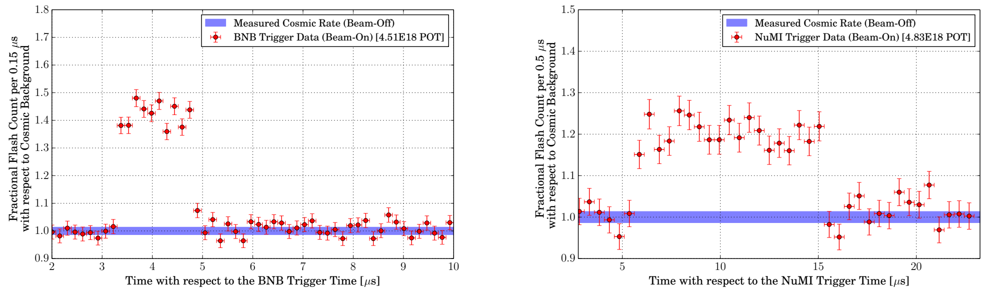

Figure 3.20: The measured distribution of flash times (requiring flashes greater than 50PE) with respect to the trigger time for BNB-triggered events (left) and NuMI-triggered events (right), shown as a ratio to the expected cosmic rate from off-beam data. The blue band denoting the cosmic rate was centered at one, with a width corresponding to the measured uncertainty in the cosmic rate. A clear excess can be seen due to neutrinos between 3 and 5 μs (for BNB) 6 and 15 μs (for NuMI) after the trigger. This is where the neutrinos were expected based on the Resistive Wall Monitor signal arrival time. A total of 1.92E6 BNB (left) and 3.67E5 NuMI (right) triggered events (unbiased trigger) were used to produce this plot. [106]

3.5.2 Future LArTPCs

As mentioned above, MicroBooNE is the newest LAr-TPC to the Fermilab Short Baseline Program, but there are two other LAr-TPCs planned to begin operation within several years. In this brief section, I will give a few selected details of these other two detectors as they are both critical components of the SBN program and essential to resolving short baseline neutrino anamolies (see Chapter 4).

SBND

Along the Booster Neutrino Beam, SBND will be the LAr-TPC closest to the neutrino source. It is currently under design and construction, with final assembly taking place in 2017 and 2018. Due to the proximity of SBND to the BNB target and the high power of the BNB, SBND will have the highest statistics measurements of neutrino interactions of any LAr-TPC to date. With over 1 million events per year, SBND records statistics equivalent to the MicroBooNE data set in just one month (and it matches the statistics of ArgoNeuT in just one day!). With this expected event rate, SBND can probe rare neutrino interactions with high statistics. The high event rate also allows precision measurements of final state topologies of neutrino interactions, which in turn is essential for tuning neutrino interaction models for DUNE.

Like MicroBooNE, SBND will feature a light collection system to trigger neutrino events and accurately determine cosmic timing. Unlike MicroBooNE, SBND is a dual drift TPC with the high voltage cathode in the middle of the TPC, and two sets of read out wires on each side - see Figure 3.21. Like MicroBooNE, SBND is driving forward the U.S. LAr-TPC program with important R&D tasks, including the manufacture of Cathode Plane Assemblies and Anode Plane Assemblies.

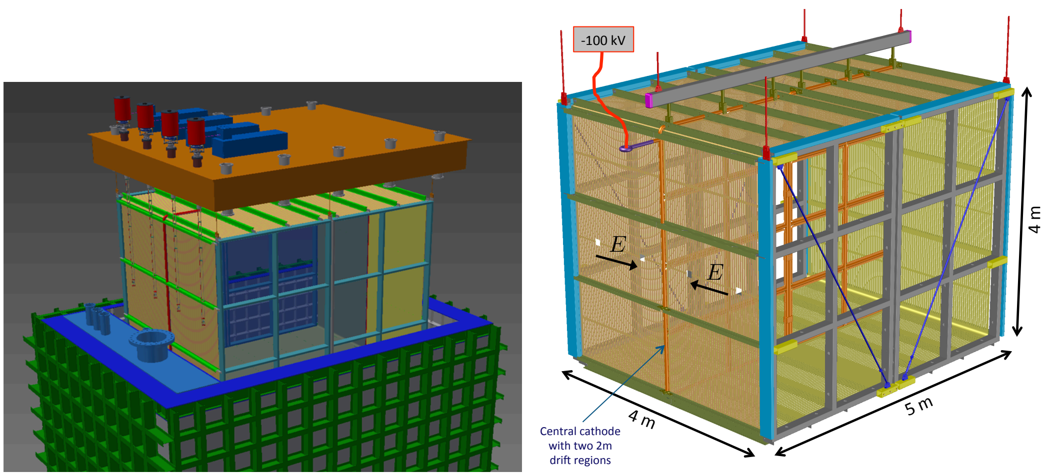

Figure 3.21: The SBND TPC (left) and cryostat design (right).

ICARUS-T600

ICARUS is an international LAr-TPC that was run in Italy, and the first large scale LAr-TPC in a neutrino beam. The detector, known as T600, is approximately 476 tons of active argon divided into two modules (known as T300 each). The two modules were deployed together at Gran Sasso lab in Italy, underground, where they were exposed to CERN's CNGS neutrino beam. ICARUS has been a pioneer of LAr-TPC technology.

After the CNGS beam was decommissioned, it was decided to transport the ICARUS detector from Italy to Fermilab for use as the third detector in the SBN Program. ICARUS is significantly more massive than both MicroBooNE and SBND, and so it offers the chance to record oscillation spectra from anomalous neutrino oscillations at a different L/E than MicroBooNE, with high statistics. Currently, ICARUS is at CERN where it is being refurbished and upgraded, before it is shipped to Fermilab for installation.

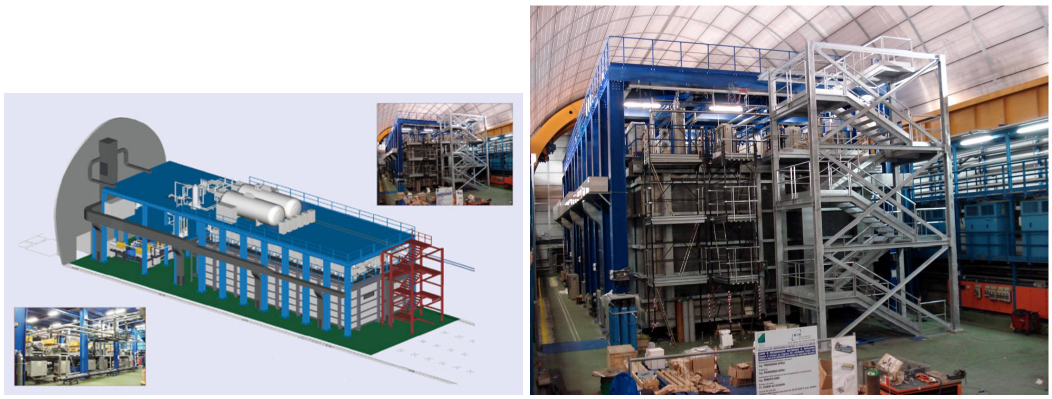

Figure 3.22: The design of the ICARUS T600 detector (left) and the realization of the detector underground at Gran Sasso lab in Italy (right).

Chapter 4

Short Baseline Neutrino Program

This chapter will describe the Short Baseline Neutrino Program, and the anomalies it is seeking to resolve.

4.1 Motivation and Goals

Over the past two decades, there have been a number of anomalous results from short baseline experiments from a variety of neutrino experiments. Individually, each experiment lacks the significance to be convincingly claim discovery of beyond the standard model physics. Taken together, however, these data can be interpreted as an oscillation on a mass splitting scale that is inconsistent with the three neutrino mixing model. This section will briefly summarize the current anomalies in this area of neutrino oscillations, known as Short Baseline oscillation physics.

A more thorough analysis of the global, experimental picture of neutrino oscillations is given by oscillation analyses such as Kopp et. al [107], Giunti et. al [108]. Though there is tension in the experimental evidence, there is indication that anomalous neutrino oscillation is occurring at short baselines.

4.1.1 LSND

In 1995, the Liquid Scintillator Neutrino Detector at Los Alamos National Laboratory published the results of it's first search for $\bar{\nu}_\mu$ to $\bar{\nu}_e$ oscillations [109]. The detector was a liquid scintillator detector making observations of electron anti neutrinos through the inverse beta decay reaction on carbon. The origin of the neutrinos was a decay at rest pion source, producing neutrinos in the range of 20 to 50 MeV. In the inverse beta decay reaction signature is a prompt positron emission, followed by a 2.2 MeV gamma from neutron capture. LSND observed $89.7 \pm 22.4 \pm 6.0$ $\bar{\nu}_e$ candidate events above background over five years of data taking, corresponding to a significance of 3.8 σ.

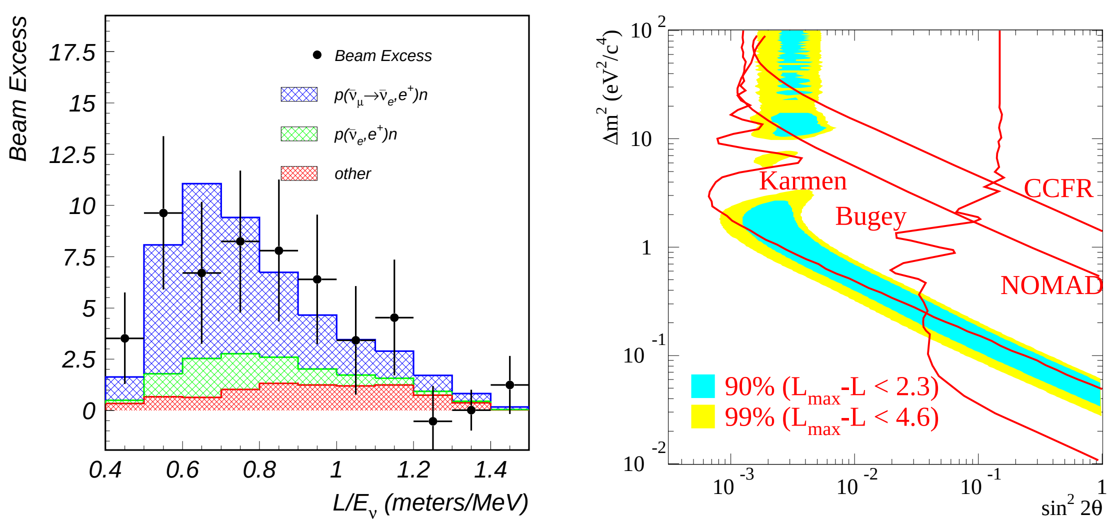

Figure 4.1: (Left) Excess of candidate $\bar{\nu}_e$ events observed by LSND, plotted as a function of L/E of the reconstructed neutrino. (Right) Allowed region of oscillation parameters when fit against a 2 neutrino mixing model.

As seen in Figure 4.1, the LSND excess is inconsistent with the three neutrino oscillation paradigm. Instead, it hints at oscillations at L/E of ~ 0.5 and a mass splitting of ~ 1 eV^2. For comparison, the solar and atmospheric mass splittings are in the ranges of 7×10^{-5} eV ^{2} and 2×10^{-2} eV ^{2}, respectively.

4.1.2 Reactor Experiments

Many experiments have measured the flux of neutrinos from nuclear reactors over many years. However, a recent reevaluation [110] [111] of the expected neutrino flux from reactors has led to an observed deficit in historical measurements, as seen in Figure 4.2 [112]. This deficit, at the level of 6 to 7%, is consistent with an oscillation of reaction $\bar{\nu}_e$ into an unobserved sterile state.

Some concern over the so called Reactor Deficit has been raised over the fact that before the recalculation was completed, all experiments were in agreement with the existing theoretical prediction. However, experimental results from the Daya Bay collaboration [113], done in a blind analysis, support the experimental evidence of the reactor neutrino deficit (See Figure 4.3).

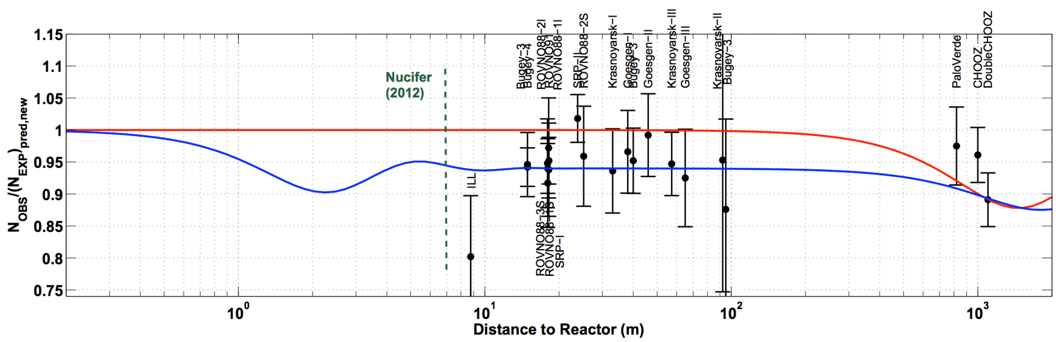

Figure 4.2: Measurements of the reactor neutrino flux indicate a deficit when compared with theoretical predictions. It's plausible that the deficit is evidence of anomalous neutrino oscillations.

4.1.3 MiniBooNE

Most recently, the MiniBooNE collaboration published evidence for an excess of electron neutrino candidate events in both neutrino and anti neutrino mode at Fermilab's Booster Neutrino Beam [114]. Their results, shown in Figure 4.5, clearly indicate an excess of candidate events. The significance of the results is 3.4 σ for Neutrino Mode, 2.8 σ in Anti-Neutrino Mode.

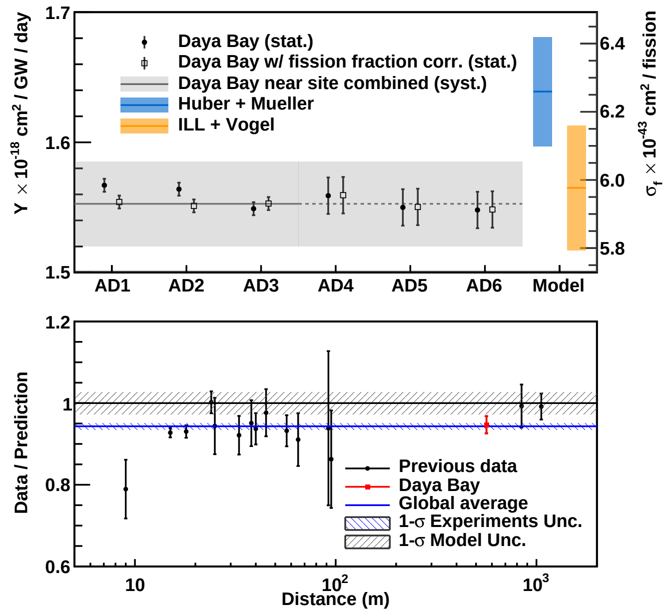

Figure 4.3: The Daya Bay experiment performed a blind measurement of the reactor flux and their location and found excellent agreement with previous experimental data. This was performed after the flux recalculations.

MiniBooNE is a Cherenkov type detector, meaning that it distinguishes particles based upon their Cherenkov signature observed by PMTs at the outer surface of the detector. Since electrons and photons both produce similar electromagnetic cascades, MiniBooNE is unable to distinguish between electron and photon events. For the electron neutrino analysis in Figure 4.5, this implies that the excess can not be attributed as electron neutrinos without further investigation, and therefore isn't conclusively inconsistent with the standard three neutrino oscillation model.

When taken with consideration into consideration with other results such as LSND (at the same L/E as MiniBooNE), and the reactor and source anomalies, there is intriguing evidence of physics beyond the Standard Model in the neutrino sector.

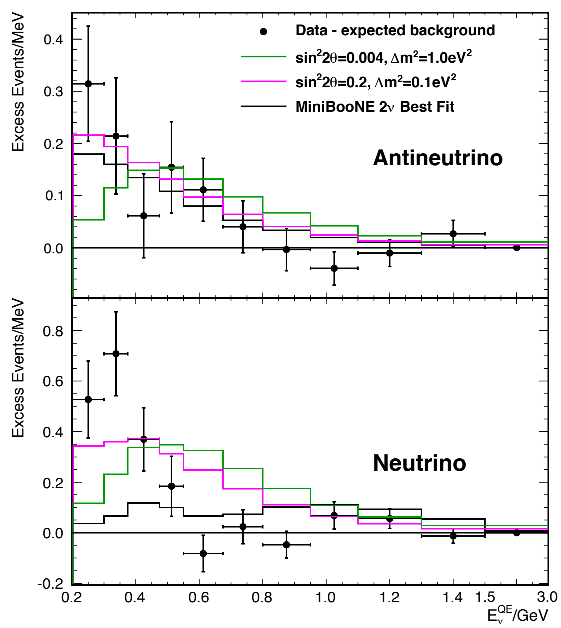

Figure 4.4: The MiniBooNE beam excess.

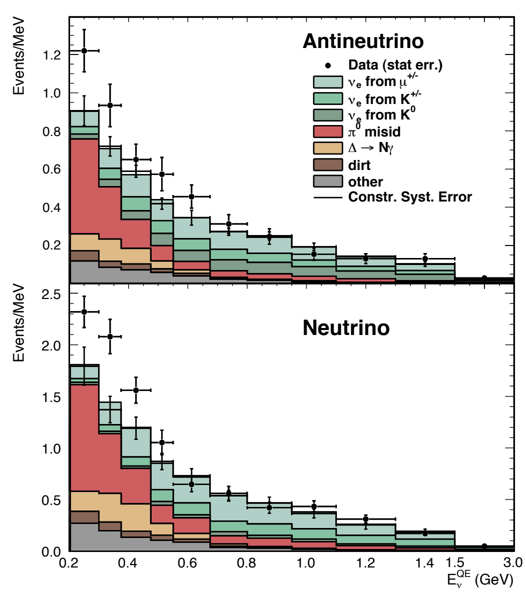

Figure 4.5: The MiniBooNE electron neutrino candidate sample.

4.1.4 Global Fits

With many hints at beyond the standard model neutrino oscillations, analyses have been performed to bring together the various hints (and null results) in an attempt to constrain allowed phase space in sterile neutrino oscillations. In particular, a viable explanation of the anomalies using sterile neutrinos must be in agreement across multiple signatures of oscillations, for a 3+1 model. Ignoring CP violating terms (which are not observable in short baseline experiments), the mixing matrix for a 3+1 model is given as:

$$\mathbf{U} = \begin{pmatrix} U_{e1} & U_{e2} & U_{e3} & U_{e4} \\ U_{\mu 1} & U_{\mu 2} & U_{\mu 3} & U_{\mu 4} \\ U_{\tau 1} & U_{\tau 2} & U_{\tau 3} & U_{\tau 4} \\ U_{s1} & U_{s2} & U_{s3} & U_{s4} \end{pmatrix}$$

1. *Electron Neutrino Disappearance:* An electron neutrino can oscillation into an unobservable, sterile neutrino state with amplitude given as

$$P(\nu_e \to \nu_{\not{e}}) \approx sin^2(2\theta_{ee}) \times sin(1.27\frac{\Delta m^2 L}{E}\frac{[eV^2][m]}{[MeV]})), \tag{4.1}$$

$$sin^2(2\theta_{ee}) \equiv 4|U_{e4}|^2(1-|U_{e4}|^2) \approx 4|U_{e4}|^2. \tag{4.2}$$

This is the oscillation regime that governs, for example, the reactor neutrino anomaly.

2. *Muon Neutrino Disappearance:* In a nearly identical fashion as above, a muon type neutrino can oscillate into a sterile stage with amplitude

$$P(\nu_\mu \to \nu_{\not{\mu}}) = sin^2(2\theta_{\mu\mu}) \times sin(1.27\frac{\Delta m^2 L}{E}\frac{[eV^2][m]}{[MeV]})), \tag{4.3}$$

$$sin^2(2\theta_{\mu\mu}) \equiv 4|U_{\mu 4}|^2(1-|U_{\mu 4}|^2) \approx 4|U_{\mu 4}|^2. \tag{4.4}$$

Intriguingly, there has been no observed signal of muon neutrino disappearance consistent with the same anomalies that hint towards sterile neutrino oscillations, despite searches by MINOS [22], MiniBooNE +SciBooNE [115], and IceCube [21].

3. *Electron (and Anti-Electron) Appearance:* Given that a sterile neutrino can have mixing parameter that connect to both electron and muon type neutrinos, it is possible to have an oscillation of muon neutrinos into electron neutrinos.

$$P(\nu_\mu \to \nu_e) = sin^2(2\theta_{\mu e}) \times sin(1.27\frac{\Delta m^2 L}{E}\frac{[eV^2][m]}{[MeV]})), \tag{4.5}$$

$$sin^2(2\theta_{\mu e}) \equiv 4|U_{\mu 4}|^2|U_{e4}|^2 \approx \frac{1}{4}sin^2(2\theta_{ee})sin^2(2\theta_{\mu\mu}). \tag{4.6}$$

As seen in [107, 116], limits on the oscillation amplitude from electron neutrino and muon neutrino disappearance can place upper bounds on the amplitude of muon to electron neutrino oscillation.

Taken together, the global data can be combined as in [107, 116]. In the best fit by Kopp et. al, there is no strongly allowed region though the tension between signals and null results is high. In the best fit by Giunti et. al, there is an allowed region though the MiniBooNE anomaly is not included in this fit (for the inconsistencies mentioned above).

4.2 FermiLab's Short Baseline Neutrino Program

With all of the above anomalies and hints of beyond the standard model, it is essential to address the sterile neutrino question and resolve the MiniBooNE anomaly. To address these hints, Fermilab is pursuing a program of short baseline neutrino experiments along it's Booster Neutrino Beam. The first experiment, MicroBooNE, started operations in 2015 and is designed to definitively address the MiniBooNE anomaly. Subsequently, two other detectors will join MicroBooNE along the Booster Beam at 100m and 660m. An overview of the three LAr-TPCs involved in Fermilab's Short Baseline Program is given in Sections 3.5.1 and 3.5.2. The location of the three detectors can be seen in Figure 4.6.

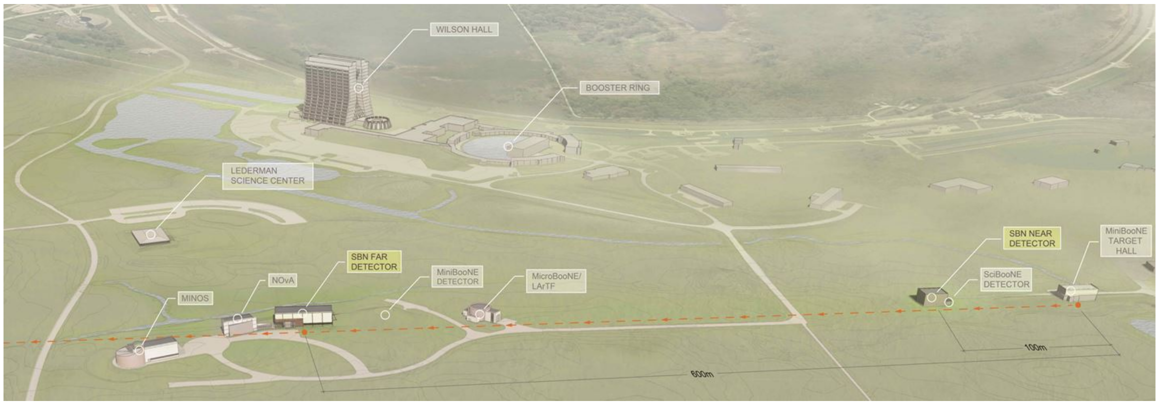

Figure 4.6: An aerial view of the SBN program. The three detectors are highlighted in yellow, and (from right to left, along the path of the beam) are SBND, MicroBooNE, and ICARUS-T600

4.3 Physics Program

The Short Baseline Neutrino program has an aggressive agenda to probe anomalous oscillation signals, and to follow up on MicroBooNE's Low Energy Excess analysis. It's worth noting that ν_e appearance is not the only physics analysis that will be performed by the SBN Program. This thesis will focus on ν_e appearance, however to resolve questions of sterile neutrinos the SBN program will also have to observe:

- ν_μ **Disapperance** As mentioned above, the channels of ν_e appearance and ν_μ disappearance are intricately connected in models of sterile neutrino oscillations. So, for any measurement of ν_e appearance at the SBN Program to be interpreted in a 3+1 model of oscillations, it should be accompanied by an amount of ν_μ disappearance consistent with the level of ν_e appearance. Much more about ν_μ disappearance is available in the SBN Program Proposal [19]

- **Neutral Current Disappearance (Active flavor Disapperance)** Just as the ν_e and ν_μ oscillation signals are connected if a sterile neutrino is present, the total active flavor content of the beam ($\nu_e + \nu_\mu + \nu_\tau$) should be modulated by the presence of a sterile neutrino in a consistent way. LAr-TPC technology allows measurement of the total neutral current interaction rate using channels such as Neutral Current π^0

production.

Also of interest is the suite of cross section measurements that the SBN Program can perform, particularly with the SBND experiment (the near detector). In the event that MicroBooNE observes the MiniBooNE anomaly to be an unexpected beam background or cross section, SBND can probe this result with nearly two orders of magnitude faster collection of events than MicroBooNE.

4.4 Simulation and Monte Carlo Predictions of Event rates

For the calculation and study of the physics sensitivity of the Short Baseline Program, a Monte Carlo Simulation predicts the event rate at each detector in the beamline. The procedure of the simulation is:

1. **Booster Beam Monte Carlo** The first stage in the simulation is the Monte Carlo simulation of the Booster Neutrino Beam production. This is a geant4 based simulation that follows 8 GeV protons through interactions on the BNB beryllium target. The hadrons produced in the interaction are focus by the horn and decay, in flight, to neutrinos, which are then propagated to a window in front of a detector. It is at this stage of the simulation that we include a series of reweighting variables for each neutrino to estimate the systematic uncertainty on the flux at each detector, as well as the correlations between detectors (additional information in Section 5.3).

2. **GENIE Neutrino Interactions** The output of the beam Monte Carlo is a file of neutrinos at the detector containing information about the flavor, momentum, and position, as well as the parentage from the beam source, for each neutrino. The interactions of these neutrinos are simulated with the genie software which outputs a series of particles exiting the argon nucleus [117].

3. **GEANT4 Simulation of Particles** The particles which exit the argon nucleus, as generated by genie, are then propagated through the liquid argon using a GEANT [77] simulation built in to the LArSoft framework [98]. In particular this helps estimate the containment of electromagnetic showers, interaction location of photons from π^0 production and Δ resonances, as well as containment of minimally ionizing particles such as muons and charged pions.

4. **Monte Carlo Truth Based Information** After the geant simulation of the neutrino interaction we extract the event information using the Monte Carlo truth information. Estimated reconstruction efficiencies and energy resolutions are applied at this stage, as well as simulated event selections based on expected detector performance. See Section 4.4.2 for more detail.

4.4.1 Background Classification

For the study of the Short Baseline Neutrino Program's sensitivity to anomalous appearance of electron neutrinos, it is essential to have a comprehensive estimate of the various backgrounds with realistic distributions based on expected reconstruction ability. Primarily, the ν_e appearance background consists of 3 broad categories: intrinsic ν_e's from the beam, mis-identified electromagnetic showers produced by the beam (primarily from ν_μ), and cosmic induced backgrounds coincidental with the beam spill.

1. **Intrinsic ν_e** - the Booster Beam, while primarily composed of muon neutrinos, has contamination of electron neutrinos that account for about 0.5% of the beam. While this is a small contamination, it is the same order of magnitude as the best fit oscillation parameters for possible sterile neutrino hints. This means that, compared to any possible signal, the intrinsic electron neutrinos in the beam are a large background and must be carefully quantified. An 80% reconstruction efficiency is applied to these events, and an electromagnetic shower energy of 200MeV is set as a threshold

for event selection. This is to ensure good selection and reconstruction in the data, and has a moderate impact at lower energies on the efficiency (30% loss in the 200 to 350 MeV bin) with small impacts (5%) at higher energies.

2. **Neutral Current Photon Misidentification** - The photons produced in the detector by neutral current processes can produce an electromagnetic shower similar to electron neutrinos. An example of a reaction that produces high energy photons is an interaction with neutral pions in the final state, as well as radiative decays from nucleon resonances. It's expected that, without cuts, these backgrounds can be large and in the same energy region as a signal search. However, analysis cuts can greatly reduce this background.

    (a) *Two photon cut:* In an event with candidate electromagnetic showers, the presence of multiple showers indicates there could be neutral pion production in the neutrino interaction. See, for example, Figure 4.7 for an ArgoNeuT event with multiple showers. For this analysis, if a second found is found with energy greater than 100 MeV, the event is rejected from the electron neutrino sample. The energy cut, 100 MeV, is lower than the threshold for candidate electron showers because the second photon does not need accurate reconstruction, it just needs to be identified.

    (b) *Photon Conversion Gap:* In events where the neutrino interaction produces high energy photons, it can at times also product hadronic activity at the vertex. If more than 50 MeV of energy is observed at the vertex, and a gap between the electromagnetic shower and the vertex is detected with more than 3 centimeters (in MicroBooNE, this is up to 30 wires), the event is rejected.

    (c) *dE/dx Cut:* In this study, for events passing the previous two cuts, and 94% rejection was applied. This accounts for the expected resolution, in the SBN detectors, of the calorimetric based cut on the ionization of the first few centimeters of a shower. For more about the power of the dE/dx cut in data, see Section 6.6

3. **Neutrino Electron Scattering** - neutrinos can scatter off both the nucleus and the orbiting electrons in an atom. An interaction off an electron ejects the electron at high energy. Experimentally, the signature of this interaction is a very forward going electron and nothing else in the event, which mimics a ν_e charged current interaction. Fortunately, these events have a very low interaction rate compared to scattering off of a nucleus and are a secondary background. The forward angle and relatively high energy also make them a removable background.

4. ν_μ **Charge Current Misidentification** - The last item considered as a possible background are misidentified charged current interactions from muon neutrinos. The rate at which this happens is poorly know and needs to be measured, but there are some scenarios that could lead to this occurring. For example, in an event near the boundary of the TPC where a π^0 is produced along with the primary muon, if the muon exits and one photon converts outside the TPC there will be one electromagnetic shower seen and the track of the muon will be impossible to tag as a muon or charged pion. Though somewhat contrived, this example only serves to illustrate that this background should be considered. Here, events are included from ν_μ CC interactions if there is a single photon in the detector and the primary muon exits with less than one meter in the detector.

5. **Cosmic Photons** - Cosmic induced photons in the TPC have the potential to be incorrectly tagged as electrons. This is a background that will be very tightly constrained from off-beam backgrounds, but estimates from simulation are included here.

6. **"Dirt" Events** - Neutrinos can interact with the material surrounding the active volume of the detector as well. Though this is not, strictly speak, "dirt", events where detector external neutrino interactions travel into the TPC and deposit energy can

cause a background to the ν_e appearance analysis. In particular, photon production external to the TPC can generate a high energy photon that travels into the TPC and doesn't ionize the argon until it has entered the TPC for some distance. This background will be constrained with both simulation and data, however, preliminary estimates are included. Additionally, strong cuts can be made with fiducial volumes.

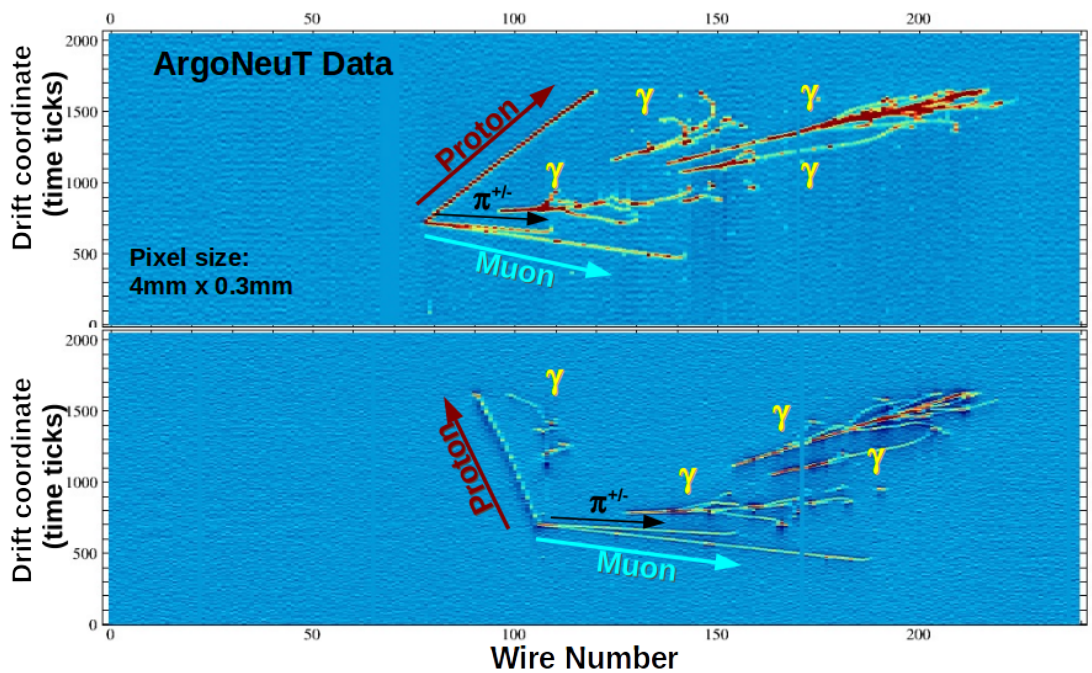

Figure 4.7: An ArgoNeuT event showing the production of neutral pions in electromagnetic showers.

4.4.2 Simulated Event Reconstruction and Analysis cuts

In order to perform the best estimate of the physics sensitivity of the SBN program, an estimate of reconstruction effects must be incorporated into the event rates. Additionally, some analysis cuts to reduce cosmic and "dirt" events are included.

The simplest cut is the fiducial volume cut applied in all three detectors. Events with a vertex found to be outside of the fiducial volume are rejected, and the volume is set as:

- **X:** The drift direction has a cut of 25cm from each edge, which reduces "dirt" backgrounds significantly.

- **Y:** The vertical direction also has a cut of 25cm from each edge, which reduces "dirt" backgrounds significantly.

- **Z:** The beam direction has an upstream cut of 30cm, to reject events that are entering the detector from the front. There is a downstream cut of 50cm to aid in detection of electromagnetic showers.

To simulate calorimetric energy reconstruction, the incoming neutrino energy in each Monte Carlo event is estimated by summing the energy of the lepton (or the γ the faking an electron) and all charged hadrons above observation thresholds present in the final state. The observation thresholds are defined by requiring that the kinetic energy of each hadron be sufficient that it cross at least 2 wires, and are guided by ArgoNeuT data. For protons, for example, the threshold is 20 MeV.

The event rate distributions, and the tables of event rates, are shown in Figure 4.8 and sidewaysTable 4.1.

4.5 Simulation of an Oscillation Signal

To predict a sensitivity of an experimental program, a model must be used to generate a sample of events that are signal events. In this case, as mentioned in Section 4.1.4, the two neutrino oscillation probability formula is used to transmute muon neutrinos into electron neutrinos. While the 3+1 model is not the only viable or interesting method to simulate a signal, it is the most straightforward to compare to other experiments.

To build a signal sample, a "fully oscillated" sample of Monte Carlo is generated where every ν_μ has been changed to a ν_e, and then the sample of ν_e's is propagated through the GENIE event generator and the rest of the simulation. Each electron neutrino, formerly

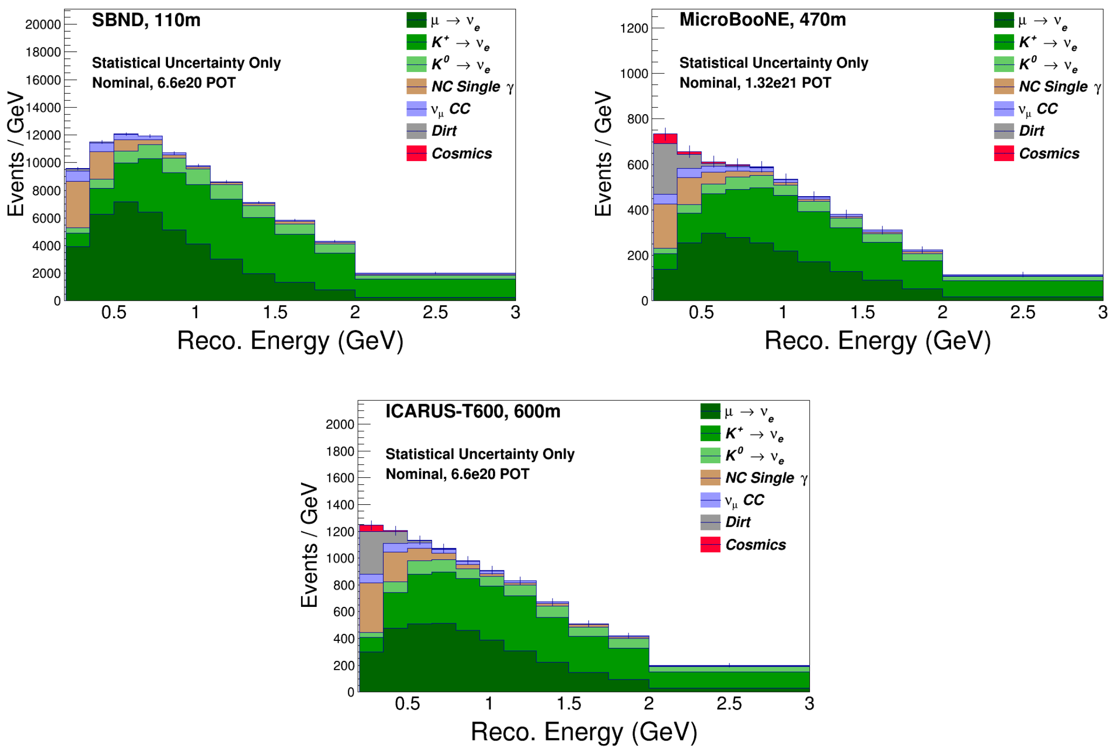

Figure 4.8: The predicted event rates for the SBN program in all three detectors, assuming 2.2e20 Protons on Target delivered each year. For this analysis, MicroBooNE is assumed to have 6 years of running (its original 3 + 3 with the SBN program)

.

muon neutrino, is "reconstructed" in the same manner as the electron neutrino candidates in the background sample, with identical cuts.

Later, a sensitivity curve will be shown as a function of $(\Delta^2_m, \sin^2 2\theta)$. This refers to physical parameters of neutrino oscillation, where Δm^2 is the mass splitting, squared, between known neutrinos and a supposed sterile state. $\mathrm{Sin}^2 2\theta$ represents the amplitude of the oscillation and is a combination of matrix elements from the neutrino mixing matrix above. For a fixed pair of $(\Delta^2_m, \sin^2 2\theta)$, each transmuted electron neutrino in the "fully oscillated" sample is scaled according to the formula

$$P(\nu_\mu \to \nu_e) = sin^2(2\theta_{\mu e}) \times sin(1.27\frac{\Delta m^2 L}{E}\frac{[eV^2][m]}{[MeV]})), \tag{4.7}$$

where L and E are known from the Monte Carlo as the distance the neutrino has traveled since the decay of it's parent particle, and the true energy of the neutrino. Because the neutrino beam is broad band, peaked near 1 GeV but with substantial flux down to several hundred MeV and out to 3 GeV, the oscillation probabilities at each detector are smeared and the predicted signal can cover a broad spectrum of neutrino energies (see Figure 4.9)

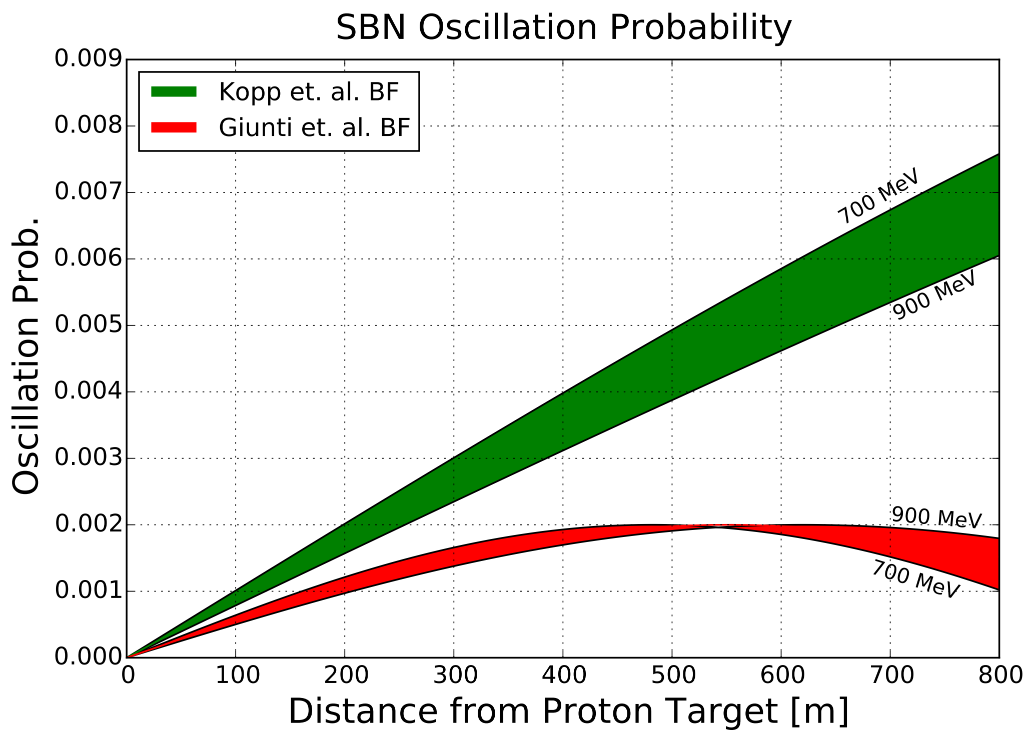

Figure 4.9: Oscillation Probability bands as a function of distance from the proton target for the SBN program. Shown are the bands for two of the global best fit results.

Table 4.1: Background Rates, broken out by analysis bin and origin, for the SBND experiment for 6.6e20 POT. The signal is from the Giunti *et al.* best fit point

Bins [GeV]	$\mu \to \nu_e$	$K^{\pm} \to \nu_e$	$K^0 \to \nu_e$	$\nu + e^-$	NC π^0	$\Delta \to N\gamma$	ν_μ CC	Dirt	Cosmic	Signal	Total
0.20-0.35	45	16	6	3	56	0	10	47	7	13	189
0.35-0.50	71	40	12	5	33	1	10	13	1	28	186
0.50-0.65	76	56	15	5	14	2	6	3	1	64	176
0.65-0.80	77	57	14	7	8	2	4	1	0	82	169
0.80-0.95	69	58	11	9	5	2	4	1	0	73	157
0.95-1.10	58	61	11	5	3	1	3	0	0	57	142
1.10-1.30	61	82	16	3	3	1	3	0	0	48	170
1.30-1.50	44	67	17	1	4	0	3	0	0	25	136
1.50-1.75	37	67	18	1	4	0	2	0	0	13	129
1.75-2.00	24	58	19	1	2	0	2	0	0	5	106
2.00-3.00	30	121	39	1	5	0	4	0	0	4	201
Total	593	684	177	39	137	8	50	65	10		

Table 4.2: Background Rates, broken out by analysis bin and origin, for the MicroBooNE experiment for 6.6e20 POT. The signal is from the Giunti *et al.* best fit point

Bins [GeV]	$\mu \to \nu_e$	$K^{\pm} \to \nu_e$	$K^0 \to \nu_e$	$\nu + e^-$	NC π^0	$\Delta \to N\gamma$	ν_μ CC	Dirt	Cosmic	Signal	Total
0.20-0.35	21	10	4	3	29	0	7	34	6	2	113
0.35-0.50	38	20	6	2	18	1	6	9	2	10	101
0.50-0.65	45	26	6	2	8	1	4	2	1	16	94
0.65-0.80	42	32	8	1	4	1	3	0	1	16	92
0.80-0.95	38	36	8	1	2	1	2	0	0	12	90
0.95-1.10	33	37	7	0	2	0	2	0	0	9	81
1.10-1.30	35	44	9	0	2	0	2	0	0	7	92
1.30-1.50	26	38	9	0	1	0	2	0	0	4	76
1.50-1.75	23	41	10	0	2	0	2	0	0	2	78
1.75-2.00	14	31	8	0	2	0	2	0	0	1	56
2.00-3.00	18	72	17	0	5	0	4	0	0	1	115
Total	331	388	91	10	75	5	34	46	11		

Table 4.3: Background Rates, broken out by analysis bin and origin, for the ICARUS-T600 experiment for 6.6e20 POT. The signal is from the Giunti *et al.* best fit point

Bins [Gev]	$\mu \rightarrow \nu_e$	$K^{\pm} \rightarrow \nu_e$	$K^0 \rightarrow \nu_e$	$\nu + e^-$	NC π^0	$\Delta \rightarrow N\gamma$	ν_μ CC	Dirt	Cosmic	Signal	Total
0.20-0.35	585	151	59	59	504	1	112	23	3	62	1496
0.35-0.50	938	282	99	137	299	13	95	10	1	81	1874
0.50-0.65	1076	417	134	20	120	21	58	5	0	58	1851
0.65-0.80	961	579	155	19	54	23	37	2	0	41	1831
0.80-0.95	769	622	158	32	33	13	22	1	0	24	1651
0.95-1.10	619	641	172	51	22	7	14	1	0	14	1528
1.10-1.30	607	866	210	32	28	4	13	1	0	9	1761
1.30-1.50	391	817	167	26	33	1	12	1	0	4	1449
1.50-1.75	339	864	186	7	51	1	21	0	0	2	1468
1.75-2.00	203	660	168	0	25	0	25	0	0	1	1083
2.00-3.00	231	1360	267	7	84	1	77	0	0	1	2026
Total	6721	7260	1776	389	1252	86	486	44	5		

Chapter 5

Systematic Uncertainties in the Short Baseline Neutrino Program

In the previous chapter, the motivation for the Fermilab Short Baseline Neutrino program was presented and the expected event rates were shown, as well as the methods of calculating an expected signal from a 3+1 model. However, the most detailed simulation (or data analysis, for that matter) is not consequential without a robust calculation of systematic uncertainties.

In this chapter, the systematic uncertainties for the Short Baseline are discussed. Of particular importance are the uncertainties from the flux and neutrino interactions. The flux for the Booster Neutrino Beam, while among the best known neutrino beam fluxes, still has residual uncertainties of up to 15% [71]. Similarly, the uncertainty in the model of neutrino interactions has a 10 to 15% normalization uncertainty for the quasi-elastic and resonant events that are most important to the oscillation searches. Considering that the amplitude of any sterile neutrino oscillation effect is very small, with oscillation probabilities that peak at 1% or less, constraining the systematic uncertainties in the Short Baseline Program is absolutely essential.

The strength of the Short Baseline Program's oscillation search comes, ultimately, from two factors: the LAr-TPC technology allows excellent event identification and background rejections, and the near detector, SBND, allows for large cancellation of systematic uncertainties. In this chapter, the method for quantifying the cancellation of systematic uncertainties is presented.

5.1 General Framework for quantification of uncertainties

In this analysis, the uncertainties that matter are the systematic uncertainties on the final distribution of event rates. Since the goal is to produce a sensitivity calculation for an expected signal, the numerical value of the sensitivity can be calculated with a χ^2 calculation:

$$\chi^2(\Delta m^2, \sin^2 2\theta) = \sum_{i,j} [N_i^{null} - N_i^{osc}(\Delta m^2, \sin^2 2\theta)] \times E_{i,j}^{-1} \times [N_j^{null} - N_j^{osc}(\Delta m^2, \sin^2 2\theta)], \tag{5.1}$$

where N_i^{null} is the expected event rate in the i^{th} analysis bin with no oscillation signal, and $N_i^{osc}(\Delta m^2, \sin^2 2\theta)$ is the expected event rate in the i^{th} analysis bin if there is an oscillation signal from a 3+1 model with the specified mass splitting and amplitude. In the ν_e appearance analysis, this is simplified to

$$N_i^{null} - N_i^{osc}(\Delta m^2, \sin^2 2\theta) = S_i(\Delta m^2, \sin^2 2\theta) \tag{5.2}$$

where S is the expected signal events from the specified parameters in the i^{th} bin.

$E_{i,j}$ in the χ^2 computation is the covariance matrix, a statistical tool to encode correlated uncertainties. In practice, the computation of the covariance matrix is the most challenging aspect of the χ^2 calculation because it requires careful determination of how the uncertainties under study are correlated. For this work, the correlations of uncertainties are quantified with the "multiple universe" method [1]. Much more will be said about the computation and use of the covariance matrix in Section 5.2.

5.1.1 Multiple Universe Error Propagation and Reweighing methods

In a complex chain of simulation and analysis such as a prediction of event rates in a neutrino detector, it can be challenging to understand the effect of, for example, an uncertainty of hadron production at the proton target on the final distribution of neutrino events in the detector. Some intuitive knowledge is of course present: if the amount of neutrino producing particles generated at the target by proton interactions is under (or over) estimated, the event rates in the final analysis distribution at the detector will also be under (over) estimated. To precisely quantify the relationship between initial variable underlying the simulation and the final distributions of events, a reweighing scheme with multiple universes is used.

Reweighing Events

The models used in the Monte Carlo simulations of neutrino experiments, there is always a class of parameters that feed the models and simulations: the neutrino cross sections dictate how many events appear in the detector; the hadron interaction cross section dictates both the amount and variation of hadrons produced in the beam target. These broad examples are meant to highlight that the Monte Carlo must be based upon not just a physics model but the input parameters to that model. In the case of hadron production when the protons interact with the target, an assumption must be made about the cross section of that interaction. While the Monte Carlo is naturally based on the best estimate of the input parameters, it's insufficient to estimate the uncertainty in the simulation without using the uncertainty on the input parameters.

1. Nothing to do with the cosmological idea of the multiverse

As a concrete example, the beam simulation (originally developed by the MiniBooNE collaboration) for the Booster Neutrino Beam uses the Sangford-Wang parameterization to model the double differential pion production cross section for secondary particles at the target. The parameterization,

$$\frac{d^2\sigma}{dpd\Omega}(p,\theta) = c_1\left(1-\frac{p}{p_B-c_9}\right)\exp\left(-c_3\frac{p^{c_4}}{p_B^{c_5}} - c_6\theta(p-c_7 p_B \cos^{c_8}\theta)\right), \tag{5.3}$$

is a complicated system with eight free parameters which have been fit against data from the HARP and BNL E901 experiments. The parameters are also not independent, but instead can have strong correlations. The knowledge of these parameters is not perfect, and indeed the best fit parameters have imperfect agreement with data (see Figure 5.1). However, the fact that the parameters are correlated allows some freedom to change the fit parameters such that the overall parameterization remains consistent with data. When the parameters are changed from the nominal value to a different, consistent parameterization, it is a different "Universe" for this set of parameters. It's worth noting that the variation in the cross section that comes about by varying the paremeters is the source of the dashed bands in Figure 5.1.

In general, varying underlying physical parameters to a model produces a new result. Unfortunately, Monte Carlo simulation of neutrino beams and interactions is computationally expensive, and repeating the simulation for every variance of a parameter is not possible. In this case, a 'reweighting scheme' is used. For the moment, assume in a particular universe the Sanford-Wang parameterization above has been increased by a factor X for a particular neutrino in the simulation. Rather than reproduce this neutrino, in the computation of the final event distributions the same event is used in the same energy bin, but is given a relative weight of $1+X$. This factor can be recomputed for every neutrino that is in the final distribution, leading to an event rate distribution that would have been

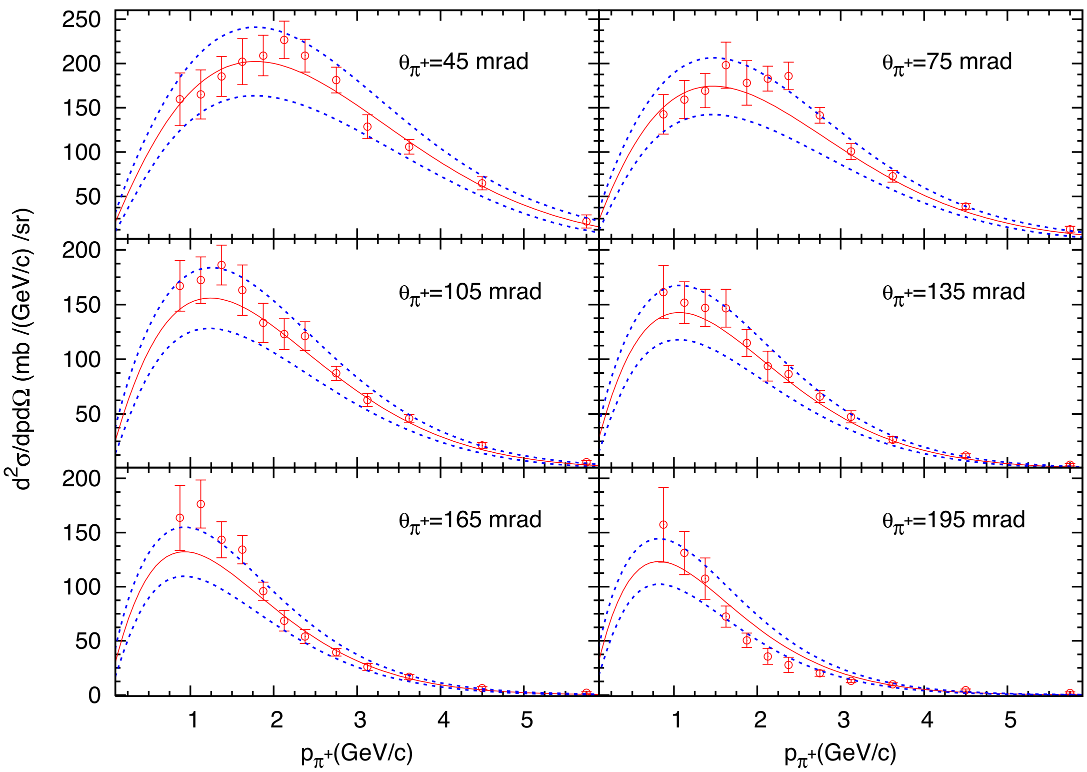

Figure 5.1: The HARP Data (points), and the Sanford-Wang best fit parameterization (solid line). The dashed lines represent a 68% uncertainty band on the parameterization model from varying the fit parameters within their correlated uncertainties. The Figure from [71].

found if the entire simulation were repeated.

In general, this method of 'reweighting' applies new weights to every neutrino in the final analysis for each "Universe." By varying the underlying parameters (in a way that leaves them consistent with constraining data) of a physical model many times, a large sample of universes is obtained, and the event distributions can be computed in each universe. The parameters, however, can not be tweaked completely at random and instead must be drawn according to a Gaussian distribution (if a single uncertainty) or through more complicated methods if a series of correlated parameters. MiniBooNE, for example, varies the Sanford-Wang parameters together through the Cholesky method.

5.2 Determination of Covariance Matrices

Using the methods described above for applying weights on an event-by-event basis, it's possible to generate a suite of "Universes" of event rate histograms, where the value of each analysis bin can be known in each universe as $N^i_{\text{Univ.}m}$. In this document, since there are three detectors under consideration, the vector of event rates in each analysis bin, N, is a concatenation of the vector of event rates in each detector. If there are P total analysis bins in each detector, then

$$\vec{N}_{\text{Nom.}} = \big(\, N^{1,\,SBND}_{\text{Nom.}},\ \ldots,\ N^{P,\,SBND}_{\text{Nom.}},\ N^{1,\,\text{MicroBooNE}}_{\text{Nom.}},\ \ldots, N^{P,\,\text{MicroBooNE}}_{\text{Nom.}},\ N^{1,\,ICARUS-T600}_{\text{Nom.}},\ \ldots\ N^{P,\,ICARUS-T600}_{\text{Nom.}}\,\big) \tag{5.4}$$

and in each universe where an underlying physical parameter has been varied:

$$\vec{N}_{\text{Univ. }m} = \big(\, N^{1,\,SBND}_{\text{Univ. }m},\ \ldots\ N^{P,\,SBND}_{\text{Univ. }m},\ N^{1,\,\text{MicroBooNE}}_{\text{Univ. }m},\ \ldots,\ N^{P,\,\text{MicroBooNE}}_{\text{Univ. }m},\ N^{1,\,ICARUS-T600}_{\text{Univ. }m}\ \ldots\ N^{P,\,ICARUS-T600}_{\text{Univ. }m}\,\big). \tag{5.5}$$

With these vectors, it's possible to calculate deviation from the nominal values due to the underlying uncertainties in an analysis bin:

$$\sigma^i = \sqrt{\frac{1}{M}\sum_{\text{All Univ. }m}^{M}\left(N^i_{\text{Nom.}} - N^i_{\text{Univ. m}}\right)^2} \tag{5.6}$$

This measurement of the uncertainty in this way gives an estimate of the uncertainty in single detector experiments, where bin to bin correlations are ignored. In other words, σ^i is the uncertainty in the i^{th} analysis bin when the existence of all the other bins, in any detector, are ignored. See Figures 5.2, 5.5 for this measurement due to flux and cross section uncertainties, below. In a practical sense, this measurement of the uncertainty is not useful for the computation of sensitivities or significances of a signal, but only provides an easily interpreted measure of the uncertainty of a single detector experiment.

A more useful statical tool is the covariance matrix, E, defined at each bin as

$$E^{i,j} = \frac{1}{M} \sum_{\text{All Univ. } m}^{M} \left[N^{i}_{\text{Nom.}} - N^{i}_{\text{Univ. m}}\right] \times \left[N^{j}_{\text{Nom.}} - N^{j}_{\text{Univ. m}}\right]. \tag{5.7}$$

Covariance matrices that arise from uncertainty sources that are uncorrelated are separable, in the sense that for a complete analysis the final covariance matrix can be constructed as the sum of the matrices from each source. In this analysis, a covariance matrix is calculated for the flux and cross section uncertainties for beam intrinsic events, and the matrix is estimated for the backgrounds from "Dirt" and cosmic induced events, as well as detector systematics.

$$E = E_{\text{Stat.}} + E_{\text{Flux}} + E_{\text{Cross Section}} + E_{\text{Dirt}} + E_{\text{Cosmic}} + E_{\text{Det. Syst.}} \tag{5.8}$$

The covariance matrix is more easily visualized in the form of some of it's transforms, the fractional covariance matrix

$$F^{i,j} \equiv \frac{E^{i,j}}{N^{i}N^{j}} \tag{5.9}$$

and the correlation matrix

$$C^{i,j} \equiv \frac{E^{i,j}}{\sqrt{E^{i,i}}\sqrt{E^{j,j}}}. \tag{5.10}$$

See Figures 5.3, 5.6 for examples of the fractional covariance matrix, and Figures 5.4, 5.7 for examples of the correlation matrix. The fractional error matrix shows which analysis bins have the largest systematic uncertainty, though because it is relative it can be deceiving: bins with high systematic uncertainties might not be important bins in the analysis.

The correlation matrix is an excellent visualization of the power of the covariance matrix technique. It is limited to between -1 (full anticorrelation) and 1 (full correlation), and each entry at bin (i, j) displays how correlated the i^{th} bin is to the j^{th} bin. This is the vital information that allows correlated uncertainties in a multi detector experiment to cancel:

a deviation at the far detector becomes significant (even if it is within the nominal uncertainty at that bin given by Eq. 5.6) if the deviation is not seen at a near detector **and** the correlation between near and far is large. The correlation matrices show the magnitude of exactly that correlation, while the covariance matrix (5.7) is the mathematical tool that carries correlation information to the χ^2 calculation.

5.3 Uncertainties from Neutrino Flux

As might be expected, the neutrino flux is highly correlated across the three detectors in the Booster Neutrino Beam. However, the exact shape of the flux is not identical, especially at the near detector. Figure 2.4 shows the flux at the three detectors.

The covariance matrix for the uncertainties from the neutrino flux is built, as described above, using a multi universe approach. As alluded to in Table 2.1, the uncertainties from the neutrino flux are well quantified by MiniBooNE. However, their uncertainty calculations concerned a single detector, while the SBN Program is a multi detector experiment. To properly quantify the correlated uncertainties between the three detectors, the flux at each detector has to be varied (using the multiple universe reweighting scheme above) consistently: in the N^{th} Universe, the underlying physical parameters that have been changed are changed identically in all three detectors. The event distributions can be calculated again in each universe, for all three detectors, and from them the covariance distribution is built for the flux uncertainties.

For the results shown here, the following uncertainties are considered in the computation of the flux covariance matrix:

- Primary production of π^+ , π^- , K^+ , K , and K_L^0 in p+Be collisions at 8 GeV
- Secondary interactions of p, n, $\pi^\pm$ in the beryllium target and aluminum horn
- Beam focusing with the magnetic horn

Primary hadron production uncertainties, whenever available, are taken directly from the measured cross sections which are used to constrain the Monte Carlo. In the case of charged pion production, the experimental uncertainties reported by the HARP experiment on their measurements are directly used to set the allowed variation within the beamline simulation [75].

For secondary interactions, the total cross sections are varied for hadrons on Beryllium and Aluminum. Also, the inelastic and the quasielastic cross sections are varied. Table 5.1 summarizes allowed variations on hadron-Be and hadron-Al cross sections in the simulation. The total cross section, σ_{TOT}, the inelastic cross section, σ_{INE} ; and the quasi-elastic cross sections, σ_{QEL} are varied separately for nucleons and pions interacting with Be and Al. When σ_{INE} and σ_{QEL} are varied, the cross section of the other is changed to hold the total cross section constant.

Table 5.1: Cross section variations for the study of systematic uncertainties from secondary interactions of hadrons in the target area. The cross section is offset by the amount shown in the table.

	$\Delta\sigma_{\mathrm{TOT}}$ (mb)		$\Delta\sigma_{\mathrm{INE}}$ (mb)		$\Delta\sigma_{\mathrm{QEL}}$ (mb)	
	Be	Al	Be	Al	Be	Al
(p/n) - (Be/Al)	± 15.0	± 25.0	± 5.0	± 10.0	± 20.0	± 45.0
$\pi^{\pm}$ - (Be/Al)	± 11.9	± 28.7	± 10.0	± 20.0	± 11.2	± 25.9

Beam focusing systematics include uncertainty on the magnitude of the horn current(174 $\pm$ 1 kA) as well as skin depth effects. the horn. The skin depth effect allows the magnetic field, flowing on the surface of the conductor, to penetrate into the interior of the horn conductor.This creates a magnetic field within the conductor that can lead to deflections of charged particles which traverse the conductor, especially at higher energy when particles which do not penetrate deeply into the conductor. The effect can be approximated by modeling an exponentially decreasing field to a depth of about 1.4 mm. To asses the systematic the field is turned on and off, which leads to an energy dependent effect of 1 to 18% for particles of ¡ 1 GeV to 2 GeV, respectively [71].

This work does not include a systematic uncertainty on downstream interactions of hadrons with surrounding material, such as air, concrete, steel, etc. These effects were studied by the MiniBooNE collaboration and found to contribute only a few percent to the ν_e and ν_μ fluxes (1% to ν_μ, 2% to ν_e). Therefore, even a large uncertainty on downstream interaction would make a very small impact on the total uncertainty.

Figure 5.2 shows the overall level on uncertainty on the event rates of electron neutrino backgrounds coming from flux uncertainties. As described above, the events selected as ν_e's are largely electron neutrinos with some background from neutral current interactions and charged current ν_μ interactions. The uncertainties shown in Figure 5.2 reflect the mixed composition of the background: in a "Universe" where the flux has varied, the ν_e and ν_μ fluxes have been changed together and so all components of the background model are varied in a consistent way.

Naturally, the flux covariance matrix only applies to the part of the background that originates with the neutrino beam. The cosmic background is independent of the flux, and though the "dirt" background does correlate with the beam, it is treated independently since the correlation is second order.

5.4 Uncertainties from Neutrino Interactions

After the flux uncertainty, the largest remaining uncertainty in a multidetector analysis is the uncertainty coming from neutrino interactions. In particular, the flux and cross section uncertainties combine to form the overall normalization uncertainty on the event rates.

The use of the covariance method to compute a χ^2 would be incorrect if the major normalization uncertainties were not all accounted for. To address this, the systematic uncertainties from the neutrino interactions are also addressed with a covariance matrix. As the simulation uses GENIE [117] to simulate neutrino interactions within argon, the same event generator was used to calculate the systematic uncertainties for cross sections.

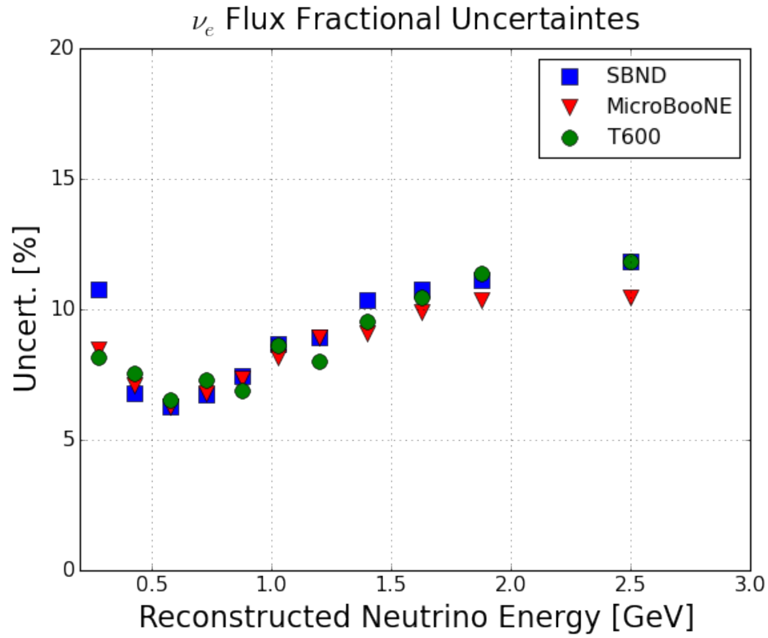

Figure 5.2: The systematic uncertainties in the ν_e appearance event rates for the SBN program, coming from uncertainties in the neutrino flux. This includes flux-based uncertainties for both the ν_e component, from the ν_e flux, and the ν_μ misidentified component of the background.

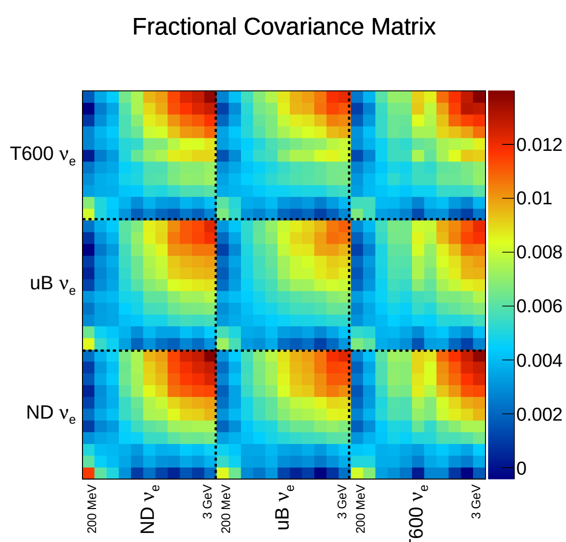

Figure 5.3: The fractional covariance matrix for the flux uncertainties. The uncertainties are highest in the tails of each detector's distributions.

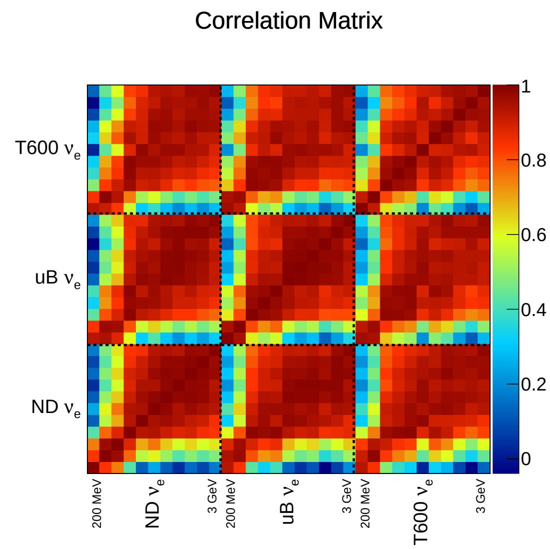

Figure 5.4: The correlation matrix for the flux uncertainties. The uncertainties are highly correlated across the three detectors, which is essential to achieving a strong cancellation between detectors.

At it's core, GENIE is a cross section calculator for neutrino interactions. It models known interactions by computing cross section splines for a reaction between a specific flavor of neutrino and a nuclear target. These splines are slow to create, and need to be comprehensive to have accurate results in the simulation. At runtime, however, GENIE doesn't recompute cross sections for a particular neutrino onto a target if it is already computed, it just accesses the spline for the information.

All of the cross sections that GENIE computes are based on theory or fits to experimental data, and hence the parameters used (in the theory or fits) have some systematic uncertainty associated with them. By varying these parameters according to their 1 σ uncertainty, and recomputing the cross section, a weight can be applied to the event as described above in section Section 5.1.

The GENIE framework provides a model for consistent variations of systematic uncertainties. When, for example, a total cross section is constrained by data and a variation is requested on a subset of that total cross section, the other subsets are adjusted to compensate. This gives a consistent "Universe" across all neutrino interactions when the

Table 5.2: Genie Cross Section Variations and their nominal uncertainty, from [118]

Parameter	**Description**	**Nominal Variation**
M_A^{CCQE}	Axial Mass for CC Quasi-Elastic	-15% +25%
M_A^{CCRES}	Axial Mass for CC Resonance Production	±20%
M_A^{NCRES}	Axial Mass for NC Resonance Production	±20%
$R_{bkg}^{\nu p,CC1\pi}$	Non-resonance Background in CC 1 π production	± 50%
$R_{bkg}^{\nu p,CC2\pi}$	Non-resonance Background in CC 2 π production	± 50%
$R_{bkg}^{\nu n,CC1\pi}$	Non-resonance Background in CC 1 π production	± 50%
$R_{bkg}^{\nu n,CC2\pi}$	Non-resonance Background in CC 2 π production	± 50%
$R_{bkg}^{\nu p,NC1\pi}$	Non-resonance Background in NC 1 π production	± 50%
$R_{bkg}^{\nu p,NC2\pi}$	Non-resonance Background in NC 2 π production	± 50%
$R_{bkg}^{\nu n,NC1\pi}$	Non-resonance Background in NC 1 π production	± 50%
$R_{bkg}^{\nu n,NC2\pi}$	Non-resonance Background in NC 2 π production	± 50%

underlying parameters are adjusted.

Table 5.2 shows the parameters that were varied in the GENIE cross section calculator for this analysis. In each “Universe,” every parameter was varied within it’s 1 σ Gaussian distribution and the weights for each interaction were calculated, for a total of 250 universes. Figure 5.5 shows the level of uncertainty in the detector’s final ν_e event rates arising from the cross section uncertainties. This is, without a multi detector analysis, a very large source of uncertainty on the interaction rates.

As seen in Figure 5.7, the cross section uncertainties across the detectors (and amongst the analysis bins within a detector) are highly correlated. The even correlation indicates that the uncertainty is largely a normalization uncertainty, and not indicative of a different uncertainty in the energy dependence of the cross section, for example. The only regions where the correlation is not as strong is the lowest energy bin to the higher energy bins in each detector. Since the lowest energy bin has the highest rate of misidentified events, coming from Neutral Current pion producing interactions, it is sensible that this bin is less

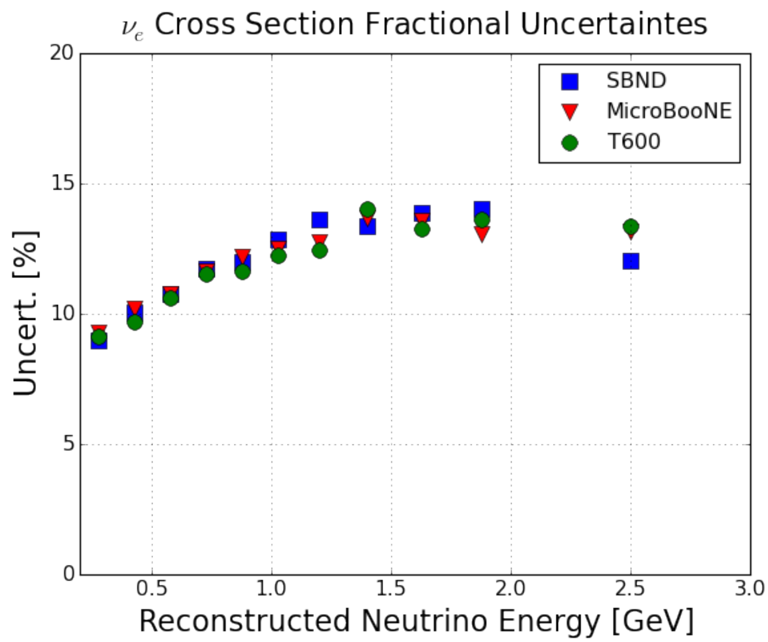

Figure 5.5: Fractional uncertainties at each detector in the ν_e analysis due to neutrino interaction uncertainties.

correlated to the rest.

Despite the very high correlation of cross section uncertainties, there are two caveats to this part of the study of systematic uncertainties in the SBN Program. First, the uncertainties studied did not include final state interaction variations. Because this is a Charged Current inclusive analysis, the final state interaction uncertainties should have minimal impact on the final result. Any analysis that uses an exclusive channel, such as CC ν_e 0 pion, would need a very careful study of the neutrino generator model and it's included uncertainties.

Second, the GENIE neutrino generator includes a package for systematic uncertainty study, however this list of channels studied is not expected to be 100% comprehensive. Instead, it serves to validate and quantify the level of correlation between the SBN detectors.

Despite these caveats, the conclusion of the cross section analysis is quite strong: whatever systematic uncertainties arise from neutrino interactions, they are very strongly correlated across the 3 detectors. The quantification of that correlation is encoded in the covari-

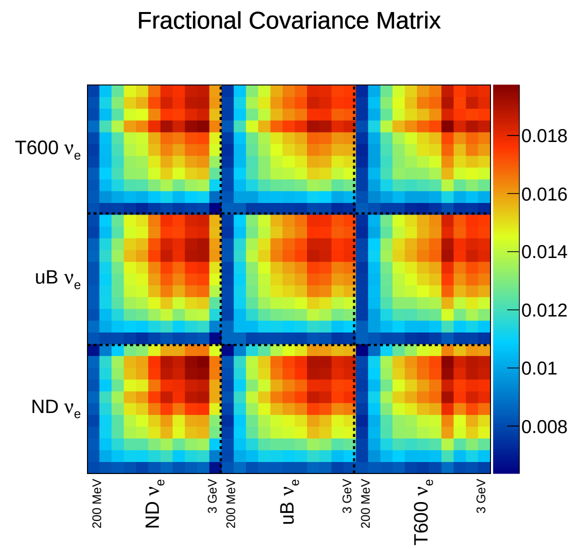

Figure 5.6: The fractional covariance matrix from the cross section uncertainties.

ance matrix, Figure 5.6.

5.5 Residual Systematic Uncertainties

After considering the flux and cross section uncertainties in detail, it is reasonable to ask what is the residual systematic uncertainty on a ν_e appearance measurement in the SBN Program.

There are two types of uncertainties that are not studied in great detail yet, correlated and uncorrelated. Some examples of correlated uncertainties that will be studied in the future, before the final analysis, are

- **Reconstruction Efficiencies** - the three detectors of the SBN Program will all use the same suite of reconstruction tools to build their event rates. The efficiency will not be perfect, as no set of particle reconstruction software ever is, however the systematic biases introduced by the reconstruction will be correctable through Monte Carlo and well correlated between the detectors. For the study shown here, reconstruction efficiencies are assumed to be the same across all three detectors.

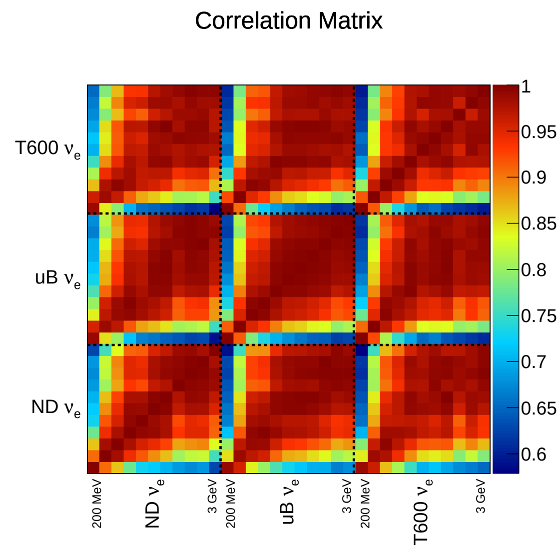

Figure 5.7: The correlation matrix for the cross section uncertainties in the ν_e analysis. As seen by the very high correlation across the analysis bins, the cross section uncertainties are mostly a normalization uncertainty and not a shape uncertainty.

- **Cosmogenic Backgrounds** - the cosmogenic background, which occurs when a cosmic particle produces an interaction that is mistaken for an electron neutrino, will be mostly correlated between the three detectors. There is some variance in the building geometries, such as overburdens and cosmic tagging systems (muon detectors external to the cryostat), however the basic cosmic flux at all three detectors will be correlated. Further, the cosmogenic background can be measured with nearly arbitrary precision with off-beam spills. That is, since the neutrino beams are pulsed there are clear samples of data with **no** neutrinos, which can be used to measure the amount of cosmogenic misidentification as electron neutrinos. Under this assumption, the covariance matrix for the cosmic sample is the statistical uncertainty of the cosmic misidentification in the accepted event samples.

On the other hand, residual uncorrelated uncertainties include

- **Detector Effects** - The three detectors of the SBN Program, while all LArTPCs, are not identical detectors in the same way that Daya Bay is, for example [119]. As described in Section 4.2, the three detectors have some differences. MicroBooNE is a single drift detector, while ICARUS-T600 and SBND are dual drift TPCs with a cathode in the middle. Further, the fiducial volumes of the detectors are different, and the ability to contain neutral particles and electromagnetic particles is different due to the different shape of the detectors.

- **"Dirt" Backgrounds** - the backgrounds produced by the beam but externally to the detector will, to first order, be uncorrelated between detectors. The overall rate will fluctuate up or down with the neutrino flux, however the complexity of the surrounding material of the detectors makes the evaluation difficult. Therefore, to be conservative, a 15% uncertainty is applied to the "Dirt" backgrounds at each detector. This is assumed to be fully correlated within each detector's analysis bins, but uncorrelated across detectors.

Before a final analysis is released, these systematics uncertainties must be carefully addressed.

5.6 Sensitivity to Anomalous ν_e Appearance at the SBN Program

To evaluate the expect sensitivity of the SBN Program, the above covariance matrices are used as shown in Equation 5.8. The χ^2 measure of sensitivity is computed as in Equation 5.1. The final sensitivity to ν_e is shown in Figure 5.8. As an alternative view to this sensitivity, the quoted sensitivity in Figure 5.9 shows the $\sqrt{\chi^2}$ of calculated along the left edge of the LSND 90% confidence region.

The sensitivity calculations shown here are the basis for the Short Baseline Neutrino Program proposal, submitted in 2014 to the Fermilab Physics Advisory Committee. Since then, the proposal has been accepted and the SBND and ICARUS experiments are being designed and constructed (SBND) and refurbished and delivered (ICARUS) to Fermilab.

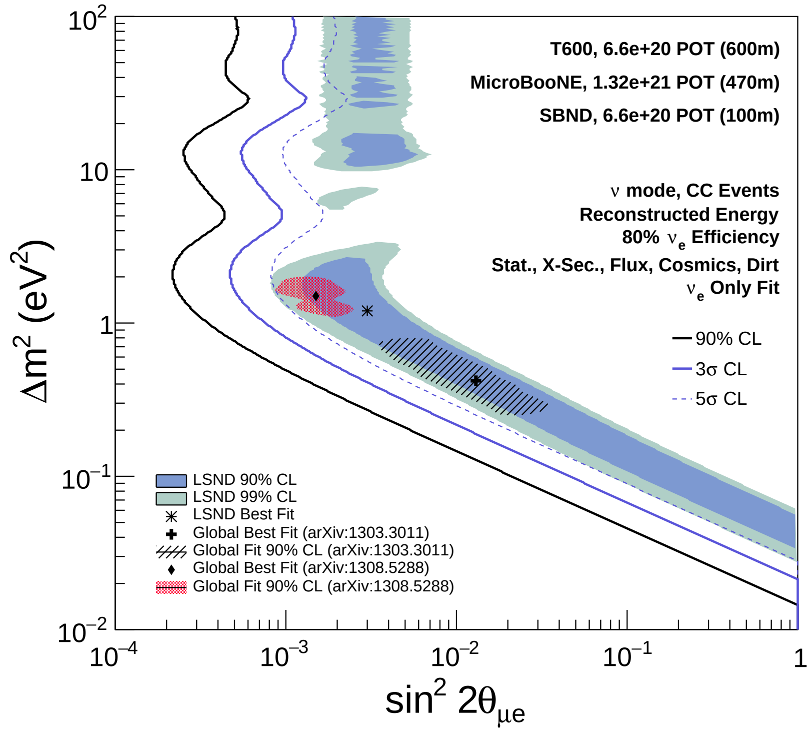

Figure 5.8: The SBN Program's quoted sensitivity, under all the assumptions shown above. At the best fit points from [107] and [116], the significance is well above 5 σ.

The full SBN Program should be commissioned and running by 2018.

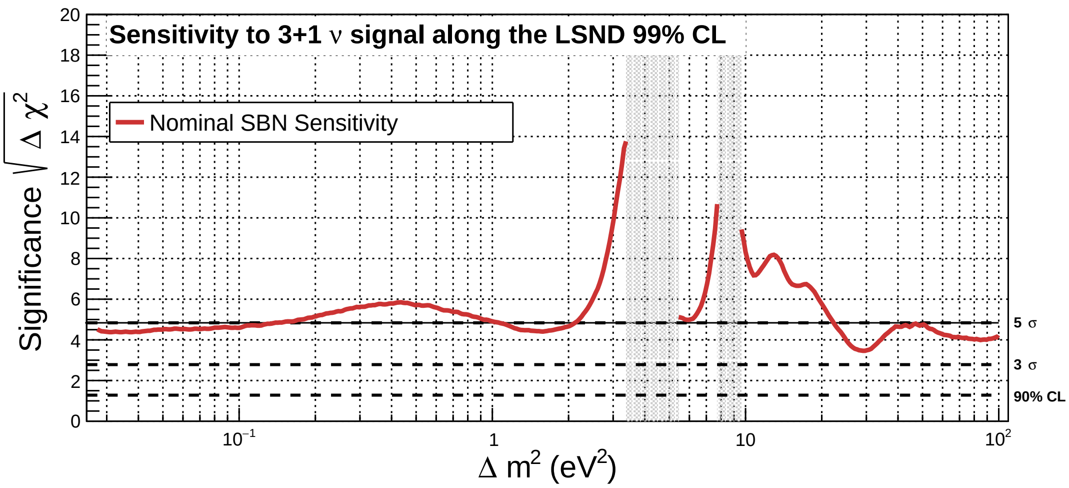

Figure 5.9: The SBN Sensitivity along the lower edge of the LSND 90% confidence allowed region. Because of the low $\sin^2 2\theta$ values along the LSND regions left edge, this is a region with a very small and difficult to measure signal. Therefore, it is a good parameter space with which to measure the SBN Sensitivity.

Chapter 6

Electron Neutrinos in Liquid Argon

As seen in Chapter 4, the detection and measurement of electron neutrinos in the SBN program (and for DUNE) is essential to its success. This chapter describes the detector signatures of electromagnetic showers, and presents a method to identify and reconstruct high energy gammas and electron neutrinos. This work is the first observation of low energy electron neutrinos in a liquid argon time projection chamber.

Essential to detecting ν_e signals is the rejection of photons from the electron candidate sample. This chapter also presents the first demonstration of two methods to reject photons from electron candidates using data from the ArgoNeuT detector: topological separation and calorimetric separation.

6.1 Electromagnetic Showers in Liquid Argon

An electromagnetic shower can originate in two ways. In the first, a high energy electron (produced as the outgoing lepton of a ν_e interaction, for example $\nu_e + n \rightarrow e + p$) will travel through the argon freeing ionization electrons as it goes. Eventually, the electron will scatter off of an argon nucleus. This rapid acceleration will cause the electron to emit a bremsstrahlung gamma ray. This gamma can pair produce in the presence of an Argon nucleus or orbital electron, producing a secondary high energy electron and positron. The

e^+/e pair will then each produce a cascade, similar to the original electron, until the energy is depleted: electrons or positrons emitting bremsstrahlung photons, and the photons pair producing or Compton scattering to produce more charged particles. Naturally, when all of the energy of the original particle has been exhausted by ionization of Argon from the charged particles, the shower will stop.

The second way to produce an electromagnetic shower originates with a high energy photon, also called a gamma, instead of an electron. A common source of gammas in neutrino experiments is from the decay of neutral pions: $\pi^0 \to \gamma\gamma$. When the photon interacts, it most often pair produces near a nucleus (at energies typical of those photons produced by neutrino interactions). The process is identical to the electron-induced shower after the first particles, and so electromagnetic showers from photons and electrons are only different in the original particles.

The primary method of discrimination between electrons and gammas exploits the value of the radiation length ($X_0 = 14$ cm) in argon, which is large compared to the excellent spatial resolution of TPCs. This means that a gamma can leave a visible gap between its origin and the place in the TPC where it interacts. For an electron originating from a CC ν_e interaction no such gap will be present.

High energy gammas can, in some cases, interact at a sufficiently short distance from the neutrino's interaction vertex such that the gap between the vertex is not visible. Further, the hadronic activity at the vertex could be invisible in the TPC data, either because it consists of only neutral particles or because the particles are below detection threshold. Without the presence of hadronic activity to distinguish the neutrino interaction vertex, there is no possibility to observe a gap. In this case, a second method of electron/gamma discrimination uses calorimetry at the start of the electromagnetic (EM) shower. An electron produces ionization consistent with a single ionizing particle, whereas a gamma, at typical neutrino beam energies, converts primarily through pair production - see Figure 6.1. The electron/positron pair produced by a gamma conversion produces ionization consistent with two single ionizing particles. This method is only useful for the first few centimeters of the cascade - once the electromagnetic cascade develops, the amount of ionization can no longer be used to distinguish electron- and photon-induced electromagnetic showers.

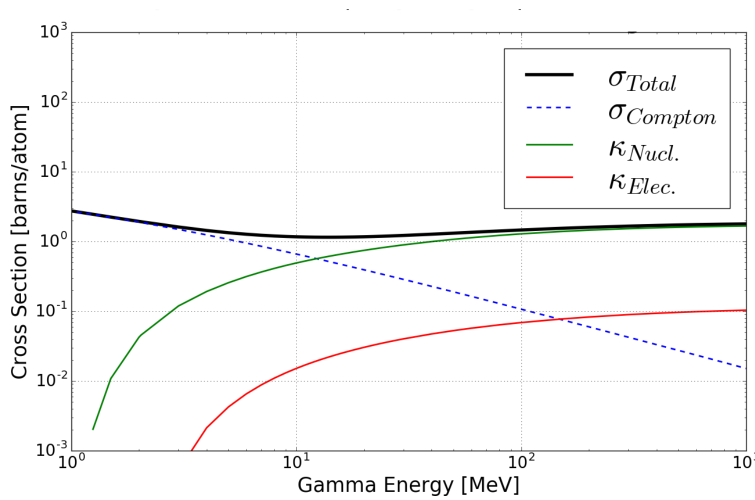

Figure 6.1: The relative cross sections of high energy gammas on Argon between 1 MeV and 1 GeV. Compton and pair production cross sections are balanced at just above 10 MeV. Data are obtained from the Xcom database [120].

For the energies typical of the gammas used in this analysis the distribution of gamma conversion distances is shown in Figure 6.2. There are gammas that convert very close to the generation point (here, 7% of the gammas convert within a centimeter). The definition of "too close" depends on the analysis being performed, however, there will always be a fraction of gammas for which a topological based cut is insufficient to tag them as gammas. In the ArgoNeuT detector, the minimal resolution of a gamma gap is approximately one wire spacing (4 mm). In neutrino interactions with hadronic activity at the vertex, it is possible that other particles can obscure the start of an electromagnetic shower. In this case, even gaps as large as a few centimeters can become unidentifiable.

The calorimetric separation of electrons and photons, using the amount of ionization measured at the start of the shower, depends on the photon interacting through pair production and not Compton scattering. As seen in Figure 6.1, the scatter cross section of photons is dominated by pair production above 100 GeV, though the Compton cross section re-

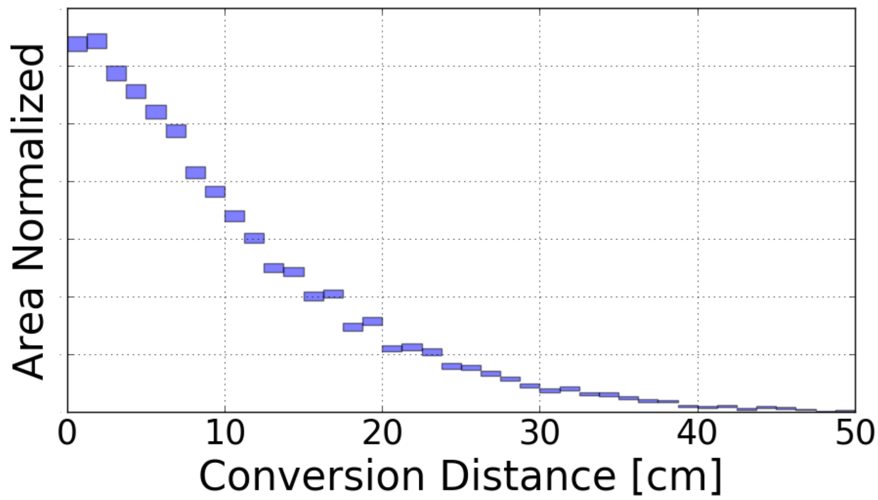

Figure 6.2: The conversion distance of each gamma in the Monte Carlo sample used for this analysis, which is about 7000 gammas in the energy range of several hundred MeV, as modeled by GEANT4 [77].

mains relevant up to 1 GeV of photon energy. Figure 6.3 shows the relative probability that a photon will interact through either Compton or pair production channels. Importantly, a photon that interacts through Compton scatter can not be distinguished via calorimetry from an electron. Instead, only a topological separation can be used on an event-by-event basis for Compton-scatter photons. In most neutrino experiments such as the SBN program [19] and DUNE [74], the high amounts of photons produced compared to expected electron neutrino events makes the fraction of Compton scatter photons a relevant background. Therefore, both methods of separation are crucial.

6.1.1 Selection of Electromagnetic Showers in ArgoNeuT

To validate the separation of electromagnetic showers in LAr-TPCs, a study was performed using the neutrino events from the ArgoNeuT detector to select samples of electron candidate and photon candidate events. A sub-sample of the ArgoNeuT data set containing electromagnetic showers is isolated first, and this sub-sample is used to select well defined electron and gamma events by visual scanning.

Selecting the sub-sample of electromagnetic showers is based on information from the

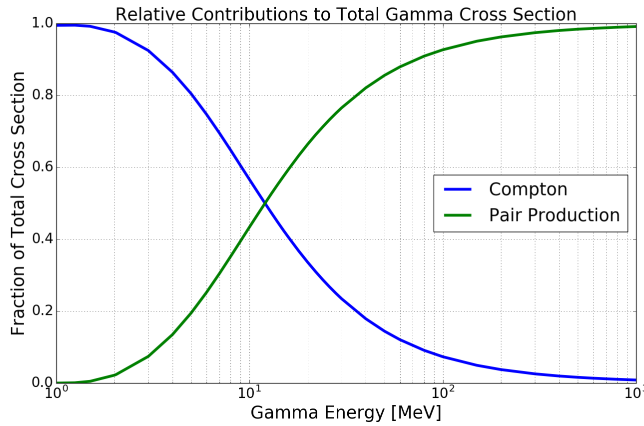

Figure 6.3: The cross section of high energy gammas on Argon between 1 MeV and 1 GeV. Here, κ refers to the pair production cross section for the nuclear field and electron field. Compton and pair production cross sections are balanced at just above 10 MeV. Data are obtained from the Xcom database [120].

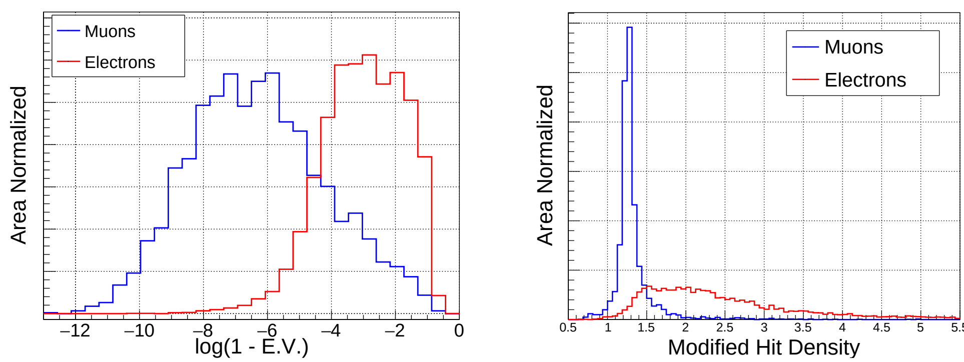

Figure 6.4: Principal Component Eigenvalue (top) and "Modified hit density" (bottom) calculated for single electron showers(red) and muon tracks (blue).

2-dimensional clusters of charge depositions (hits) in each wire plane. First, empty events and events with only track like particles are removed from the sample using an automated filter. This filter considers two-dimensional clusters of hits made with the LArSoft package [98], and calculates several parameters of these clusters to differentiate between track-like and shower-like clusters.

The two most successful metrics in separating tracks and showers for well clustered events are the principal eigenvalue of a principal component analysis (PCA), and a direction corrected hit density of the cluster:

- **Principal Component Eigenvalue:** A principal component analysis (PCA) [121] takes a collection of N dimensional points and numerically finds the orthonormal coordinate system that best aligns to the data. The goodness-of-fit metrics in the PCA analysis are the eigenvalues of the transformation matrix between the initial coordinate system and the best fit. In this analysis, we use the 2D reconstructed charge depositions (hits) in the wire-time views of the collection plane TPC data and perform a principal component analysis on each cluster. For track like particles, which have strong directionality, the first eigenvalue of the analysis is quite high, close to 1. For shower like clusters, the direction of the shower and it's transverse direction are less obviously separated, and the principal eigenvalue is lower than 1.

- **Direction Corrected Hit Density:** A showering event is defined significant activity in the TPC that is resolved away from the primary axis of the particle. That is, a shower has many hits reconstructed as it travels through the TPC, whereas a track generally has one charge deposition detected per step through the TPC. Measuring the hit density, defined as hits per unit distance, along a particle can thus discriminate between tracks and showers. Since hits are only reconstructed on wires, and tracks and showers need not be perpendicular to the wires, the hit density is corrected to account for the fact that high angle tracks and showers (more parallel to the wires) have relatively fewer hits reconstructed.

For this analysis, a cut is made on the value of $log(1-E.V._{PCA}) > -5$ as seen in Figure 6.4. $E.V._{PCA}$ is the first eigenvalue of the PCA analysis. This corresponds to rejecting all clusters that have a principal eigenvalue greater than $\sim$0.999. Events with a corrected hit density greater than 1.5 hits per cm are kept. Figure 6.4 shows these separation parameters obtained using Monte Carlo simulations of single electrons as a model for electromagnetic showers, and single muons and protons as an archetype for tracks.

An additional requirement is that a shower-like cluster in on plane should correspond to an analogous cluster in the second plane at the same drift time. This removes spurious events tagged as showers due to wire noise or other sources in just one plane.

Finally, an additional set of criteria is applied using all of the hits in a single view in an event as a single cluster. These criteria remove high-multiplicity ν_μ deep inelastic scatter events and cosmic ray events which resulted in a large amount of total charge in an event.

This procedure resulted in sample of ArgoNeuT events that contained mostly EM-shower events, from which the final electron and gamma samples are selected.

When a gamma is produced in an interaction in argon, it will travel some distance, typically less than 50 cm in argon (for a 500 MeV gamma), before it interacts with the argon and induces an electromagnetic shower. Thus there is often a gap between the origin of the gamma and the start of the electromagnetic shower. Unless there is other activity in the detector at the location of gamma production, the gap is impossible to detect. Therefore, two types of events are classified as gamma candidates, based on the observation of charged protons or pions at a neutrino interaction vertex: electromagnetic showers pointing back to charged particle activity at a vertex with hadronic interaction, and Neutral Current π^0 events where two electromagnetic showers project back to a common point. In the second case, hadronic activity at the vertex is allowable but not required. Examples of both types of gamma interactions are shown in Figure 6.5. Gammas that are unable to be positively identified purely through topological considerations - if, for example, the electromagnetic shower is the only activity in the detector - are not used in this analysis.

For a sample of electrons, this analysis targeted electron neutrino events as the electron shower candidates. To maximize purity, an electromagnetic shower is selected as an electron candidate only in events that also exhibited hadronic activity at the vertex *without* the presence of a gap between the shower and other particles. In addition, events with a track like particle matched to a muon in the MINOS near detector are rejected. This ensures that the contamination from ν_μ charged current events with high bremsstrahlung activity is negligible. Examples of electron candidates are shown in Figure 6.6. In total, 37 electron candidate showers and 274 gamma candidate showers are selected for this analysis.

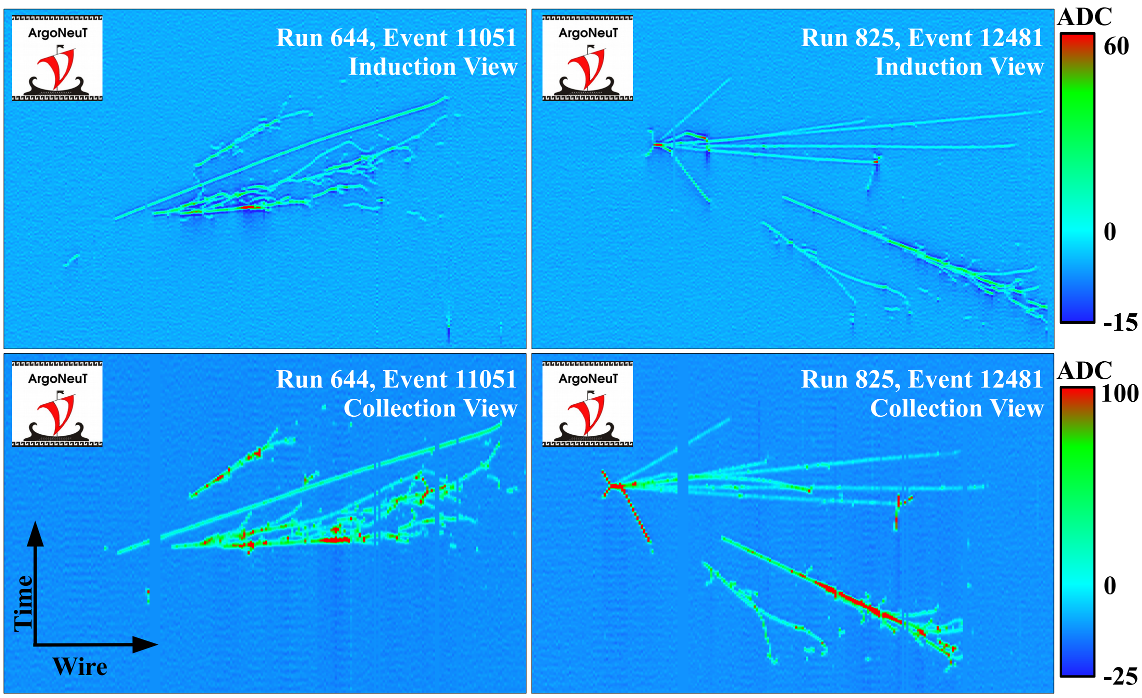

Figure 6.5: Examples of gamma candidate events. The top row are the induction views and the bottom row are the collection views of two events. In both cases, the key identifying feature is the gap between the showers and the other activity to which they point backwards. In the (bottom) collection planes, there is a block of 5 wires that are inactive.

6.2 Reconstructing Electromagnetic Showers in LAr-TPCs

To reconstruct electromagnetic showers in LAr-TPCs, a procedure described in Section 6.2.1 is applied. In general, the raw data from the detector must be deconvolved to mitigate noise sources, and a peak finding algorithm is applied to the signal from each wire to find charge depositions, known as hits. The integral of the ADC count in each hit is used to calculate the charge dQ using an (ADC$\times$Timetick)/Coulomb conversion constant. The constants are obtained using the procedure described in 3.4.4, which follows the procedure in [93].

The most difficult step in the reconstruction of electromagnetic showers, by far, is deciding which hits in an interaction are associated with the shower. For the events selected to

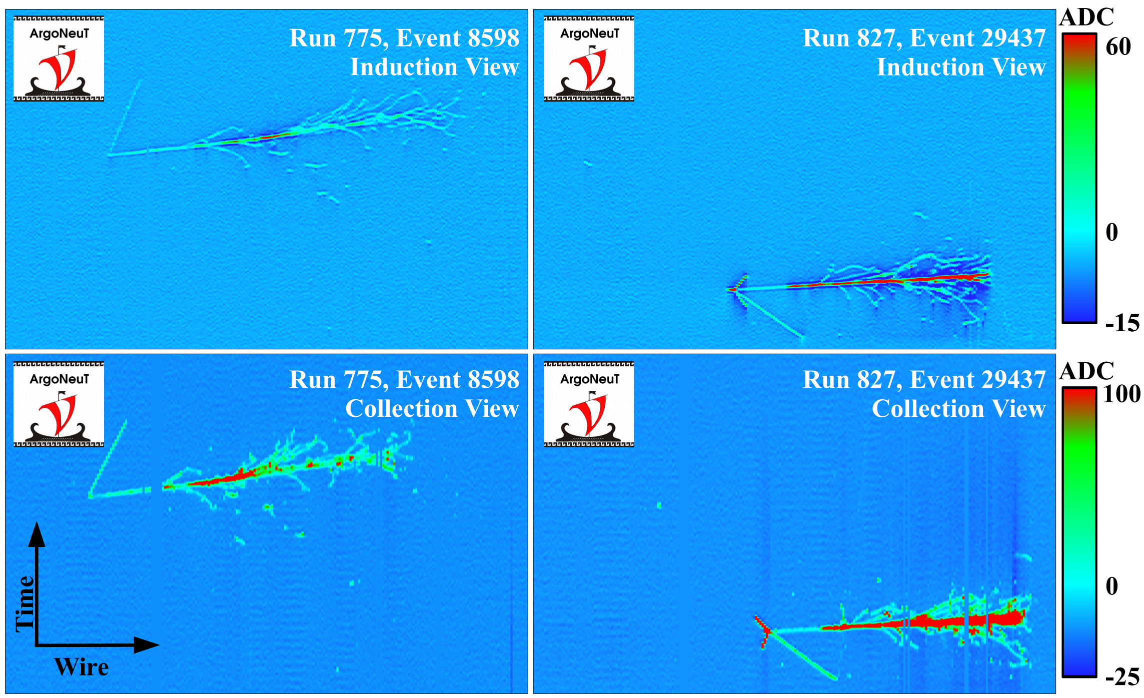

Figure 6.6: Examples of $\nu_e \to e$ CC events. The top row are the induction views and the bottom row are the collection views of two events. In both cases, there is no observable gap between the shower and the hadronic activity.In the (bottom) collection planes, there is a block of 5 wires that are inactive due to a bad electronics connection in the detector.

demonstrate electron/gamma separation, the hits were assembled into appropriate clusters manually.

In order to measure dE/dx correctly, it is extremely important to precisely determine the start point and direction of the shower. In particular, the start point and direction are needed to measure the *first* several centimeters of the shower before the development of the electromagnetic cascade. Once the shower develops, the electron and gamma populations become significantly less distinguishable (see Section 6.5).

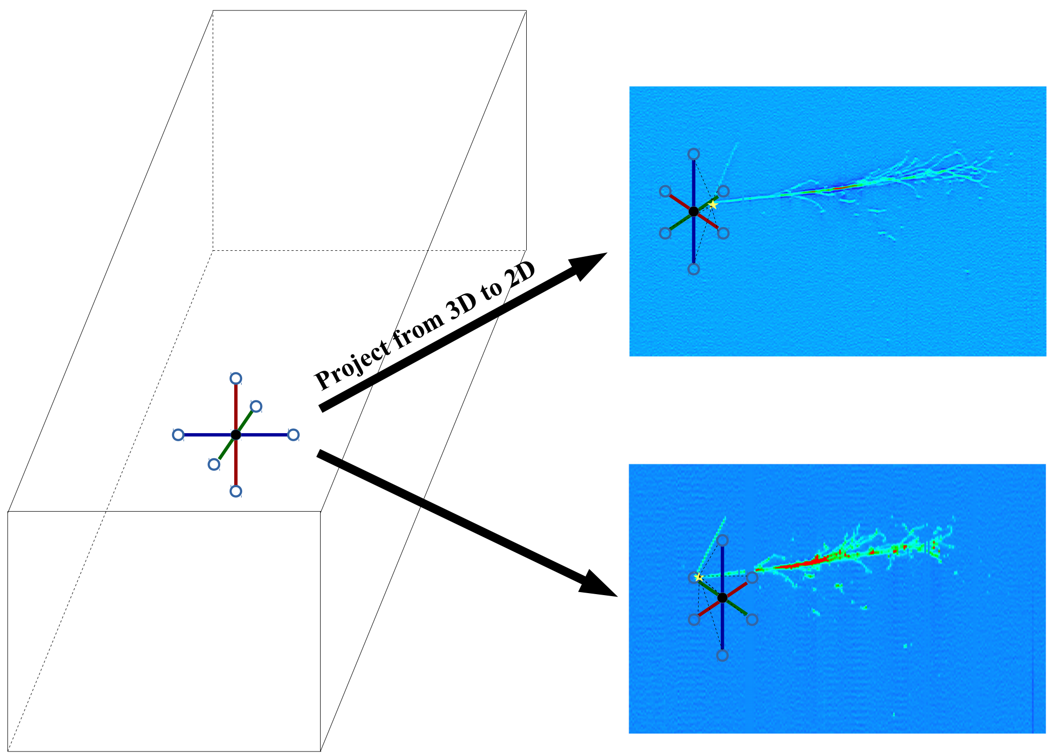

Figure 6.7: Diagram of the 3D start point algorithm.

6.2.1 Reconstruction Algorithms

The 3D start point is initially calculated from the intersection point of the wires where the two 2D start points are found and their position in the drift time coordinate. The start point in 3D is improved using an iterative algorithm, and illustrated in Figure 6.7.

An initial guess, the point in black, is made for the start point based on the 2D start points (yellow stars in each plane). The start point in 3D is projected into each plane, and the error in the 3D start point is the sum (over each plane) of the distance between the true start point in each plane and the projection of the 3D point. Six additional points, along the detector coordinates (in the ± x, y, and z directions), are also projected into each plane, and the error of each point is computed similarly (black dashed lines show the distance between projection and true start point). The point with the smallest summed error is chosen as the better 3D start point, and the algorithm makes an additional six guesses around it. If the central point (in black) is chosen as the best fit point, the distance the other 6 points are offset from it is decreased and the algorithm repeats. This procedure is repeated until the algorithm can no longer improve the accuracy of the 3D start point. The initial offset from the central point for the 6 auxiliary points is 5 centimeters, and it decreases by 2% for each successful iteration. As seen in Figure 6.10, the 3D start point resolution is generally better than 1 cm.

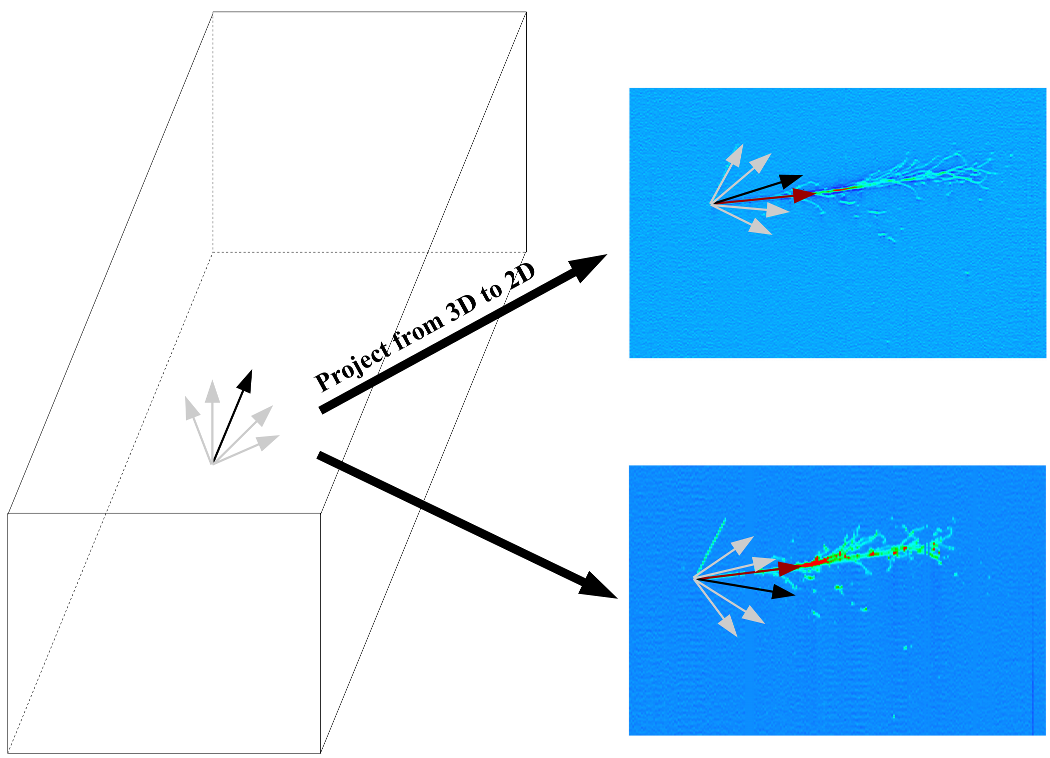

Figure 6.8: Diagram of the 3D start direction algorithm.

Similar to the 3D start point, the 3D axis is computed using an iterative projection matching algorithm. The standard TPC trigonometric formula is used to compute an approximate 3D axis based on the angle of each shower in the collection and induction plane:

$$\theta = \arccos \frac{m}{\sqrt{l^2 + m^2 + n^2}}, \tag{6.1}$$

$$\phi = \arctan\left(\frac{n}{l}\right) \tag{6.2}$$

where

$$l = sign(t_{end} - t_{start}), \tag{6.3}$$

$$m = \frac{1}{2\sin(\alpha)}\left(\frac{1}{\Omega_0} - \frac{1}{\Omega_1}\right), \tag{6.4}$$

$$n = \frac{1}{2\cos(\alpha)}\left(\frac{1}{\Omega_0} + \frac{1}{\Omega_1}\right). \tag{6.5}$$

Here, θ represents the polar angle in 3D with respect to the z axis (approximately the beam direction). ϕ is the azimuthal angle in the x-z plane, with $\phi = 0$ along the z axis, and α is the angle of the wire planes with respect to the vertical direction, which in ArgoNeuT is 60 degrees. Ω_0 and Ω_1 are the tangents of the 2D angles of the shower measured in each plane. t_{start} and t_{end} are the start and end points of the cluster, such that l is positive if the shower points away from the wires and positive the shower points towards the wires.

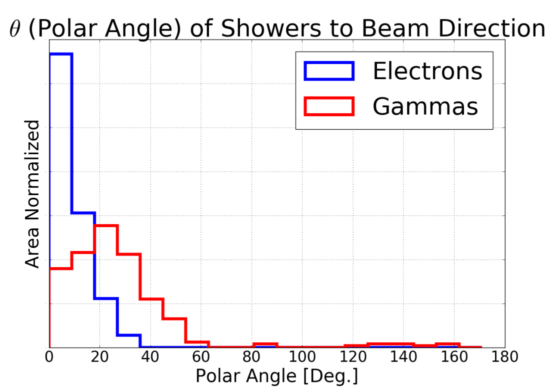

Figure 6.9: The distribution of the polar angle of events with respect to the Z direction (approximately the beam direction). The electron sample is very forward going, and the gamma sample has a wider distribution of angles.

The reconstructed 3D axis is then projected into each plane, and the slope (in 2D) is

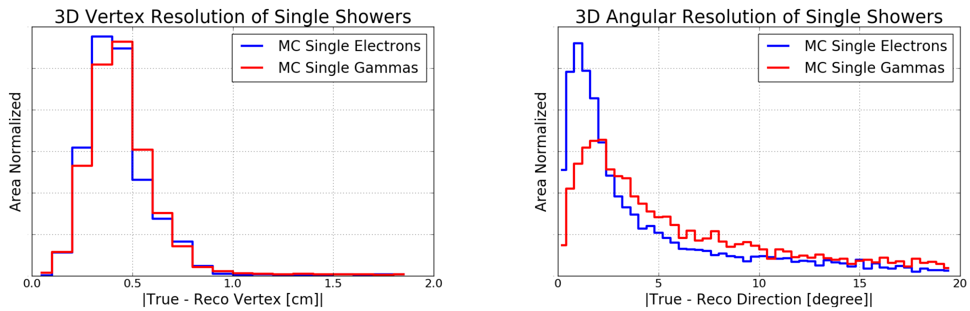

Figure 6.10: The calculated resolution of the 3D start point (left) and angular resolution (right) for single electromagnetic showers generated with the LArSoft package. The angular resolution for gammas is slightly worse than for electrons because the gamma sample is at lower energy, and hence has fewer depositions (hits) in the TPC.

compared against the slope of the electromagnetic showers in each plane. Based upon the quality of the match between the projection and the 2D slopes, the 3D axis is adjusted until the best fit is obtained - see Figure 6.8. An initial guess, the arrow in black, is made for the start direction based on the 2D start directions (red arrows in each plane). The start direction in 3D is projected into each plane, and the error in the 3D start direction is calculated. An additional set of 3D directions (gray arrows) are also projected into each plane. If the central direction (in black) is chosen as the best fit direction, the angular separation between it and the other (gray) directions is decreased and the algorithm repeats. This procedure is repeated until the algorithm can no longer improve the accuracy of the 3D start direction.

The angular resolution for electromagnetic showers, shown in Figure 6.10, is generally quite good (better than 5 degrees) though there is a substantial tail. However, for this analysis, the poor resolution in a few measurements of the 3D axis has a minimal effect on the dE/dx calculation. This is due to the fact that the majority of the events are forward going, as shown in Figure 6.9. Therefore a moderate uncertainty in the 3D angle leads to only a small uncertainty in the effective wire pitch, described below, and a small uncertainty in dE/dx.

Since an electromagnetic shower is a combination of many single ionizing particles - electrons and positrons - and is not composed of highly ionizing stopping particles - i.e.,

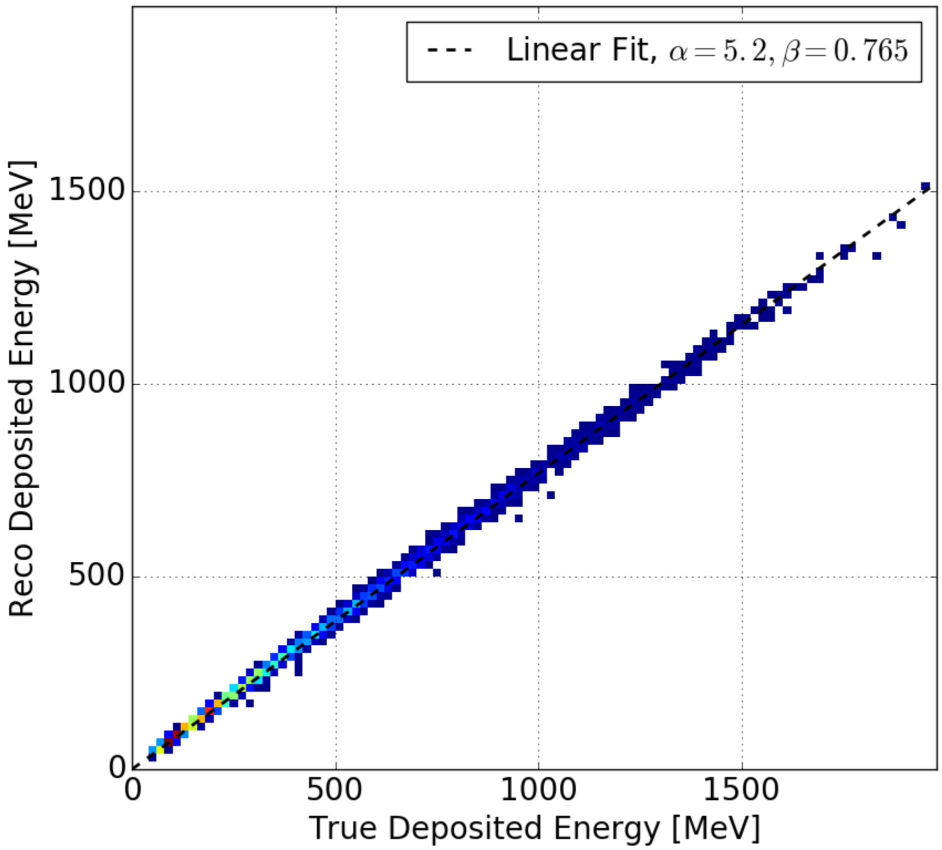

Figure 6.11: The reconstructed, deposited energy of an electron shower compared to the true, simulated deposited energy.

protons - the measured charge on the sense wires in the peak of the showering activity is a sum of many minimally ionizing particles. Therefore, to calculate the total energy deposited by an electromagnetic shower, each deposition collected is corrected by a recombination amount that is proportional to a minimally ionizing particle. All of the energy depositions, once corrected, are summed into a final measure of the reconstructed, deposited energy. Figure 6.11 shows the relationship between the true deposited energy from the simulation and the reconstructed deposited energy of electron showers. The correlation between the two is quite strong, though there is a significant and consistent deficit of reconstructed energy compared to the true energy. This deficit arises from the very small ionizations coming from very low energy photons in the argon, which are far from the main shower and either below detection threshold or not spatially associated with the electromagnetic shower.

Lastly, for the calorimetric separation of electrons and gamma to succeed, the dE/dx metric must be well reconstructed. As the charge depositions are measured discretely in 2D on single wires, in each of the wire planes we use the 3D axis of the shower to calculate an "effective" wire pitch between hits. This effective pitch is, in other words, the real distance in the TPC that a particle travels between its two projections (hits) on adjacent wires. Figure 6.12 shows the distributions of effective pitches for the electron and gamma samples. The effective pitch is at least the wire spacing, which is 0.4 cm in ArgoNeuT. The gamma distribution shows a slightly higher effective pitch, which is expected from Figure 6.9 showing that the gammas are at slightly higher angles to the wire planes than the electron sample. In the calculation of dE/dx, the effective pitch is used as the estimate of 'dx'.

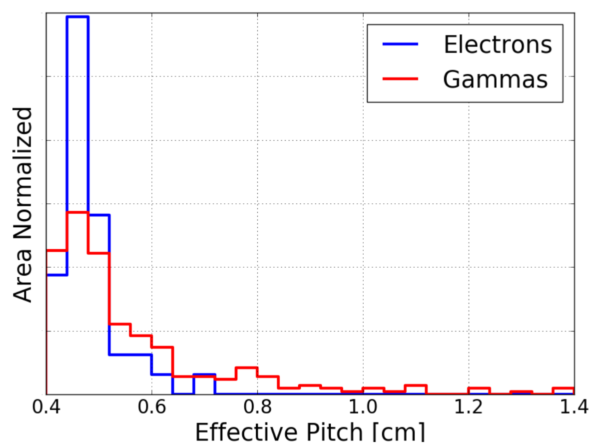

Figure 6.12: The effective pitch for the electron and gamma samples used in this analysis. The effective pitch is a measure of how far a particle travels between depositions of charge recorded on adjacent wires.

A valuable cross-check of this sample of events is the distribution of every dE/dx deposition measured at the start of the shower, from all the events in the selected sample. Figure 6.13 shows this distribution for the Monte Carlo simulation of both electrons and photons. The electron hits follow a Gaussian-convolved Landau distribution, while the

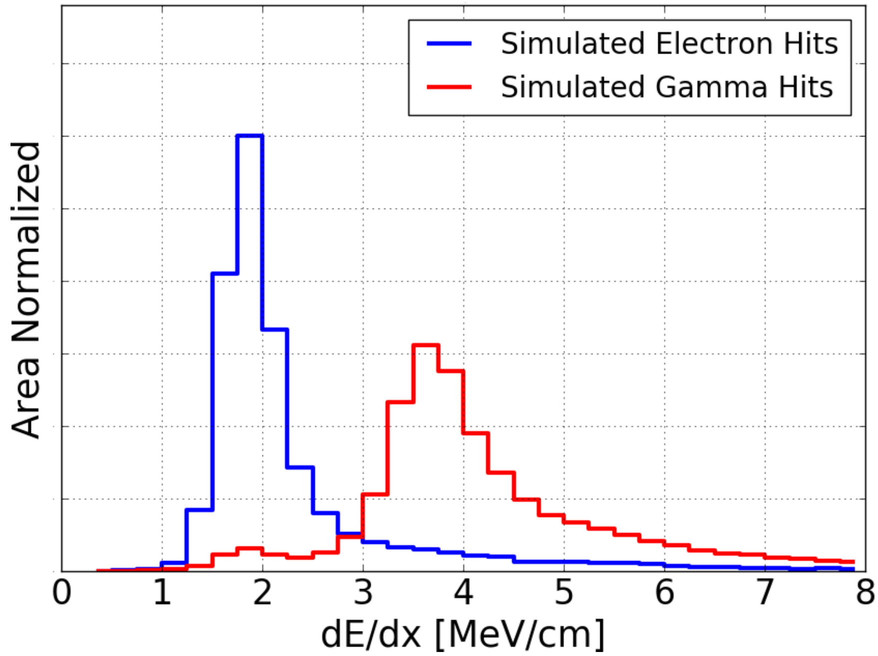

Figure 6.13: Distribution of dE/dx for all hits at the start of the shower for the electron and gamma samples using Monte Carlo.

photon distribution is more complicated due to the presence of two single ionizing particles at the start of both showers. In addition, the photon distribution includes contributions from photons that Compton scatter instead of pair producing.

For the gamma sample, the comparison of data and simulation is shown in Figure 6.14. Since the gamma sample is produced entirely by selecting showers with a displaced vertex, the purity of the gamma sample is taken to be nearly 100% in this analysis.

For the electron sample, we can not assume that the purity of the sample is 100% based on topology alone. As seen in Figure 6.2, a non-negligible amount of gammas will convert at a sufficiently short distance that they will get selected as electrons in a topological based cut. Hadronic activity at the vertex can also obscure the presence of a gap from a gamma. Therefore, the distribution of electron-like dE/dx hits analogous to Figure 6.14 is expected to be modeled by a combination of electron and gamma showers in Monte Carlo.

In Figure 6.13, the simulated dE/dx distributions for electrons and gammas are shown. These two distributions are used to fit to the equivalent distribution of the electron-candidate

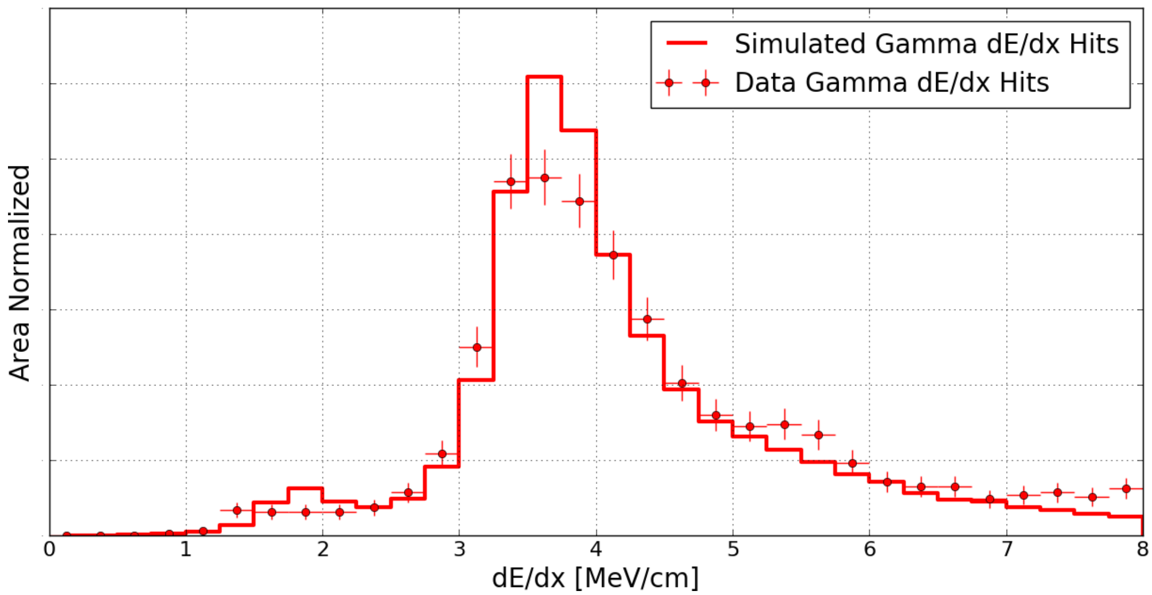

Figure 6.14: Distribution of dE/dx for all hits at the start of the shower for the gamma sample.

data sample, using a linear combination of electron and gamma Monte Carlo such that the normalization is fixed. The χ^2/dof is minimized between the (area normalized) data distribution and the combination of the electron and gamma distributions from Monte Carlo. The best fit is shown on the right side of Figure 6.15. The χ^2/dof decreases from 2.78 with no gamma contamination to 1.02 when a gamma contamination is included at $20 \pm 15\%$. This represents a direct measurement of the misidentification rate of the topological selection of electrons for this particular analysis, and demonstrates a method to measure this mis-ID rate in future electron neutrino searches in LArTPCs.

As a final verification of the reconstruction, the measured distribution for the electron candidates is corrected by subtracting the gamma distribution from Figure 6.15, scaled by the 20% found above. This background subtracted distribution is fit with a Gaussian-convolved Landau distribution to determine the most probable value of charge deposition. In particular, the most probable value of dE/dx for electron like hits is consistent with the theoretical values as shown in Figure 6.16. For electrons above 100 MeV/c, as this sample is, the theoretical expectation of the most probable ionization is 1.77 MeV/cm. This is in

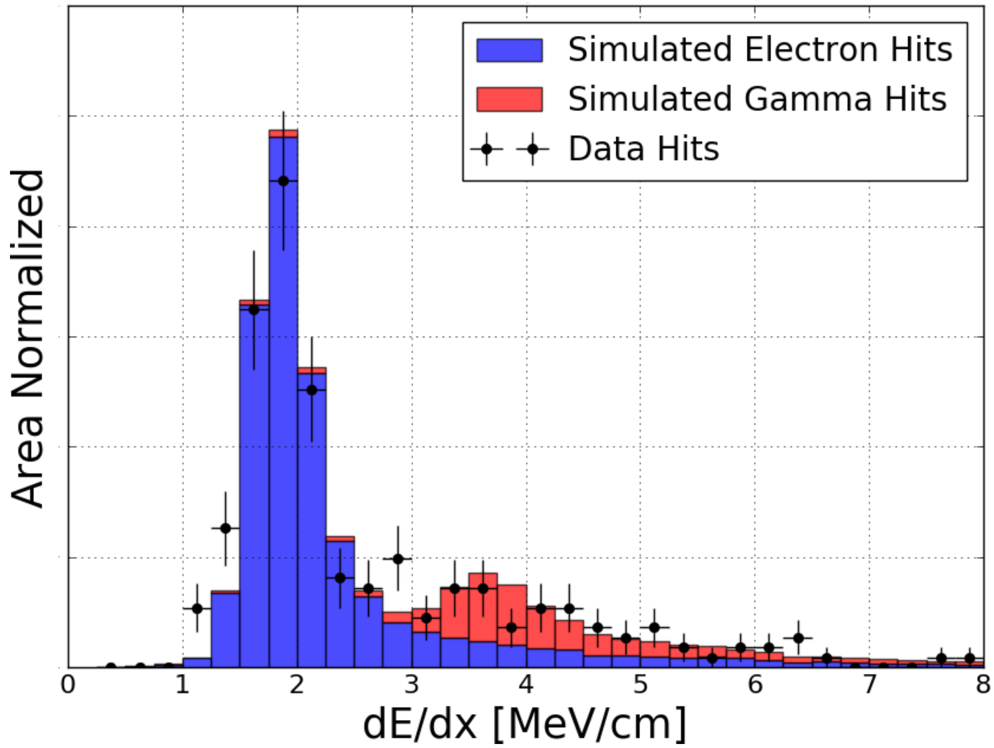

Figure 6.15: All dE/dx hits from the electron candidate sample, compared to a sample of Monte Carlo comprised of 80% electrons and 20% gamma.

good agreement with the fitted value of 1.74 MeV/cm.

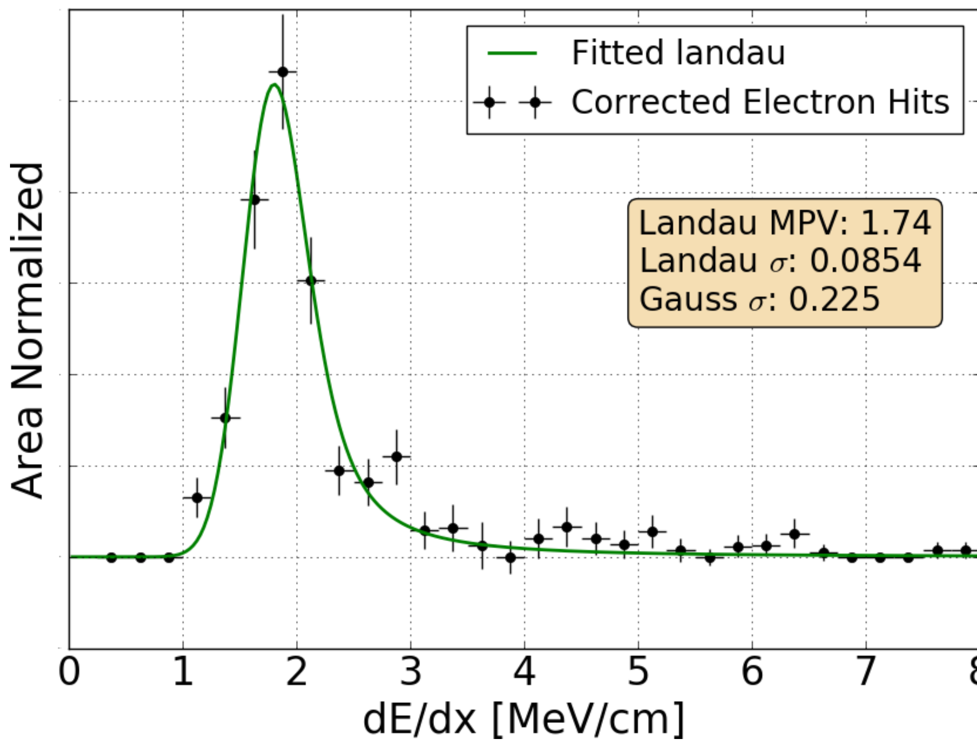

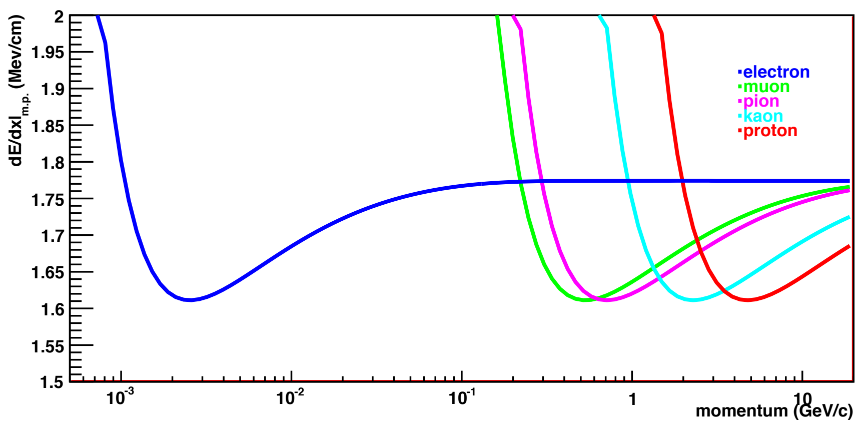

Figure 6.16: (Top) Background subtracted distribution of the hits at the start of the electron showers, with a fitted Gaussian-convolved Landau . (Bottom) Most probable value of ionization as a function of momentum for particles traversing liquid argon.

6.3 Detection of Electron Neutrinos

To verify that the sample of electron-candidate events are predominantly electron neutrino events, the kinematic behavior of the electron-candidate sample has been studied. Due to the small active volume of the ArgoNeuT detector, the electromagnetic showers are poorly contained and the reconstructed electron energy is not a measurable quantity. Instead, we measure the distribution of reconstructed *deposited* energy, compared to a simulation of electron neutrino events using the electron neutrino and anti-neutrino flux shown in Figure 2.7. This flux used to simulate the electron neutrino events is generated with a simulation of the NuMI beam with FLUKA [80]. The mean energy of the electron anti-neutrinos is 4.3 GeV, while the mean energy of electron neutrinos is 10.5 GeV. As seen, the beam is predominately electron anti-neutrinos.

Figure 6.17 shows the kinematic distribution of the electron events' deposited energy and angle θ. For both the deposited energy and the polar angle θ, the agreement between data and Monte Carlo is good. For the measurement of deposited energy, the Monte Carlo deposited energy is scaled by 24.5% to model the reconstruction inefficiencies as observed above.

In Figure 6.17, both the deposited energy and reconstructed angle are area normalized independently for both data and simulation. Due to the fact that the electron candidate events were selected manually from a sample of showering events, we are unable to accurately estimate the efficiency of electron neutrino selection. Therefore, an absolute comparison of data and Monte Carlo is not possible, and not presented here. For the same reason, the measurement of the electron neutrino scatter cross section is also not presented.

Regardless, this analysis is the first observation of low energy electron neutrinos in a liquid argon time projection chamber. This is an essential step towards the successful analyses of MicroBooNE, the SBN Program, and DUNE.

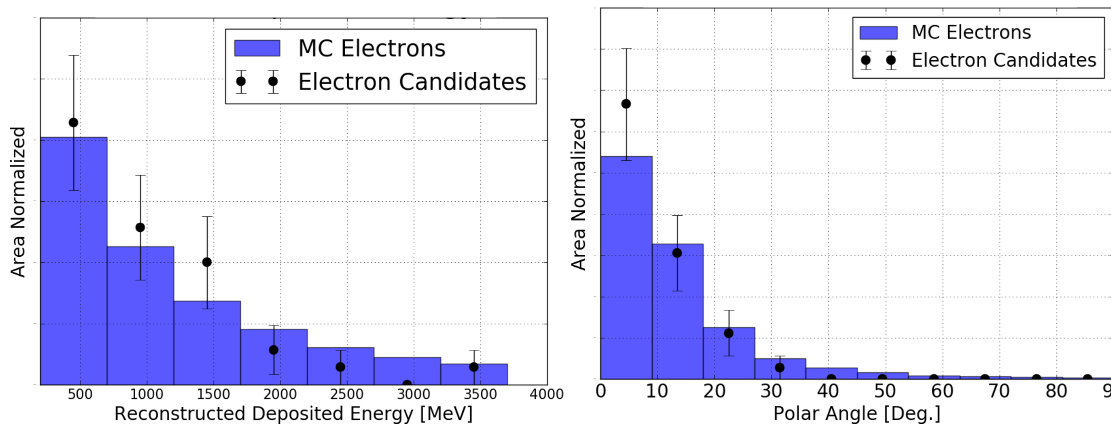

Figure 6.17: (Left) Electron deposited energy. (Right) Electron polar angle. In general, these kinematic variables agree with the simulation, despite low data statistics.msd2

6.4 dE/dx Separation

Once an electromagnetic shower has been identified and reconstructed, the information from the charge depositions at the start of the shower needs to be aggregated into a single dE/dx metric.

In the previous section, the conversion from dQ/dx (the measured charge per unit centimeter), to dE/dx (deposited energy per unit centimeter) is computed using a nonlinear model of the recombination of electrons and argon ions [94, 122]. In considering the ionization at the start of a gamma induced shower where an electron and positron pair are present, we assume the ionization clouds of the two particles are sufficiently separated such that a non linear model incorrectly inflates the dE/dx from a dQ/dx, for higher values of dQ/dx. Thus, the dE/dx separation is computed using a minimally ionizing particle scale recombination correction for all charge depositions at the beginning of the shower in the electron and gamma samples. While this is not applicable for highly ionizing fluctuations, it prevents an over estimation of the dE/dx of gammas which artificially inflates the calorimetric separation power.

For a given event there is not a statistically large sample of energy depositions to use for measuring a robust average dE/dx. Given the Landau nature of the energy deposition fluctuations away from the most probable value, it is not surprising that an aggregate metric will tend towards higher energy depositions per centimeter than the most probable value. For this analysis, when computing the dE/dx separation metric for a shower all of the hits within a rectangle of 4 cm along the direction of the shower and 1 cm perpendicular to the shower are collected, and the median is computed.

6.5 dE/dx Calculation Methods

While investigating the methods to convert a sample of hits (per shower) into a single variable, three promising dE/dx metrics were developed:

1. **Outlier Removed Mean**: For every hit considered for each shower (within a certain distance from the start), the mean dE/dx of the hits is calculated, as well as the RMS. The hits that are outside of the mean $\pm$ the RMS are then rejected, and the mean of the remaining hits is recomputed and used.

2. **Median**: The same initial set of hits as above is used. However instead of rejecting outliers a median is calculated. In particular, this method is robust against single high or low fluctuations.

3. **Lowest Moving Average**: For the same set of N initial hits, a moving 3 hit average is calculated. For example, for N hits, the average is calculated of the hits (1,2,3), then the hits (2,3,4), etc. until the hits (N-2, N-1, N). For all of these average values calculated, the lowest value is used as the dE/dx measure. This is designed to find regions where the start of the shower is behaving as a minimally ionizing particle for an extended period.

To determine which metric is the best for separating electrons from gammas, the truth level energy depositions from the Monte Carlo simulation are examined. For each event, the true energy depositions are binned into "hits" with a pitch that corresponds to the pitch of the simulated shower on the collection plane. Then, the three dE/dx metrics above are computed for the true hits, and this processes is repeated while varying the length of the shower used in the dE/dx calculation. The number of hits used in the calculation is a function of the distance along the shower, from the start and moving along the axis of the shower, from which the hits are collected. The distance used is varied from 2 cm up to 20 cm, with a width of 1 cm. It was found that a width of 1 cm was sufficient to collect the hits along the trunk of the shower. The results are provided in Figure 6.18, which show that the median metric is the most robust over a variety of distances used at the start of the shower. Give this result, the median is chosen as the optimal metric for this paper.

In addition, the length of the shower used in this analysis is fixed at 4cm. As shown in Figure 6.18, even the median metric begins to degrade at longer distances along the shower, though the degradation is much slower than with the other two methods. The exact distance used is not the most important parameter. Between 3 and 5 cm of distance along the shower, all distances yield equivalent separation power.

Lastly, to verify that the dE/dx calculation from the reconstruction accurately models the true dE/dx of the electromagnetic showers, Figure 6.19 shows the relationship between the true dE/dx and the reconstructed dE/dx. This demonstrates that the reconstructed dE/dx well reproduces the true dE/dx of each shower.

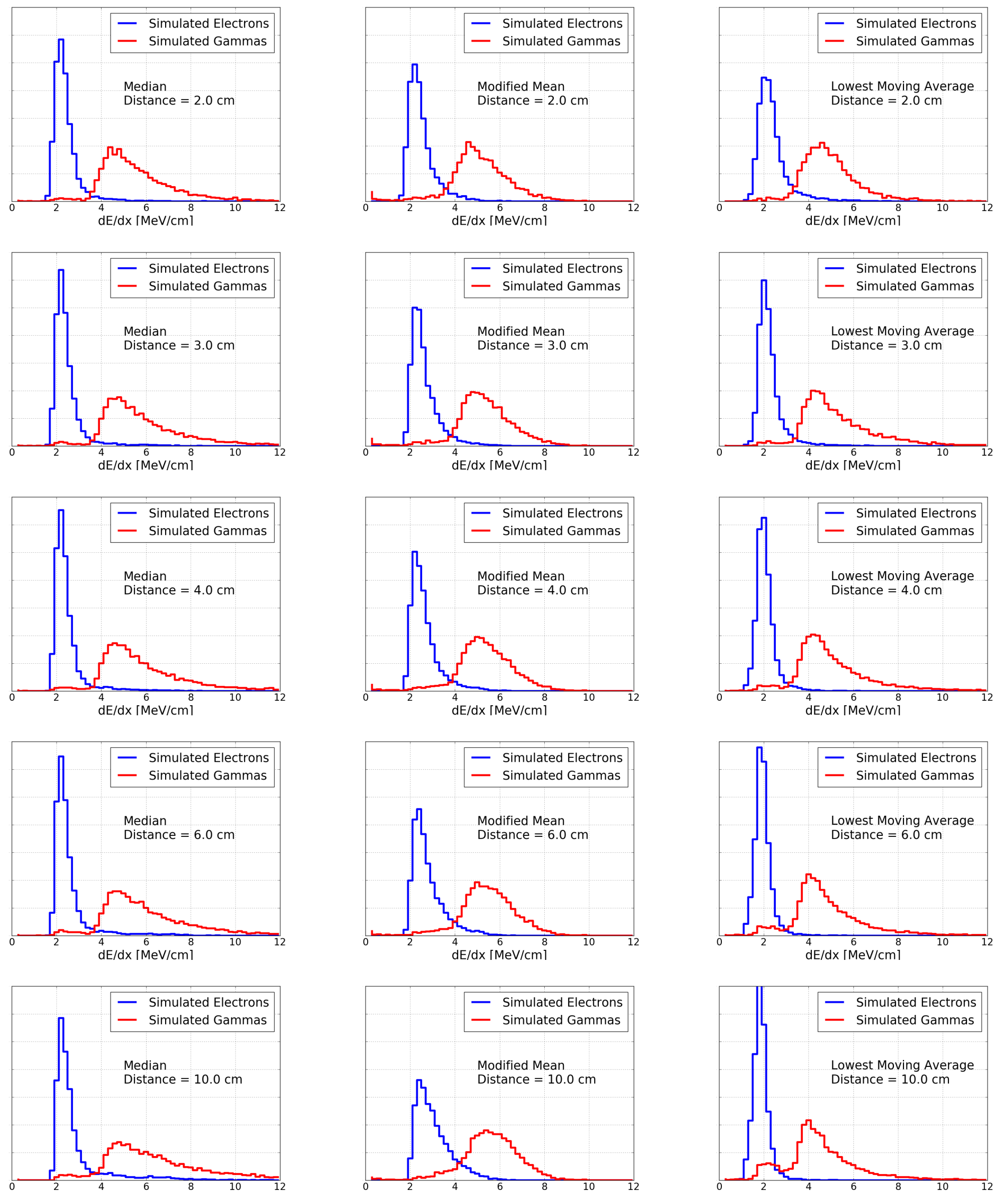

Figure 6.18: The separation power of the three dE/dx metrics, using a variable amount of the start of the shower in the calculation. As can be seen, all three metrics show promise at shortest distances. However, at long distances, the Modified Mean develops a large tail in the electron distribution, and the Lowest Moving Average shifts many gammas into the electron peak.

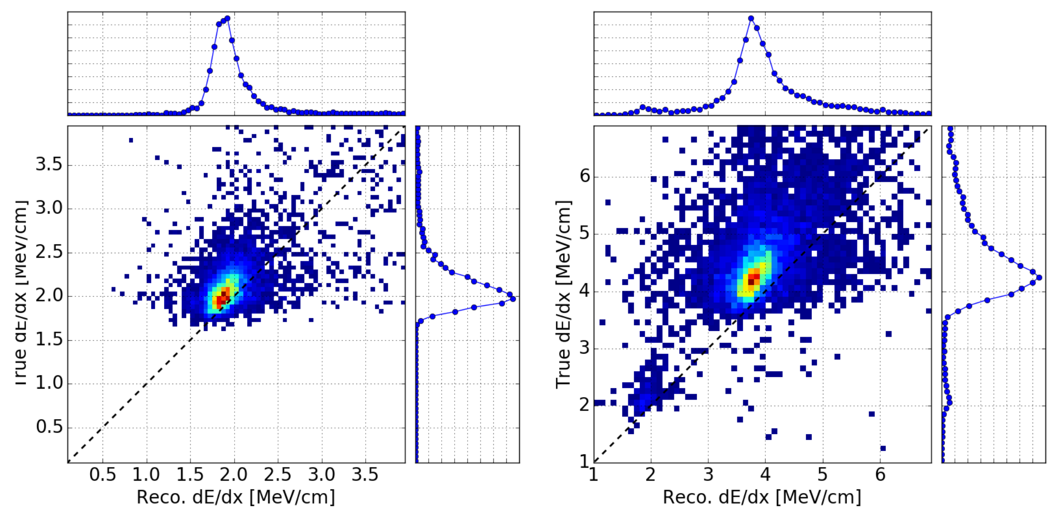

Figure 6.19: The true dE/dx of the beginning of simulated showers, calculated from simulated energy depositions in the TPC, vs the reconstructed dE/dx of the same showers. The electrons (left) and the gammas (right) both show a strong correlation between true and reconstructed dE/dx. There is a small offset arising from reconstruction inefficiencies, below the 10% level in both electrons and gammas.

6.6 Calorimetric Separation of Electromagnetic Showers

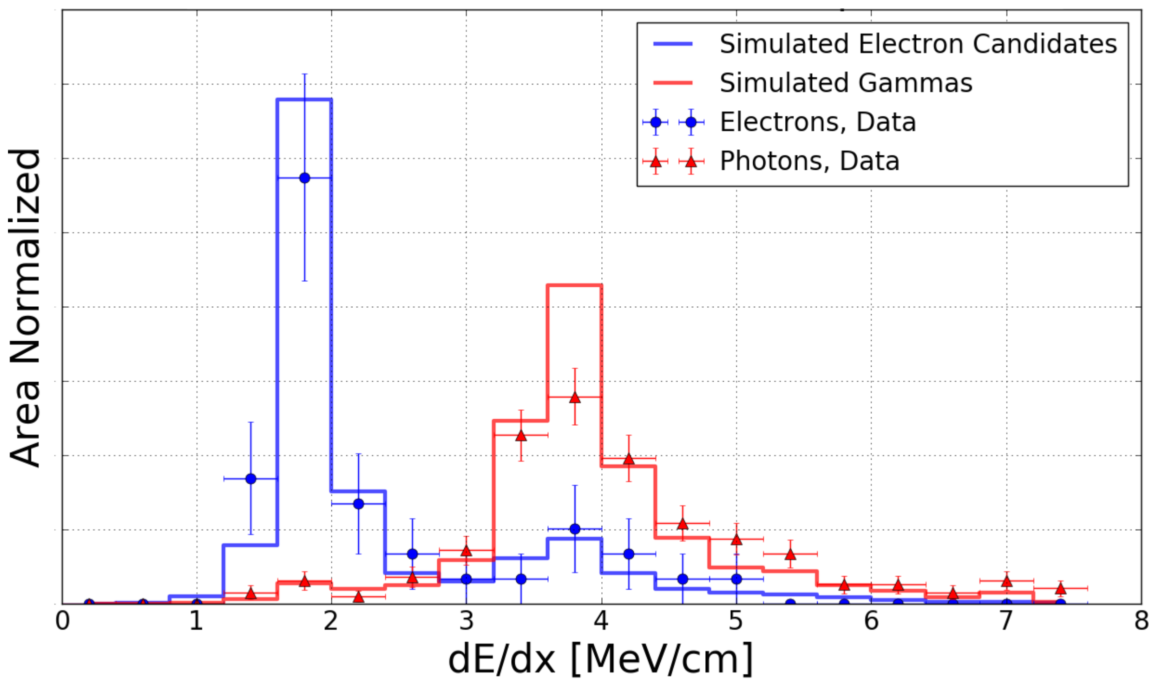

Figure 6.20: The dE/dx distribution for electrons (blue) and gammas (red). The solid blue curve, representing the simulation of electron dE/dx, includes a 20% containimation of gammas consistent with the results from Figure 6.15.

Figure 6.20 represents the first demonstration of calorimetric separation of electrons and gammas in a LArTPC using neutrino events. Despite the low statistics of the ArgoNeuT experiment, the electron and gamma separation using calorimetry is clearly validated. When a cut is made at 2.9 MeV/cm the efficiency of selecting electron candidate events in data is $76 \pm 7\%$ with a $7 \pm 2\%$ contamination from the gamma sample. Here, the uncertainties on the efficiency are estimated with the Feldman-Cousins method [123] and are statistical only. It must be noted, however, that the sample of electron candidates in this figure is not background subtracted. The efficiency to select electrons with the same cut at 2.9 MeV/cm, estimated with the Monte Carlo, is 91%. This is consistent with the above measurement that $20 \pm 15\%$ of the electron candidate sample, selected by topology only, is in fact gammas.

The value of the cut used above, 2.9 MeV/cm, is also somewhat arbitrary and must be determined uniquely for each analysis. In this case, it is selected as the mid point between the two peaks of the distribution. However, in an analysis targeting electron neutrinos the absolute normalization of the electron and gamma shower populations is crucial. The desired purity of electrons must be balanced with the need to keep sufficient electron statistics. An aggressive dE/dx cut, at 2.5 MeV/cm, effectively rejects gammas but also can remove a significant amount of electrons (removes 30% of electron candidate events in data, 13% of Monte Carlo electrons).

As seen in figure 6.6 and figure 6.5, the high granularity of a LArTPC allows precision topological discrimination of gammas and electrons. A purely topological cut produced a sample of electron events with an estimated $80 \pm 15\%$ purity. Further, full reconstruction of an event can improve gamma rejection. For example, identification of two electromagnetic showers that reconstruct with an invariant mass consistent with the π^0 mass can remove both showers as electron candidates, even if there is not a gap present for one shower and the dE/dx cut fails.

The analysis in this chapter has shown, using data, that a metric based on the dE/dx deposition in the beginning part of the shower is a valid method of separating electron-neutrino charged current events from gamma backgrounds. The full gamma background rejection capability of liquid argon detectors will be enhanced by adding to this a topological cut. This represents the first experimental proof of applying the calorimetric cut to separate electrons from gammas in a liquid argon detector using neutrino events.

One should note that the efficiency and misidentification rates presented here do not represent the full capability of liquid argon TPCs to discriminate gamma backgrounds from electron signals. The final separation power of LArTPCs leverages multiple identification techniques, of which calorimetry is just one. Further, the exact efficiencies and misidentification rates depend heavily on the energy spectrum of the electromagnetic showers: the Compton scattering gammas, a major source of impurity, appear predominately at energies below 200 MeV.

Chapter 7

Conclusions

Neutrino physics has grown substantially since the initial discovery of the neutrino, especially with the conclusive evidence of neutrino oscillations and neutrino mass, for which the Nobel prize was awarded in 2015. It is entering an era where deviations of even a few percent from the expected model of neutrino oscillations and interactions are detectable. The next generation of neutrino detector technology is already running: fine granularity tracking detectors such as liquid argon time projection chambers are the preferred choice of neutrino experiments in the 1 GeV range.

In this thesis, a study of the expected backgrounds to the SBN Program were presented, and an expectation of the expected event rates including an estimate of the signal from a 3+1 sterile neutrino oscillation was shown. The SBN Program, however, will require a measurement of electron neutrinos to extraordinary precision, and so a detailed understanding of the systematic uncertainties of its measurements are necessary. In Chapter 5, it was shown that the uncertainties from the neutrino flux and cross sections can be constrained to several percent uncertainty by exploiting a multi-detector analysis.

The estimate of systematic uncertainties for the SBN Program did not include the uncertainties from sources such as detector effects or reconstruction efficiencies. However, the strength of the SBN Program lies in the fact that its three detectors are the same technology along the same neutrino beam, and the systematic uncertainties largely cancel. The uncertainties associated with detector effects and event reconstruction will need to be studied before the final analysis of the SBN program. However, if history is our guide, like other multi-detector experiments with precision detectors, the SBN Program will make a substantial impact on neutrino physics.

The first step toward the physics goals of the SBN Program, as well as DUNE and MicroBooNE, is the observation and characterization of its signature oscillation channel. In Chapter 6 the first observation of low energy electron neutrinos in a liquid argon time projection chamber was presented. This measurement will be extended in the future to an electron neutrino cross section on argon, after the development of automated event selection for electromagnetic showers. The critical next step is the development of an automated event selection for electron neutrinos in liquid argon.

The measurements of oscillations and electron neutrino appearance in many experiments will be constrained by its level of background rejection from high energy photons in the energy range of hundreds of MeV. Though liquid argon time projection chambers have long promised exquisite rejection of high energy gammas, this work is the first demonstration of those abilities with data. It was found that a purely topological selection of electron neutrinos could produce a sample that was 80 ± 15 % pure, and a calorimetric cut can be very efficiently applied to an electron neutrino sample to further reduce backgrounds from high energy photons. Future analyses can apply both of these results to measure electron neutrinos in the 1 GeV range with excellent purity.

Bibliography

[1] Enrico Fermi. Versuch einer theorie der β-strahlen.i / towards the theory of β-rays. *Z. Phys. 88 161*, 1934.

[2] C. L. Cowan, F. Reines, F. B. Harrison, H. W. Kruse, and A. D. McGuire. Detection of the free neutrino: A Confirmation. *Science*, 124:103–104, 1956.

[3] G. Danby, J-M. Gaillard, K. Goulianos, L. M. Lederman, N. Mistry, M. Schwartz, and J. Steinberger. Observation of high-energy neutrino reactions and the existence of two kinds of neutrinos. *Phys. Rev. Lett.*, 9:36–44, Jul 1962.

[4] K. Kodama et al. Observation of tau neutrino interactions. *Phys. Lett.*, B504:218–224, 2001.

[5] F. J. Hasert et al. Observation of Neutrino Like Interactions Without Muon Or Electron in the Gargamelle Neutrino Experiment. *Phys. Lett.*, B46:138–140, 1973.

[6] John N. Bahcall, Aldo M. Serenelli, and Sarbani Basu. New solar opacities, abundances, helioseismology, and neutrino fluxes. *Astrophys. J.*, 621:L85–L88, 2005.

[7] Raymond Davis, Jr., Don S. Harmer, and Kenneth C. Hoffman. Search for neutrinos from the sun. *Phys. Rev. Lett.*, 20:1205–1209, 1968.

[8] Y. Fukuda et al. Evidence for oscillation of atmospheric neutrinos. *Phys. Rev. Lett.*, 81:1562–1567, Aug 1998.

[9] Q. R. Ahmad et al. Direct evidence for neutrino flavor transformation from neutral current interactions in the Sudbury Neutrino Observatory. *Phys. Rev. Lett.*, 89:011301, 2002.

[10] W. Hampel et al. Final results of the Cr-51 neutrino source experiments in GALLEX. *Phys. Lett.*, B420:114–126, 1998.

[11] J. N. Abdurashitov et al. Measurement of the response of the Russian-American gallium experiment to neutrinos from a Cr-51 source. *Phys. Rev.*, C59:2246–2263, 1999.

[12] K. N. Abazajian et al. Cosmological and Astrophysical Neutrino Mass Measurements. *Astropart. Phys.*, 35:177–184, 2011.

[13] P. A. R. Ade et al. Planck 2013 results. XVI. Cosmological parameters. *Astron. Astrophys.*, 571:A16, 2014.

[14] L. Bornschein. Proceedings of the 22nd international nuclear physics conference (part 2) the katrin experiment - a direct measurement of the electron antineutrino mass in the sub-ev region. *Nuclear Physics A*, 752:14 – 23, 2005.

[15] S. Mertens, T. Lasserre, S. Groh, G. Drexlin, F. Glueck, A. Huber, A. W. P. Poon, M. Steidl, N. Steinbrink, and C. Weinheimer. Sensitivity of Next-Generation Tritium Beta-Decay Experiments for keV-Scale Sterile Neutrinos. *JCAP*, 1502(02):020, 2015.

[16] Hiroshi Nunokawa, Stephen J. Parke, and Jose W. F. Valle. CP Violation and Neutrino Oscillations. *Prog. Part. Nucl. Phys.*, 60:338–402, 2008.

[17] L. Wolfenstein. Neutrino Oscillations in Matter. *Phys. Rev.*, D17:2369–2374, 1978.

[18] S. P. Mikheev and A. Yu. Smirnov. Resonance Amplification of Oscillations in Matter and Spectroscopy of Solar Neutrinos. *Sov. J. Nucl. Phys.*, 42:913–917, 1985. [Yad. Fiz.42,1441(1985)].

[19] M. Antonello et al. A Proposal for a Three Detector Short-Baseline Neutrino Oscillation Program in the Fermilab Booster Neutrino Beam. 2015.

[20] J. Ashenfelter et al. The PROSPECT Physics Program. 2015.

[21] M. G. Aartsen et al. Searches for Sterile Neutrinos with the IceCube Detector. 2016.

[22] P. Adamson et al. Search for sterile neutrino mixing in the MINOS long baseline experiment. *Phys. Rev.*, D81:052004, 2010.

[23] P. Adamson et al. A search for sterile neutrinos mixing with muon neutrinos in MINOS. *Submitted to: Phys. Rev. Lett.*, 2016.

[24] F. P. An et al. Search for a Light Sterile Neutrino at Daya Bay. *Phys. Rev. Lett.*, 113:141802, 2014.

[25] R. Acciarri et al. Long-Baseline Neutrino Facility (LBNF) and Deep Underground Neutrino Experiment (DUNE). 2016.

[26] M. Antonello et al. Search for anomalies in the ν_e appearance from a ν_μ beam. *Eur. Phys. J.*, C73:2599, 2013.

[27] V. L. Dadykin et al. Detection of a Rare Event on 23 February 1987 by the Neutrino Radiation Detector Under Mont Blanc. *JETP Lett.*, 45:593–595, 1987. [Pisma Zh. Eksp. Teor. Fiz.45,464(1987)].

[28] K. S. Hirata et al. Observation in the Kamiokande-II Detector of the Neutrino Burst from Supernova SN 1987a. *Phys. Rev.*, D38:448–458, 1988.

[29] Samoil M. Bilenky and B. Pontecorvo. Lepton Mixing and Neutrino Oscillations. *Phys. Rept.*, 41:225–261, 1978.

[30] Ziro Maki, Masami Nakagawa, and Shoichi Sakata. Remarks on the unified model of elementary particles. *Prog. Theor. Phys.*, 28:870–880, 1962.

[31] Paul Langacker and David London. Lepton Number Violation and Massless Nonorthogonal Neutrinos. *Phys. Rev.*, D38:907, 1988.

[32] L. Bartoszek et al. Mu2e Technical Design Report. 2014.

[33] K. A. Olive et al. Review of Particle Physics. *Chin. Phys.*, C38:090001, 2014.

[34] W. Hampel et al. GALLEX solar neutrino observations: Results for GALLEX IV. *Phys. Lett.*, B447:127–133, 1999.

[35] Y. Fukuda et al. Solar neutrino data covering solar cycle 22. *Phys. Rev. Lett.*, 77:1683–1686, 1996.

[36] V. N. Gavrin. Measurement of the solar neutrino capture rate in SAGE and the value of the pp-neutrino flux at the earth. *Nucl. Phys. Proc. Suppl.*, 138:87–90, 2005. [,87(2005)].

[37] P. Anselmann et al. Solar neutrinos observed by GALLEX at Gran Sasso. *Phys. Lett.*, B285:376–389, 1992.

[38] M. Altmann et al. Complete results for five years of GNO solar neutrino observations. *Phys. Lett.*, B616:174–190, 2005.

[39] S. Fukuda et al. Determination of solar neutrino oscillation parameters using 1496 days of Super-Kamiokande I data. *Phys. Lett.*, B539:179–187, 2002.

[40] Q. R. Ahmad et al. Measurement of the rate of $\nu_e + d \to p + p + e^-$ interactions produced by ^8B solar neutrinos at the Sudbury Neutrino Observatory. *Phys. Rev. Lett.*, 87:071301, 2001.

[41] John N. Bahcall, Frank Calaprice, Arthur B. McDonald, and Yoji Totsuka. Solar neutrino experiments: The next generation. *Physics Today*, 49(7):30–36, 1996.

[42] K. Eguchi et al. First results from KamLAND: Evidence for reactor anti-neutrino disappearance. *Phys. Rev. Lett.*, 90:021802, 2003.

[43] T. Araki et al. Measurement of neutrino oscillation with KamLAND: Evidence of spectral distortion. *Phys. Rev. Lett.*, 94:081801, 2005.

[44] S. Abe et al. Precision Measurement of Neutrino Oscillation Parameters with KamLAND. *Phys. Rev. Lett.*, 100:221803, 2008.

[45] A. Gando et al. Constraints on θ_{13} from A Three-Flavor Oscillation Analysis of Reactor Antineutrinos at KamLAND. *Phys. Rev.*, D83:052002, 2011.

[46] Morihiro Honda, T. Kajita, K. Kasahara, and S. Midorikawa. A New calculation of the atmospheric neutrino flux in a 3-dimensional scheme. *Phys. Rev.*, D70:043008, 2004.

[47] G. D. Barr, T. K. Gaisser, P. Lipari, S. Robbins, and T. Stanev. Three-dimensional calculation of atmospheric neutrinos. *Phys. Rev. D*, 70:023006, Jul 2004.

[48] Vassily Plyaskin. Calculation of atmospheric neutrino flux. *Phys. Lett.*, B516:213–235, 2001.

[49] K. Abe et al. Evidence for the appearance of atmospheric tau neutrinos in super-kamiokande. *Phys. Rev. Lett.*, 110:181802, May 2013.

[50] Y. Ashie et al. Evidence for an oscillatory signature in atmospheric neutrino oscillations. *Phys. Rev. Lett.*, 93:101801, Sep 2004.

[51] M. H. Ahn et al. Measurement of neutrino oscillation by the k2k experiment. *Phys. Rev. D*, 74:072003, Oct 2006.

[52] P. Adamson et al. Measurement of the neutrino mass splitting and flavor mixing by minos. *Phys. Rev. Lett.*, 106:181801, May 2011.

[53] P. Adamson et al. Measurements of atmospheric neutrinos and antineutrinos in the minos far detector. *Phys. Rev. D*, 86:052007, Sep 2012.

[54] K. Abe et al. Precise measurement of the neutrino mixing parameter θ_{23} from muon neutrino disappearance in an off-axis beam. *Phys. Rev. Lett.*, 112:181801, May 2014.

[55] P. Adamson et al. First measurement of muon-neutrino disappearance in nova. *Phys. Rev. D*, 93:051104, Mar 2016.

[56] P. Adamson et al. First measurement of electron neutrino appearance in NOvA. *Phys. Rev. Lett.*, 116(15):151806, 2016.

[57] P. Adamson et al. Improved search for muon-neutrino to electron-neutrino oscillations in minos. *Phys. Rev. Lett.*, 107:181802, Oct 2011.

[58] P. Adamson et al. First measurement of electron neutrino appearance in nova. *Phys. Rev. Lett.*, 116:151806, Apr 2016.

[59] K. Abe et al. Evidence of electron neutrino appearance in a muon neutrino beam. *Phys. Rev. D*, 88:032002, Aug 2013.

[60] F. Ardellier et al. Letter of intent for Double-CHOOZ: A Search for the mixing angle theta(13). 2004.

[61] Y. Abe et al. Indication of reactor $\overline{\nu}_e$ disappearance in the double chooz experiment. *Phys. Rev. Lett.*, 108:131801, Mar 2012.

[62] F. P. An et al. Observation of electron-antineutrino disappearance at daya bay. *Phys. Rev. Lett.*, 108:171803, Apr 2012.

[63] J. K. Ahn et al. Observation of reactor electron antineutrinos disappearance in the reno experiment. *Phys. Rev. Lett.*, 108:191802, May 2012.

[64] F. P. An et al. New Measurement of Antineutrino Oscillation with the Full Detector Configuration at Daya Bay. *Phys. Rev. Lett.*, 115(11):111802, 2015.

[65] M. Sisti et al. Status of the CUORE and results from the CUORE-0 neutrinoless double beta decay experiments. *Nucl. Part. Phys. Proc.*, 273-275:1719–1725, 2016.

[66] M. Auger et al. Search for Neutrinoless Double-Beta Decay in ^{136}Xe with EXO-200. *Phys. Rev. Lett.*, 109:032505, 2012.

[67] M Agostini et al. 2 decay of 76 ge into excited states with gerda phase i. *Journal of Physics G: Nuclear and Particle Physics*, 42(11):115201, 2015.

[68] K. Abe et al. Letter of Intent: The Hyper-Kamiokande Experiment — Detector Design and Physics Potential —. 2011.

[69] D. S. Ayres et al. NOvA: Proposal to build a 30 kiloton off-axis detector to study nu(mu) —¿ nu(e) oscillations in the NuMI beamline. 2004.

[70] P. Adamson et al. The NuMI Neutrino Beam. *Nucl. Instrum. Meth.*, A806:279–306, 2016.

[71] A. A. Aguilar-Arevalo et al. The Neutrino Flux prediction at MiniBooNE. *Phys. Rev.*, D79:072002, 2009.

[72] K. Abe et al. A Long Baseline Neutrino Oscillation Experiment Using J-PARC Neutrino Beam and Hyper-Kamiokande. 2014.

[73] J. Grange et al. Muon (g-2) Technical Design Report. 2015.

[74] R. Acciarri et al. Long-Baseline Neutrino Facility (LBNF) and Deep Underground Neutrino Experiment (DUNE). 2015.

[75] M. G. Catanesi et al. Measurement of the production cross-section of positive pions in the collision of 8.9-GeV/c protons on beryllium. *Eur. Phys. J.*, C52:29–53, 2007.

[76] I. Chemakin et al. Pion production by protons on a thin beryllium target at 6.4-Ge, 12.3-GeV/c, and 17.5-GeV/c incident proton momenta. *Phys. Rev.*, C77:015209, 2008. [Erratum: Phys. Rev.C77,049903(2008)].

[77] S. Agostinelli et al. GEANT4: A Simulation toolkit. *Nucl. Instrum. Meth.*, A506:250–303, 2003.

[78] T. S. Nigmanov et al. Electromagnetic and hadron calorimeters in the MIPP experiment. *Nucl. Instrum. Meth.*, A598:394–399, 2009.

[79] C. Alt et al. Inclusive production of charged pions in p+C collisions at 158-GeV/c beam momentum. *Eur. Phys. J.*, C49:897–917, 2007.

[80] L. Aliaga et al. Neutrino Flux Predictions for the NuMI Beam. *Submitted to: Phys. Rev. D*, 2016.

[81] Christian Lippmann. Performance of the ALICE Time Projection Chamber. *Phys. Procedia*, 37:434–441. 8 p, 2012.

[82] K. Aamodt et al. The ALICE experiment at the CERN LHC. *JINST*, 3:S08002, 2008.

[83] Xiao Luo. MuSun: muon capture on the deuteron. *EPJ Web Conf.*, 95:04037, 2015.

[84] D. S. Akerib et al. The Large Underground Xenon (LUX) Experiment. *Nucl. Instrum. Meth.*, A704:111–126, 2013.

[85] E. Aprile et al. The XENON100 Dark Matter Experiment. *Astropart. Phys.*, 35:573–590, 2012.

[86] W. J. Willis and V. Radeka. Liquid Argon Ionization Chambers as Total Absorption Detectors. *Nucl. Instrum. Meth.*, 120:221–236, 1974.

[87] C. Rubbia. The Liquid Argon Time Projection Chamber: A New Concept for Neutrino Detectors. 1977.

[88] P. Musset and J. P. Vialle. Neutrino Physics with GARGAMELLE. *Phys. Rept.*, 39:1–130, 1978.

[89] T. Heindl, T. Dandl, M. Hofmann, R. Krucken, L. Oberauer, W. Potzel, J. Wieser, and A. Ulrich. The scintillation of liquid argon. *Europhys. Lett.*, 91:62002, 2010.

[90] C. Anderson et al. The ArgoNeuT Detector in the NuMI Low-Energy beam line at Fermilab. *JINST*, 7:P10019, 2012.

[91] C. Anderson et al. First Measurements of Inclusive Muon Neutrino Charged Current Differential Cross Sections on Argon. *Phys. Rev. Lett.*, 108:161802, 2012.

[92] R. Acciarri et al. Measurements of Inclusive Muon Neutrino and Antineutrino Charged Current Differential Cross Sections on Argon in the NuMI Antineutrino Beam. *Phys. Rev.*, D89(11):112003, 2014.

[93] C. Anderson et al. Analysis of a Large Sample of Neutrino-Induced Muons with the ArgoNeuT Detector. *JINST*, 7:P10020, 2012.

[94] R. Acciarri et al. A study of electron recombination using highly ionizing particles in the ArgoNeuT Liquid Argon TPC. *JINST*, 8:P08005, 2013.

[95] R. Acciarri et al. Detection of back-to-back proton pairs in charged-current neutrino interactions with the ArgoNeuT detector in the NuMI low energy beam line. *Phys. Rev.*, D90(1):012008, 2014.

[96] R. Acciarri et al. First Measurement of Neutrino and Antineutrino Coherent Charged Pion Production on Argon. *Phys. Rev. Lett.*, 113(26):261801, 2014. [Corrigendum: Phys. Rev. Lett.114,no.3,039901(2015)].

[97] A. N. Kalinovsky, N. V. Mokhov, and Yu. P. Nikitin. *PASSAGE OF HIGH-ENERGY PARTICLES THROUGH MATTER*. 1989.

[98] Eric D. Church. LArSoft: A Software Package for Liquid Argon Time Projection Drift Chambers. 2013.

[99] M. Antonello et al. Precise 3D track reconstruction algorithm for the ICARUS T600 liquid argon time projection chamber detector. *Adv. High Energy Phys.*, 2013:260820, 2013.

[100] The MicroBooNE Collaboration. The pandora multi-algorithm approach to automated pattern recognition in lar tpc detectors, 2016.

[101] D. G. Michael et al. The Magnetized steel and scintillator calorimeters of the MINOS experiment. *Nucl. Instrum. Meth.*, A596:190–228, 2008.

[102] H. Chen et al. Proposal for a New Experiment Using the Booster and NuMI Neutrino Beamlines: MicroBooNE. 2007.

[103] A. A. Aguilar-Arevalo et al. The MiniBooNE Detector. *Nucl. Instrum. Meth.*, A599:28–46, 2009.

[104] The MicroBooNE Collaboration. Measurement of the electronegative contaminants and drift electron lifetime in the microboone experiment, 2016.

[105] D. Caratelli for the MicroBooNE Collaboration. Noise dependence on temperature and lar fill level in the microboone time projection chamber, 2015.

[106] The MicroBooNE Collaboration. Selection and kinematic properties of charged-current inclusive events in 5×10^{19} pot of microboone data, 2016.

[107] Joachim Kopp, Pedro A. N. Machado, Michele Maltoni, and Thomas Schwetz. Sterile Neutrino Oscillations: The Global Picture. *JHEP*, 05:050, 2013.

[108] C. Giunti, M. Laveder, Y. F. Li, and H. W. Long. Pragmatic View of Short-Baseline Neutrino Oscillations. *Phys. Rev.*, D88:073008, 2013.

[109] C. Athanassopoulos et al. Candidate events in a search for anti-muon-neutrino —¿ anti-electron-neutrino oscillations. *Phys. Rev. Lett.*, 75:2650–2653, 1995.

[110] Patrick Huber. On the determination of anti-neutrino spectra from nuclear reactors. *Phys. Rev.*, C84:024617, 2011. [Erratum: Phys. Rev.C85,029901(2012)].

[111] Th. A. Mueller et al. Improved Predictions of Reactor Antineutrino Spectra. *Phys. Rev.*, C83:054615, 2011.

[112] G. Mention, M. Fechner, Th. Lasserre, Th. A. Mueller, D. Lhuillier, M. Cribier, and A. Letourneau. The Reactor Antineutrino Anomaly. *Phys. Rev.*, D83:073006, 2011.

[113] Feng Peng An et al. Measurement of the Reactor Antineutrino Flux and Spectrum at Daya Bay. 2015.

[114] A. A. Aguilar-Arevalo et al. Improved Search for $\bar{\nu}_\mu \rightarrow \bar{\nu}_e$ Oscillations in the MiniBooNE Experiment. *Phys. Rev. Lett.*, 110:161801, 2013.

[115] K. B. M. Mahn et al. Dual baseline search for muon neutrino disappearance at $0.5\mathrm{eV}^2 < \Delta m^2 < 40\mathrm{eV}^2$. *Phys. Rev.*, D85:032007, 2012.

[116] Carlo Giunti and Marco Laveder. 3+1 and 3+2 Sterile Neutrino Fits. *Phys. Rev.*, D84:073008, 2011.

[117] C. Andreopoulos et al. The GENIE Neutrino Monte Carlo Generator. *Nucl. Instrum. Meth.*, A614:87–104, 2010.

[118] Costas Andreopoulos, Christopher Barry, Steve Dytman, Hugh Gallagher, Tomasz Golan, Robert Hatcher, Gabriel Perdue, and Julia Yarba. The GENIE Neutrino Monte Carlo Generator: Physics and User Manual. 2015.

[119] F. P. An et al. The Detector System of The Daya Bay Reactor Neutrino Experiment. *Nucl. Instrum. Meth.*, A811:133–161, 2016.

[120] M.J. Berger, J.H. Hubbell, S.M. Seltzer, J. Chang, J.S. Coursey, R. Sukumar, D.S. Zucker, and K. Olsen. XCOM: Photon Cross Section Database (version 1.5), 2010. [Online] Available: http://physics.nist.gov/xcom [Wednesday, 03-Aug-2016 16:57:01 EDT]. National Institute of Standards and Technology, Gaithersburg, MD.

[121] I. Jolliffe. Principal component analysis, 2014.

[122] J.B. Birks. The Theory and Practice of Scintillation Counting. *Proc. Phys. Soc.*, A64: 874, 1964.

[123] Gary J. Feldman and Robert D. Cousins. A Unified approach to the classical statistical analysis of small signals. *Phys. Rev.*, D57:3873–3889, 1998.